MODELLING OF BLOOD FLOW IN A TIME-VARYING SHAPE PASSAGE

BY

SHAIK ABDUL QAIYUM

A Thesis Presented to the
DEANSHIP OF GRADUATE STUDIES

KING FAHD UNIVERSITY OF PETROLEUM & MINERALS

DHAHRAN, SAUDI ARABIA

In Partial Fulfillment of the
Requirements for the Degree of

MASTER OF SCIENCE

In

MECHANICAL ENGINEERING

APRIL 2005

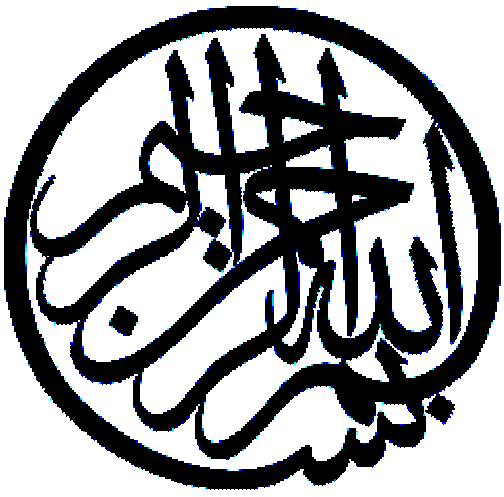

In the Name of Allah, Most Gracious, Most Merciful.

KING FAHD UNIVERSITY OF PETROLEUM & MINERALS
DHAHRAN 31261, SAUDI ARABIA

DEANSHIP OF GRADUATE STUDIES

This thesis, written by SHAIK ABDUL QAIYUM under the direction of his thesis advisor and approved by his thesis committee, has been presented to and accepted by Dean of Graduate Studies, in partial fulfillment of the requirements for the degree of

MASTER OF SCIENCE IN MECHANICAL ENGINEERING.

Thesis Committee

Dr. Rached Ben-Mansour(Advisor)

Dr. Badr, Hassan M (Member)

Dr. Nabil Maalej(Member)

Dr. Al-Sulaiman, Faleh A.
(Department Chairman)

Dr. Mohammad Al- Ohali
(Dean of Graduate Studies)

[Date] ١٨/٧/١٤٢٦هـ
24-7-2005

Dedicated to My Beloved Parents, Sister & Brother whose constant prayers, sacrifice and inspiration led to this wonderful accomplishment

ACKNOWLEDGMENT

All praise and thanks are due to Almighty **Allah,** *subhana-wa-taala,* the most Merciful; the most Benevolent, for bestowing me with the health, knowledge, opportunity, courage and patience to complete this work. Thereafter, acknowledgement is due to KFUPM for the support given to this research through its tremendous facilities and for granting me the opportunity to purse graduate studies with financial support.

I acknowledge, with deep gratitude and appreciation, the inspiration encouragement, valuable time and guidance given to me by my thesis Committee Chairman, Dr. Rached Ben-Mansour.

Thereafter, I am deeply indebted and grateful to Dr. Hassan M. Badr and Dr. Nabil Maalej, my committee members, for their extensive guidance, continuous support, and personal involvement in all phases of this research. Thanks are also to director of PC labs Dr. M. A. Antar and administrators Mr. Riyaz and Mr. Kamran for there help in providing me adequate computing facilities thorough out this work and the department secretaries, Mr. Lateef and Mr. Jameel for their help and assistance.

I am also thank full to department Chairman Dr. Faleh A. Al-Sulaiman for providing me favorable environment where I able to utilize my skills.

Special thanks are due to my senior colleagues at the University, Mujtaba Hussain, Arifussalam, Farrukh Sagir, Md.Iftekhar, Arshad, Bilal, Hassan, who were always there to help me in my work. I would also like to thank my friends Mazher, Baqtiyar, Yousuf, Siraj, Anees, Riyaz, Adil, Farooq, Kashif, Sarfraz, Yoga, Deepak, Soma, Hari, Sridhar, Samiuallah, Hafeez, Basha, Atif, Hameed, Khaja, Shafeeq, Shujath, Razwan, Faheem, Zahed, Omer, Jaffer, Khaliq, Obaid, Rizwan, Fasi, Mujahed, Abbas, and all others who provided wonderful company and good memories that will last a life time. Special thanks are due to Saad and Ayub Azher, who were always there to help me in my work and my sincere appreciation is due to all other North Compound friends who provided wonderful company and some memories that will last a lifetime.

Family support plays a vital role in the success of an individual. I am thankful to my entire family for its love, support and prayers throughout my life especially my dearest mother and father who devoted their lives in the endeavor of getting me a quality education, my dearest sister: Firdouse and my dearest brother: Abdul Wahab, my dearest uncle: Nanne Saheb and aunty: Haseena. Also I am grateful to all other relatives, for their emotional and moral support throughout my academic career and also for their love, patience, encouragement and prayers.

I would in the end must appreciate the efforts of my father and mother who supported me a lot during my education and without their help I could not achieve my goals.

TABLE OF CONTENTS

Page

CHAPTER 4

CHAPTER 5

List of Tables

TABLE Page

LIST OF FIGURES

Figure Page

THESIS ABSTRACT

Name: SHAIK ABDUL QAIYUM

Title: MODELLING OF BLOOD FLOW IN A TIME-VARYING SHAPE PASSAGE

Major Field: MECHANICAL ENGINEERING

Date of Degree: APRIL, 2005

In the present work, the time-dependent flow in an axisymmetric tube with a moving indentation was numerically simulated using the dynamic mesh model. The model was first validated for a two-dimensional channel with a moving indentation. The results showed very good agreement with the available experimental and numerical results. The model was then used to simulate the water and blood flow in an axisymmetric tube with an indentation moving at different frequencies. Water was simulated at two different indentation frequencies i.e. f_w=0.1Hz and f_w=1Hz. Blood was simulated considering the indentation frequency of f_w=1Hz, which is close to the heart beat frequency assuming blood as a Newtonian fluid with steady and pulsatile inlets. Later, the non-Newtonian properties of blood were considered. The non-Newtonian properties of blood were characterized using non-Newtonian power law, Carreau model and the Carreau-Yasuda model.

In the case of water flow, for wall frequency of 0.1 Hz a single eddy was observed, where as for a higher frequency of 1 Hz eddy doubling was observed with the reverse flow dominating the downstream of indentation. In the case of steady Newtonian blood flow no recirculation zone was observed upstream of the indentation while the recirculation zone was observed for the pulsatile blood flow case. In addition, eddy doubling was also observed in this case. For the non-Newtonian models, no recirculation zone was observed upstream of the indentation. The three non-Newtonian models exhibited the similar behavior. Higher wall shear stresses and pressure drops were obtained for the blood flow when compared with the water flow.

MASTER OF SCIENCE DEGREE

KING FAHD UNIVERSITY OF PETROLEUM AND MINERALS

Dhahran, Saudi Arabia

ملخص الرسالة

الاســـــــــم: شايك عبد القيوم

عنوان الرسالة: محاكاه لسريان الدم فى ممر مع وخود تغير زمنى

التخصـــــص: : الهندسه الميكانيكيه

تاريخ التخـرج: ابريل 2005 م

فى هذا البحث يتم دراسه سريان متغير مع الزمن داخل انبوب متماثل حول محوره حيث تم عمل محاكاه رقميه باستخدام نموذج تفاعلى (ديناميكى)
تم التأكد من صحه النموذج فى قناه ثنائيه الابعاد اولا وقد اعطت نتائج متوافقه لدرجه كبيره مع النتائج القياسيه والرقميه السابقه.
تم استخدام النموذج فى محاكاه سريان الماء والدم فى انبوب متماثل حول محوره عند ترددات مختلفه. تم محاكاه سريان الماءعند ترددين هما 0.1 هرتز و 1 هرتز.
تم محاكاه سريان الدم عند تردد 1 هرتز والذى يعتبر قريب من قيمه تردد نبضات القلب مع اعتبار الخواص النيوتونيه للدم وسريان مستقر عند مدخل الانبوب تاره ومتقطع تاره اخرى.
ثم بعد ذلك اخذ فى الاعتبار الخواص اللانيوتونيه للدم باستخدام قانون الاس اللانيوتونى (نموذج كاريو وكاريو-ياسودا).
فى حاله سريان الماء وعند تردد 0.1 هرتز لوحظ وجود دوامه احاديه بينما عند تردد 1 هرتز حدث دوامه ثنائيه مع انعكاس اتجاه السريان.
اما فى حاله سريان الدم المستقر ذو الخواص النيوتونيه لم تحدث منطقه دوران عند المدخل بينما حدث دوران فى حاله السؤيان المتقطع بالاضافه الى وجود دوامات ثنائيه.
فى حاله النموذج اللانيوتونى للدم لم تحدث اى منطقه دوران وذلك عند استخدام كل طرق محاكاه السائل اللانيوتونى الثلاثه حيث اعطوا جميعهم نفس السلوك.
واخيرا تم الحصول على قيم اعلى للاجهادات ونقص الضغط فى حاله سريان الدم بالمقارنه بمثيلتها فى حاله سريان الماء.

رساله ماجستير

جامعه الملك فهد للبترول والمعادن

الظهران – المملكه العربيه السعوديه

ابريل 2005

NOMENCLATURE

b	Depth of unindented channel
$h_{\max}$	Maximum blockage of the channel at $\tau = 0.5$
p	Dimensional pressure
P	Non-dimensional pressure
Q_0	Volume flow rate
r	Radius
r_0	Radius of unindented tube
R	Non-dimensional radius of the tube
t	Dimensional time
δt	Time Step
t_0	Indentation motion period
U_0	Average velocity at the inlet or characteristic velocity
U	Non-dimensional velocity component in x -direction
u	Dimensional velocity component in x-direction
v	Dimensional velocity component in y-direction
$v_{\max}$	Maximum velocity
V	Non-dimensional velocity component in y-direction
X	Non-dimensional x co-ordinate
Y	Non-dimensional y co-ordinate

Greek Symbols

τ	Non-dimensional time
τ_w	Wall Shear stress
α	Wormersley parameter
μ	Viscosity
υ	Kinematic viscosity
ρ	Density
ω	Radial frequency

Subscripts

i, j	spatial coordinate indices
i	inlet condition
P	nodal point
w	wall condition
o	outlet condition

CHAPTER 1

INTRODUCTION

In this chapter, background information relevant to hemodynamic modeling of flow in blood vessels is given. The chapter also includes the structure and function of heart, blood rheology, and pulsatile flows. The chapter finishes with the motivation behind this thesis and the structure of the thesis document.

1.1. Computational Hemodynamics

The circulatory system consists of a branching network of arteries, veins, capillaries and the heart. The circulatory system distributes metabolites and oxygen to all cells and collects carbon dioxide and other waste products for excretion. The heart is the driving force for this system. Under normal conditions, the arteries can adapt to local changes in blood flow to maintain the overall homeostasis of the circulatory system.

A detailed knowledge of blood flow and the response of blood vessels, and the heart to different fluid forces is required in order to understand the normal behavior of the human circulatory system. Analyzing blood flow in the body may help us to identify the

locations in the circulatory system which are prone to arterial diseases (such as atherosclerotic lesions, intimal thickening, etc.) due to altered flow conditions. Experimental investigations of blood flow in the circulatory system have made important contributions to the understanding of vascular diseases and long-term consequences of surgical repair. However, experimental studies have several limitations. Some of these limitations are:

- Extraction of quantitative flow data from *in vitro* models (used for experimental visualization) is a time consuming and expensive process.

- It is not easy to use fluids that have the same rheological properties as blood. Also the use of a model having the same mechanical properties as blood vessels is quite challenging.

- Extraction of complete flow field information (pressure, velocity, shear stress etc.) through the region of interest is impractical.

In recent years, *Computational Fluid Dynamics* (CFD) has been increasingly utilized by researchers to better understand the hemodynamics of the circulatory system. CFD is a powerful tool for analyzing flow characteristics in complex geometries and is able to give detailed results of velocity and pressure fields at various locations in a complex geometry. CFD is useful in extracting details about flow field variables, which can be expensive and sometime impossible to obtain by experimental means. Parametric studies can be performed inexpensively with CFD, for example by changing the geometry, in flow and/or outflow boundary conditions. With the increasing performance

of computer hardware in terms of storage and speed, CFD has become a powerful tool in cardiovascular investigations.

Research in blood flow has a direct impact in improving our understanding and management of human health. Blood flow is a related measure of oxygen and nutrient concentrations in blood. Such concentration measures are an indication of general cell health. We begin by outlining the physiology involved in blood flow. This includes a discussion of the cardiovascular system, and of the regulation of cardiac output, blood flow, and blood pressure.

1.2. Physiology

The first requirement to study the blood flow is to gain a general understanding of the physiology involved. A brief outline of the circulatory system and cardiac output is provided below for better understanding of how blood is circulated and regulated in the human body.

1.2.1. The Circulatory System

The circulatory system is divided into two main components: the cardiovascular system, and the lymphatic system. The focus here will be on the cardiovascular system, which consists of blood, blood vessels, and the heart. Blood acts as a transport medium to the cells for nutrients and wastes. Blood vessels provide a tubular network to channel the

blood to every region of the body, and the heart supplies the pressure required to push the blood through the vessels.

1.2.1.1. Blood

Blood is a heterogeneous suspension containing several different components. Blood consists of plasma with red blood cells (erythrocytes), white blood cells (leucocytes), and platelets (thrombocytes) in suspension. In the typical adult human, blood is composed of approximately forty-five percent of plasma, and the other fifty-five percent consists of a further heterogeneous mixture of cellular components. Plasma is composed of 93% water and 3% particles: electrolytes, proteins, gases, nutrients, hormones, and waste products. Erythrocytes, or red blood cells (RBCs), are flattened discs with a depressed center, about $2.5\mu m$ thick and $7\mu m$ wide [1]. The depressed center provides increased surface area for the diffusion of gases. RBCs contain no nuclei or mitochondria, but they do contain hemoglobin. It is the hemoglobin, which binds to oxygen and allows the RBCs to transport oxygen to cells. Leukocytes, or white blood cells (WBCs), are larger than RBCs. They have a nuclei and mitochondria which enable them to move around. WBCs are capable of squeezing through pores in capillary walls in order to reach sites of infection. This aids WBCs in their participation in the body's immune response. Platelets are the smallest formed element and are actually fragments of large bone marrow cells. They contain no nuclei but are still capable of movement and function in blood clotting. All formed elements of blood are produced in the myeloid tissue, or red bone marrow, in a process known as hemopoiesis. Further more, all these

cells are deformable, with the erythrocytes being the most deformable. Significant deformations occur when the cells are passing through the capillaries. However, the cell membranes do not rupture because each cell has a cytoskeleton that supports its shape.

Therefore, the mechanical properties of blood should be studied by analyzing a liquid containing a suspension of flexible particles. A liquid is said to be Newtonian if the coefficient of viscosity is constant at all the rates of shear. This condition exists in most homogeneous liquids, including blood plasma. But the mechanical behavior of a liquid containing a suspension of particles can vary such that the liquid becomes non-Newtonian. These deviations become particularly significant when the particle size becomes appreciably large in comparison to the dimension of the channel in which the fluid is flowing. The situation happens in the microcirculation (for the small arterioles and capillaries). If the suspended particles are spherical and non-settling, then for any motion the shear stress will be proportional to the rate of shear and the suspension will be proportional to the rate of shear and the suspension will behave as a Newtonian fluid. However, if the suspended particles are not spherical or deformable in any way, then the shear stress is not proportional to the shear rate. The cells suspended in blood are not rigid spheres; therefore the behavior of the blood is non-Newtonian. But it has shown that the human blood is Newtonian at all rates of shear for hematocrits (proportion, by volume, of the blood that consists of red blood cells) up to about 12%. In general blood has a higher viscosity than plasma, and as the hematocrit rises, the viscosity of the suspension increases and non-Newtonian behavior is observed, being detectable first at very low rates

of shear. Studies with human blood show that viscosity is independent of shear rate when the shear rate is high.

In large vessel it is reasonable to assume blood has a constant viscosity because the vessel diameters are large compared with the individual cell diameters and because shear rates are high enough for viscosity to be independent of them. For very small vessels, it is not easy to reach conclusions as to the Newtonian nature of blood because some effects tend to decrease the viscosity and others to increase it.

1.2.1.2. Blood Vessels

The network of blood vessels allows the transport of blood to all living cells in the body. Their structure enables the exchange of blood plasma and dissolved molecules between the blood and surrounding tissues. Blood travels away from the heart passing through a series of vessels progressively smaller in diameter: arteries to arterioles to capillaries. Blood returns to the heart through a series of vessels progressively larger in diameter: capillaries to venules to veins. The walls of arteries and veins consist of three layers. The outermost layer is the tunica externa; it is composed of loose connective tissue. The middle layer is the tunica media; it is composed of smooth muscle. The innermost layer is the tunica intima; it is composed of the endothelium and connective tissue. The endothelium lines all inner walls of vessels, and capillaries consist only of the endothelium. Arteries contain more muscle than comparably sized veins. Large arteries stretch when the pressure of the blood rises during systole and recoil during diastole. The elastic recoil of the walls helps to produce a smoother flow of blood in the smaller arteries

and arterioles. However, the result is a cardiac cycle-dependent artery diameter. Smaller arteries and arterioles are less elastic than larger arteries, and contain a proportionally thicker layer of smooth muscle. Thus they maintain a relatively constant diameter.

Capillaries are the simplest structured vessel. They are composed of a single cell layer of endothelium and are about 8 mm in length. They permeate the entire body in a fine mesh to provide the surface area for blood and interstitial fluid transfer. Capillaries only contain about 250 ml of blood at any given time [1]. The amount of blood in a capillary bed is regulated by the precapillary sphincter muscles and the resistance to blood flow is provided by the small arteries and arterioles. Blood is transported back to the heart by venules, which empty into progressively larger and larger veins. The pressure in the veins is around 2 mm Hg that is insufficient to return blood to the heart [1]. However, veins pass between skeletal muscles, which contract during motion and naturally provide a massaging action on the veins. The squeezing effect increases venous pressure and helps to push the blood back up to the heart. One directional flow is maintained by venous valves, which close in response to increased pressure.

1.2.1.3. The Structure and Function of the Heart

The heart acts as a double pump to keep blood circulating through blood vessels. The heart consists of upper right and left atria and lower right and left ventricles (Figure 1.1). It is surrounded by the pericardium whose inner lining produces fluid to lubricate the hearts motion. The heart is composed of three layers: the epicardium forms an outer protective sheath; the myocardium forms the thick middle layer composed mainly of

cardiac muscle tissue; and the endocardium forms the inner layer which is continuous with the endothelium of the blood vessels. Blood enters the heart via the right atrium. The right atrium fills the right ventricle which pumps blood to the lungs and back to the left atrium. Blood is then passed to the left ventricle which pumps to the aorta and systemic arteries. Atrioventricular and semilunar valves open based on pressure gradients and allow the heart to pump blood in a unidirectional flow.

The cardiac cycle refers to the pattern of systole and diastole, and is produced by a wave of depolarization through the nodal tissues of the heart. The sinoatrial (SA) node initiates the cardiac cycle by depolarizing from about -60 mV to -40 mV [1].

The heart is a two step pump-first the atria, then the ventricles contract. During diastole, while the ventricles are relaxed, they are filled with blood by the atria. The ventricles are about 80% full before the atria actually contracts. The amount of blood ejected by the ventricles is about two-thirds that of the volume prior to contraction, and is referred to as the stroke volume [1].

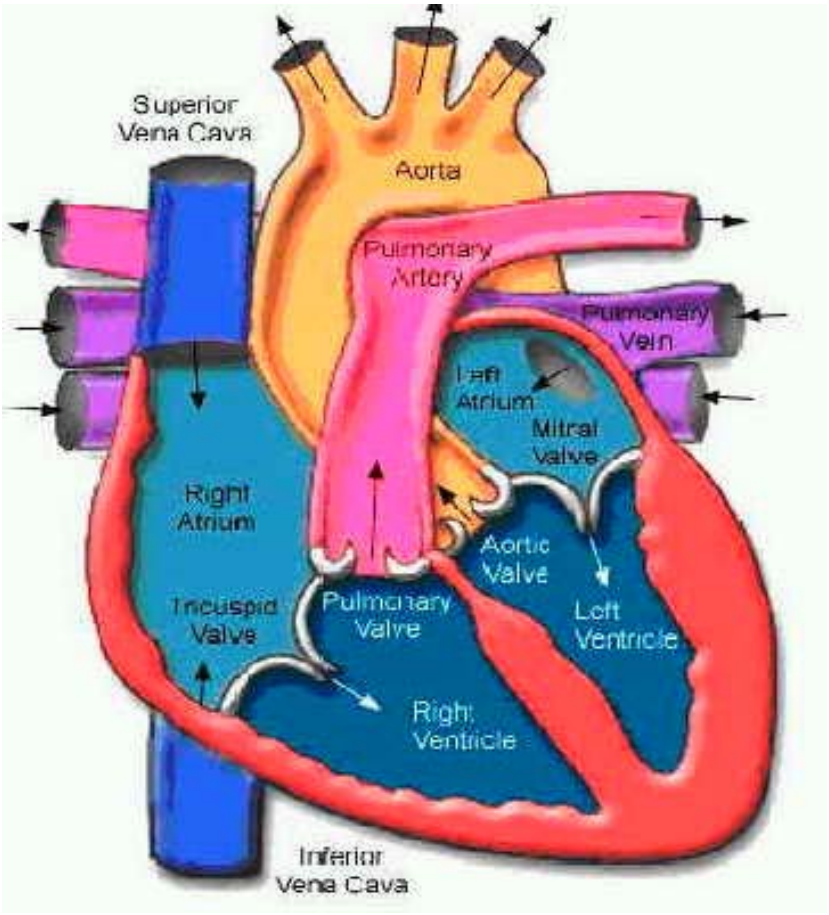

Figure 1.1 Schematic of the human heart.

1.2.2. Cardiac Output and Cardiac Rate

The amount of blood ejected from the ventricles, or cardiac output, is a measure of the pumping ability of the heart. The cardiac rate and stroke volume determines it.

$$\underset{(ml/\min)}{Cardiac\ output} = \underset{(beats/\min)}{Cardiac\ rate} \times \underset{(ml/beat)}{Stroke\ Volume\ per\ beat}$$

Cardiac output is related to total blood volume. An increase in cardiac output requires an increase in the rate blood flows through the vessels. This increased flow is caused by the regulation of cardiac rate and stroke volume. Cardiac rate is based on the natural rhythm of the SA node. Sympathetic and parasympathetic stimulation continuously modify the cardiac rate by increasing or decreasing the rate of depolarization. This autonomic activity is coordinated by the cardiac control centers of the medulla oblongata. Other effects of this autonomic nerve activity include changes in the AV node conduction rate, and changes in the strength of contraction for both the arterial and ventricular muscles.

1.2.2.1. Regulation of Stroke Volume

Recall that stroke volume is the amount of blood pumped per beat by each ventricle. It is regulated by three parameters:

- End-diastolic volume (EDV),

- Contractility, and
- Total peripheral resistance.

Stroke volume is directly proportional to EDV since an increase in the volume of blood in the ventricles prior to contraction, results in an increase in the ejection volume. Contractility is also directly proportional to stroke volume: a more forceful ejection results in a more complete emptying of the ventricles.

Total peripheral resistance, however, is inversely proportional to stroke volume. A higher resistance, or increase in arterial pressure, results in less blood entering the aorta. This is due to the fact that blood is only ejected from the ventricles while a pressure gradient exists. Higher arterial pressure means that the time it takes for the pressures to equalize is shorter, and thus less blood will transfer from ventricle to aorta.

1.2.2.2. Regulation of Blood Flow

Blood flow to an organ is controlled by the constriction and dilation of vessel walls. The changes in vessel diameter are regulated by sympathetic interaction and by local conditions within the blood vessel and organ. Sympathetic nerve stimulation causes vasoconstriction in the viscera and skin, and vasodilation in the skeletal muscles.

Myogenic regulation, in the cerebral arteries, causes the dilation of vessels in response to a decrease in blood pressure, and vice versa. Metabolic regulation, in the skeletal and cardiac muscle vessels, promotes vasodilation based on local conditions such as oxygen concentrations, carbon dioxide concentrations, tissue pH, and the release of

adenosine. The increase in blood flow in skeletal muscles and the heart as a result of increased metabolism is called active hyperemia.

1.2.2.3. Regulation of Blood Pressure

Blood pressure is regulated by changes in the cardiac rate, blood volume, and total peripheral resistance - all of which are controlled by the sympathoadrenal system. An increase in any of these parameters results in an increase in blood pressure. This effect, however, can be offset by a decrease in the other parameters.

Baroreceptors in the aortic arch and carotid sinuses detect an increase in pressure when the arterial walls of these regions are stretched. The sensory nerve activity of the baroreceptors is a negative feedback control for the medulla oblongata. Vasomotor control centers regulate the vasoconstriction, vasodilation, and total peripheral resistance in the vessels. Cardiac control centers regulate the cardiac rate.

1.3. Motivation And Importance Of Present Work

Flows in domains with moving boundaries are encountered in many practical situations. Applications, in which considerable research interest has been shown in recent years, are flow in blood vessels, in-cylinder flows in internal combustion engines, free surface flows, etc. The main feature of these flows is their unsteadiness, both with respect to flow patterns and to the shape of the boundaries. Flow inside moving-wall channels results in transient and complex flow phenomena. The complexity of these flows is

mainly due to the moving boundaries of the domain and the interaction between the moving wall and the flowing fluid. Occurrence of the flow detachment from the wall may result in oscillatory flow motion downstream of the moving wall.

Flow through severely atherosclerotic vessels is of great interest. These vessels pose grave health risks and are a major cause of mortality and morbidity in the industrialized world. Narrowing of a blood vessel, or stenosis, can result from substantial plaque deposit, and may cause a severe reduction of blood flow. The plaque may also break off into particles, or emboli, which may lodge in a vessel downstream. In the carotid artery bifurcation, which is particularly prone to plaque deposition, the danger of embolism is that the ruptured particles may be carried into the brain, provoking neurological symptoms or a stroke [1]. Ischemic coronary and cerebrovascular events often occur because of a sudden and dramatic change in a plaque that had narrowed an artery to a sub critical degree. This kind of sudden event is much more difficult to predict or diagnose than a gradual occlusion. Numerical simulation provides details of the entire flow field and is becoming more important in homodynamic analysis as computer technology and computations fluid dynamics (CFD) software continue to develop [3].

The flow, shear and pressure patterns across a narrowing mimics the clinical situation of arterial narrowing due to atherosclerotic plaque. Haemodynamic variables are known to have significant clinical applications. For instance, clot formation in narrowed arteries has been observed to occur in both areas of high shear and area of flow stagnation [9]. Qualifying and quantifying these haemodynamic variables and correlating them with

clinical observations may prove to be very valuable for clinical diognosis and prevention of thrombosis.

1.3.1. Motivation for Numerical Modeling

Reasons for numerically modeling of blood flow in an axisymmetric tube with moving indentation are:

- Once a proper model has been set up and validated, carrying out simulations can be both cheaper and less time consuming than conducting the corresponding experiments.
- Numerical modeling can be very helpful for understanding the physical phenomena that occur in flow in arteries and veins because it can estimate parameters that might be very difficult to measure during experiments.

This thesis analyzes the rheological and pulsatile effects of blood flow field in a two dimensional axisymmetric tube with moving indentation. Some background information about the physiology of the blood is given here to understand the work.

1.4. Thesis Structure

The thesis is organize into 7 chapters:

- Chapter 2 gives a brief view of the research carried out related to the present work and the objectives of the present work.

- In Chapter 3, different aspects like blood rheology, problem statement, boundary conditions and the governing equations have been discussed.

- In Chapter 4, the descritized version of the Navier-Stokes equations using Finite Volume method is discussed.

- In Chapter 5, the flow in a 2D planar channel with a moving indentation is numerically simulated using the dynamic mesh model and the results are validated against the published results. The above model is extended to simulate the water flow in a 2D axisymmetric tube with an indentation moving at different frequencies. Then the model was used to simulate the blood flow with steady and pulsatile inlets assuming the blood to be Newtonian.

- In Chapter 6, the above model was used to simulate the blood flow considering the non-Newtonian properties of the blood. The non-Newtonian properties of blood are characterized using the non-Newtonian power law, Carreau Model and Carreau-Yasuda model.

- In Chapter 7, conclusions are given, and recommendations for future research directions are proposed.

CHAPTER 2

LITERATURE REVIEW

2.1. Experimental Investigations

2.1.1. Flow In A Rigid Wall Channels

Pulsation of blood flow is an important factor dominating the unsteady flow phenomena in a cardiovascular system, because it complicates the vortical flow under time-varying inflow and pressure conditions. Pulsatile blood flow may show very different features between normal physiological and pathological situations, among different parts of arterial system or even at different instants, e.g., still or exercise under normal physiological conditions [4].

David *et al*. [5] studied the pulsatile flow in an in vitro model of the human carotid bifurcation by flow visualization using hydrogen bubble techniques. They constructed a glass model after determining an average geometry from 57 biplanar angiograms of 22

subjects ranging from 34 to 77 years of age. Visualization by hydrogen bubbles demonstrated significant deviations from steady flow behavior. Steady flow at the branch showed a fixed separation region, no evidence of turbulence, a well-defined unchanging secondary flow structure, and wall shear stress vectors, which do not change in time. In contrast, pulsatile flow created a continuously changing region of separation; possible turbulent disturbances at the end of systole; vortices which dramatically vary in size and energy level; wall shear stress vectors which change in both magnitude and direction, especially at the end of the outer wall divergence, and the frequency dependent phenomena of an increased residence time of the bubbles in the sinus, the extent of separation region, and the size of the secondary vortices.

David *et al*. [6]measured the fluid velocities by laser Doppler Velocimetry under conditions of pulsatile flow in a scale model of the human carotid bifurcation. They compared the flow velocity and wall shear stress at five axial and four circumferential positions with intimal plaque thickness at corresponding locations in carotid bifurcations obtained from cadavers. Comparison of detailed pulsatile hemodynamic measurements with quantitative morphologic studies revealed that low mean shear stress and marked oscillations in the direction of wall shear stress might be critical factors in the development and localization of atherosclerotic plaques. They suggested that the turbulence is not a prominent feature at sites of early plaque formation.

Moore & Ku [7] examined the hemodynamics of the abdominal aorta during physiological changes in flow rates and pulse rate that occur under exercise and postprandial conditions. They performed the hemodynamic measurements using an in

vitro model, which took into account seven major branches, the curvature and the pulsatile nature of blood flow of the abdominal aorta. They measured the pulsatile axial velocity profiles for the entire cross section at three axial locations using Magnetic resonance imaging velocimetry. They found that, under simulated exercise conditions, the forward velocities were approximately double those seen during rest, and the flow reversal seen for resting conditions was greatly reduced. They concluded that the changes that occur in abdominal aorta hemodynamics under different physiologic conditions might affect the rate of progression of atherosclerosis at this site.

Pulsatile flow through a bifurcation with a cerebrovascular aneurysm was experimentally studied by Liou *et al* [8]. They made Laser-Doppler velocimetry (LDV) measurements and flow visualization in pulsatile and steady flow in a cerebrovascular aneurysm model with bifurcation angles of 60, 90, and 140 degrees, and volume-flow rate ratios between the branches of 1 to 1 and 3 to 1. For unevenly distributed branches flow they found that the flow activity inside the aneurysm and stresses acting on the aneurysmal wall increase with increasing bifurcation angle. Their LDV measurements and flow visualization suggests the presence of critical bifurcation angle below which the aneurysm is prone to thrombosis, where as above which the aneurysm is susceptible to progression or rupture. For evenly distributed branch flow, the intra-aneurysmal flow in sluggish and therefore prone to thrombosis for all studied bifurcation angles.

Maalej, N, *et al*. [9] investigated the in vivo effect of percent stenosis, trans-stenotic pressure, and shear stress on platelet accumulation in canine mechanically injured and stenosed carotid arteries. In 10 dogs intimal damage and controlled variations in stenosis

were produced on the carotid artery. Blood flow through the stenosis, trans-stenotic pressure, and stenosis geometry were measured. The shear stress was obtained from the finite difference solution of the Navier-Stokes equations. It was found that the platelet accumulation was maximum at the stenotic portion of the vessel where the shear stress was high. Severe stenoses produce critical levels of shear stress that potentiate thrombosis and lead to life-threatening arterial occlusion.

The flow field less than one diameter downstream of the end of a collapsible tube executing self excited oscillations was examined by Betram *et al*. [10] using two component fiber-optic laser-Doppler anemometer. Their measurements showed strongly phasic turbulence intensity, with the phase of high intensity coinciding with the time of maximal tube collapse. They found that reverse flow occurred during much of the cycle at places in the cross section that agree with their previous observations of laminar and turbulent steady flow through a rigid simulated collapsed tube.

Xue and Stanley [11] examined the effects that different flow ratios between the proximal outlet segment (POS) and the distal outlet segment (DOV) have on the flow patterns and the distributions of hemodynamic factors in the anastomosis by using a pulsatile flow in vitro model of the distal end to side anastomosis of an arterial by pass graft. They obtained the detailed hemodynamic factors such as wall shear stress (WSS), Spatial wall shear stress gradient (WSSG), and oscillatory index. Their results showed that changes in POS: DOS flow ratios had a great influence on the flow patterns in the anastomossis. They found that, with an increase in proximal outlet flow, the range of location of stagnation point along the artery floor is decreased, while the extent of flow

separation along the graft hood increased. They concluded that a combination of low mean WSS and high oscillatary shear index (OSI) might be most prone to the formation of intimal hyperplasia.

The effect of homodynamic pressure, flow and waveform perturbations on the deposition of protein-sized in porcine carotid arteries was studied by Chesler and Enyinna [12]. An ex vivo perfusion system was used to control the waveform, pressure and flow environment for live arterial tissue. Three waveforms (steady, pulsatile and oscillatory) and two mean pressure levels were tested for their effects on particle deposition in live porcine carotid arteries. It was found that 200nm particles were deposited intimally along vessels perfused under oscillatory waveform conditions than all others. Under all pressure, flow and waveform conditions, particles were excluded from the media and adventitia of the vessel wall.

2.1.2. Flow in Deforming Channels

Stephanoff et.al. [13] experimentally studied the incompressible fluid flow along a channel with an asymmetric oscillating constriction. They observed a train of waves and double row of eddies, which appear in the core flow at the downstream of the oscillating constriction. Flow along a channel with moving indentation in one wall was experimentally studied by Pedley and Stephanoff [14]. They considered a steady flow for upstream, and the indentation in channel moved in and out sinusoidally in time. They found a vortex wave for both viscous and in viscid flow, but there were significant differences between the two cases. A much more complex pattern was obtained in the

viscous case, including ‘eddy doubling’ in which an eddy which initially shows a high degree of longitudinal symmetry becomes markedly asymmetric and eventually splits into at least two separate co-rotating eddies.

2.2. Numerical Investigations

2.2.1. Flow In A Rigid Wall Channels

The velocity distribution resulting from oscillatory blood flow has been extensively studied. The classical works of Womersley, Uchida, Atabek and Chang gave the fundamentals of oscillatory flow field theory. Womersley [15] improved Hagen-Poiseuille model by including the unsteady nature of the pressure and flow waveforms. He obtained an analytical solution to the Navier-Stokes equation by neglecting the convective terms and the motion of the vessel wall. Ling and Atabek [16] extended the model of Womersley. They included the non-linear convective terms of the N-S equations and the motion of the artery walls. Chang and Tarbell [17] made further developments for the curved tubes. They used finite difference method to describe the fully developed, time-dependent flow of a Newtonian fluid in rigid curved tubes. These authors also applied their model to flows in the coronary circulation. Mirsa and Sing [18] investigated the pulsatile flow of blood through arteries by treating the blood vessel as a thin walled anisotropic, non linear viscoelastic, incompressible material and blood as an incompressible Newtonian fluid whose motion is non linear.

Later Cen, *et al*. [19] made developments for oscillatory flow. They have presented a new set of formulas for velocity and pressure distribution in developing flows using the imaginary argument of the Bessel function to solve the Navier-Stokes equations in circular pipes under oscillatory conditions. They showed that their formulas were consistent with both Atabek's computed results and the experimental measurements.

The numerical study of pulsatile non-Newtonian flow characteristics in a three-dimensional human carotid bifurcation model was carried by Perktold *et al*. [20]. They considered both Newtonian and Non-Newtonian behavior of the blood. They presented numerical results for the flow velocity field and the wall shear stress during the pulse cycle. The comparison of non-Newtonian results and of Newtonian results demonstrated that, under flow conditions, the Newtonian simplification yields no change in the essential flow characteristics, however a minor difference was seen in the secondary flow.

Xu *et al*. [21] predicted the three-dimensional flows through canine femoral bifurcation models by solving numerically the time-dependant three-dimensional Navier-strokes equation. They assumed two models for the blood (i) a Newtonian fluid (ii) Non-Newtonian fluid obeying the power law. They found that the non-Newtonian characteristics might not be an important factor in determining the general flow patterns for these bifurcations, but could have logical significance. Their results showed good qualitative agreement between the predicted velocity profiles and those of the in vivo measurements. Pulsatile flow in a constricted channel was studied by Tutty [22]. Flow patterns have been calculated for pulsatile flows with both sinusoidal and nonsinusoidal flow rates for a range of Reynolds number (Re) and Strauhal number (St). He suggested

that even for relatively low frequency flows a strong vortex wave was generated with a complex wall shear stress distribution and peak values much greater than those found in steady or unsteady parallel flow. He concluded that the strength of the vortex wave increases with increase in Re and St, with its total length and wavelength independent of Re but inversely proportional to St.

Ma, Lee and Wu [23] examined the behavior of nonlinear pulsatile flow of incompressible blood contained in an elastic tube. They characterized the motion of the arterial wall by a set of linearized differential equation. They used finite element method to solve the non-linear system. The results obtained are pressure distribution, velocity profile, and flow rate and wall displacements along the elastic tube. The results showed good agreement with the previously published results.

Preliminary analysis of the effects of blood vessel movement on blood flow patterns in the Coronary arteries was extensively studied by Moore *et al*. [24]. They used a Womersley type solution to determine the effect of axial movement on the wall shear rate in a simplified model of the coronary arteries. They derived pulsatile pressure gradient from previous published coronary artery waveforms. They found that most of the changes in wall shear rate were observed in systole, when the pressure gradient is minimum. Their results indicated that the blood vessel movement during the cardiac cycle has a significant effect on the thermodynamic phenomena, which have been associated with the development of anthersclerosis.

Kobayashi & Pereira [25] presented a computational method for solving arbitrary two-dimensional physiological flows. They concluded that the blood cannot be considered Newtonian for separated flows, even in large blood vessels. They found that the low Reynolds turbulence modeling should be considered for the physiological Reynolds number in arteries. From their results, they predicted that the Minmod scheme represents an impressive improvement over traditional convection discretization schemes, and is recommended for fluid applications, in particular with separated zones and high levels of shear rate in the computational domain.

He and Ku [26] studied the unsteady entrance flow development in a straight tube. The pulsatile entrance flow was solved using a spectral element simulation of the full unsteady Navier-Stokes equation. They observed the variations in the entrance length during the pulsatile cycle. They found that the amplitude of the entrance length variation decreases with an increase in the Womersley parameter .The phase lag between the entrance length and the inlet flow waveform increased for Womersely parameter α up to 5.0 and decreased for α larger than 5. They concluded that for larger arteries, α is high and the entrance length during pulsatile cycle is close to the value corresponding to the mean Reynolds number. However, in medium to small arteries such as the carotid, coronary and femoral arteries, the Womersely numbers are smaller.

Sharp *et al*. [27] analytically studied the effect of blood viscoelasticity on pulsatile flow in stationary and axially moving wall tubes. They calculated the effect of blood viscoelasticity on velocity profiles and shear stress. They calculated the effect of blood viscoelasticity on velocity profiles and shear stress. And it was found that the wall shear

stress differences between viscous and viscoelastic flows in the coronary artery were small, regardless of whether axial vessel motion was included. The shape of the wall shear stress waveform and its difference, however, changed dramatically between the stationary and moving vessel cases. The peaks in wall shear stress difference corresponded with large temporal gradients in the combined driving force for the flow.

Ghalichi, F. *et al*. [28] numerically investigated the blood flow in arterial stenosis using the Wilcox low-Re k-ω turbulence model. They considered three stenosis models with 50%, 75% and 85% reduction in cross-sectional area over a range of physiologically relevant Reynolds numbers. The results obtained were compared with experimental measurements and with the results obtained by the standard k-ω model in tuerms of velocity profile, vortex length, wall shear stress, wall static pressure and turbulence intensity. The comparisons showed that the results predicted by low-Re were in good agreement with the experimental measurements. They concluded that their model is suitable for blood flow in certain areas of the arterial tree where both laminar and transitional /turbulent flows coexist.

A numerical study of blood flow patterns in anatomically realistic and simplified end-to-side anastomoses was studied by Moore *et al*. [29]. They used a human femoral-popliteal bypass graft to reconstruct an anatomically faithful finite element model of an end to side anastomosis. They considered both steady and unsteady flow models for six different geometries. The flow and wall shear stress fields were analyzed to determine the significance of each level of geometric simplification. They concluded that for the specific case of an end to side anastomosis, simplified models provide sufficient information for

comparing hemodynamics with qualitative locations. The ratio of the graft to host artery diameter was shown to be the most important geometric feature. "Secondary" geometric features such as local arterial caliber changes, out of plane curvature, and small-scale surface topology are less important determinants of the wall shear stress patterns.

The analysis of temporal shear stress gradients during the onset phase of flow over a backward–facing step was studied by Haidekkar *et al*. [30]. They computed the wall shear stress action on the bottom plate as a function of time and distance from the sudden expansion. Their results showed that depending on the time for the flow to be established, significant temporal gradients occurred close to the second significant point of flow. They found that in a backward facing step flow chamber, cells were exposed to both temporal & spatial gradients of shear stress they also found that the temporal gradient cause a significant mitogenic response in endothelial cells, which are related to observations at sites of distributed flow in the vascular endothelium.

Finol and Amon [31] performed the numerical predictions of blood flow patterns and thermodynamic stresses in Abdominal Aortic Aneurysm (AAAs) in a two-aneurysm, axisymmetric, rigid wall using the spectral element method. They found that the vortex dynamics induced by pulsatile flow was characterized by a sequence of five different flow phases in one period of the flow cycle. They obtained the higher shear stress and wall shear stress gradient [WSSG] at the peak flow, downstream of both aneurysms. They illustrated the importance of considering time-dependant flow for the evolution of hemodynamic indicators.

Lei *et al*. [32] numerical simulated the pulsatile flow in a canine distal graft anastomosis model using the finite element method and compared the results with experimental data obtained using Laser Doppler Velocimetry (LDV). These comparisons showed good agreement for velocity profiles with some clear differences near the recirculation zones during the deceleration and reverse-flow segments of the flow waveform. Wall shear stresses were determined form velocity gradients, whether by computational or experimental methods. From the wall shear stress numerical results, they computed four variables that have been cited in the development of intimal hyperplasia-the time averaged wall shear stress, an oscillation shear index, and spatial and temporal wall shear stress gradients-in order to illustrate the versatility of numerical methods. They concluded that computational approach is valid alternative to the experimental approach for quantitative hemodynamics studies.

The blood flow dynamics of end to end native arteriovenous fistulas (AVF) was numerically studied by En-lordache *et al*. [33] using computational fluid dynamics (CFD). They generated three-dimensional mesh using digital subsrtraction angiographies of an AVF for numerical analysis of blood flow. They considered the blood as a non-Newtonian fluid using the shear-thinning model of Carreau. They calculated the wall shear stresses at different zones. It was found that the shear stress was high on the inner surface of the bending zone, on the venous side, proximal to the anastomosis. Shear stress was oscillating between negative and positive values, while distal from the anastomosis, wall shear stress returned with the physiologic range. Areas of the vessel wall with very high

shear stress were identified on the bending zone of the radial artery and the venous side, after the arteriovenous shunt. And also secondary flows were observed in these regions.

A three-dimensional computational investigation of the effect of proximal artery flow on the hemodynamics at the distal anastomosis of a vascular bypass graft was studied by Kute and Vorp [34]. They used the finite volume method to solve the full Navier-Stokes equations for steady flow through an idealized geometry of the distal anastomosis. They calculated the flow field, local wall shear stress (WSSL & WSS gradient WSSG) everywhere in the domain. They also calculated the severity parameter (SP), a quantification of a hemodynamic variation, at the anastomosis. Their results suggested that the flow condition in the proximal artery is an important determinant of the hemodynamics at the distal anastomosis of end to side vascular bypass graft.

Prakash and Ross Ethier [35] investigated the requirements for mesh resolution in 3D computational hemodynamics. They used a well-validated Navier Stokes solver to simulate in an anatomically realistic human right coronary artery (RCA) using unstructured high order tetrahedral finite element meshes. They used adaptive mesh refinement (AMR) methodology to perform the calculations. They concluded that the RCA model used in their study requires about 325,000 nodes to achieve mesh independence, and about 190,000 nodes to obtain less than a 10 percent spatial discretization error in the outer wall, wall shear stress distribution (WSS). They suggested that the AMR approach has the important benefit of providing a systematic framework that allows mesh-independence to eventually be obtained, while manual mesh generation does not provide such a framework.

The effect of blood velocity pulsations on bioheat transfer in two-dimensional straight rigid blood vessel was numerically studied by Craciunescu & Clegg [36]. Their results showed that the pulsating axial velocity produces a pulsating temperature distribution, reversal of flow occurs in aorta and in large vessels, which produces significant time variation in the temperature profile. They found that for the thermally important terminal arteries velocity pulsations have a small influence on temperature distribution and on the energy transport out of the vessels. They concluded that, for estimating bioheat transfer it is reasonable to assume a non-pulsating blood velocity.

A systematic study of pulsatile flow in a stenosed channel has been numerically studied in terms of waveform dependence on physiological pulsation by Liu and Yamaguchi [37]. The results were obtained for unsteady flows downstream of the stenosed portion with variation in the waveforms of systole and diastole. They observed a train of propagating vortex waves, which showed great sensitivity to the waveforms. They found that the generation and development of the vortex waves might be linked to the presence of an adverse pressure gradient within a specific interval between two points of inflection at the systolic waveform. They concluded that adverse pressure gradient consists of a global pressure gradient that is found to closely related to the dynamics of pulsation, and a local pressure gradient, which is observed to be dominated by nonlinear vortex dynamics.

The computational analysis of coupled blood-wall arterial LDL transport was studied by Stangeby and Ethier [38]. They modeled the fluid flow with in the lumen & wall of a constricted, axisymmetric tube simulating a stenosed artery, and used this flow

pattern to study low-density lipoproteins (LDL) mass transport from the blood to the artery wall. Their results showed an elevated LDL concentration downstream side of stenosis. Stroud *et al*. [39] carried out numerical analysis of flow through a severely stenotic carotid artery bifurcation. They considered both steady and pulsatile flow conditions for different Reynolds numbers. They found that both dynamic pressure and wall shear stress were very high, proximal to the stenosis throat in the internal carotial theory. They also observed vortex shedding downstream of the most severe occlusion. They found the Chien turbulence model was better than the Goldberg k-ε turbulence model.

Pulsatile turbulent flow in stenotic vessels has been numerically modeled using the Reynolds-averaged Navier-Stokes equation approach by Varghese and Frankel [40]. Two different experiments were modeled involving pulsatile flow through axisymmetric stenoses. Four different turbulence models were employed to study their influence on the results. It was found that the low Reynolds number k-ω turbulence model was in better agreement with previous experimental measurements than both the low and high Reynolds number versions of the RNG (renormalization-group theory) k-ε turbulence model and the standard k-ε model, with regard to predicting the mean flow distal to the stenosis including aspects of the vortex shedding process and the turbulent flow field. All models predicted a wall shear stress peak at the throat of the stenosis with minimum values observed distal to the stenosis where flow separation occurred.

A new one-dimensional model for the calculation of steady and unsteady flow through an indented two-dimensional channel with separation and reattachment point was

studied by Kalse *et al*. [41]. The new model was based on an interactive boundary layer flow near the channel walls and for an inviscid core flow were solved simultaneously. The advantage of this model was that this approach does not require semi-empirical inputs, such as location of separation and reattachment. Based on the results for a steady flow through symmetrically indented channel, the model showed promising results.

The accuracy and reproducibility of CFD prediction based on images acquired using three-dimensional ultrasound was studied by Augst *et al*. [42]. A human carotid artery bifurcation phantom was scanned three times using 3D ultrasound in order to assess accuracy and reproducibility of the procedure from image acquisition to reconstruction to CFD simulation. The geometry was reconstructed and flow simulation were carried out on the three sets as well as on a model generated using computer aided design (CAD) from the geometric information given by the manufacturer. Flow simulations were carried out for four model under pulsatile flow conditions using a non-Newtonian blood-mimicking fluid model, namely the Quemada model. It was found that the tree reconstructed sets showed good reproducibility as well as satisfactory quantitative agreement with the CAD model.

2.2.2. Flow in Deforming Channels

Ralph and Pedley [43] numerically studied the unsteady flow of viscous, incompressible fluid flow in a channel with moving indentation in one wall. They modified the stream function-vorticity equation and a finite difference solution scheme to obtain a solution for laminar flow in a channel with moving indentation. Downstream of

the moving indentation, it was found that the flow in the center of the channel becomes wavy, and eddies are formed between the waves crests/troughs and the walls. Eddy doubling process was explained in detail.

The flow in a channel with an oscillating constriction was investigated by Ralph and Pedley [44] using the numerical solution of Navier-Stokes and Euler equations. They observed a vorticity wave downstream of the constriction in both viscous and Inviscid flow, whether the downstream flow rate was held constant and the upstream flow was pulsatile, or vice versa. Closed eddies were observed between the crests/troughs of the wave and the walls, in the Euler solutions as well as the Navier-Stokes flows, although their structures were different in the two cases.

Demirdzic and Peric [45] developed a finite volume method for prediction of fluid flow in arbitrarily shaped domains with moving boundaries. The method is both Lagrangian and Eulerians since the numerical mesh may move with the fluid (Lagrangian approach), be held fixed (Eulerian approach) or be moved in any other prescribed way. The method uses the integral form of the governing equations for an arbitrary moving control volume, with pressure and Cartesian velocity components as dependent variables. They have validated their method with the experimental results available in the literature.

The nonlinear analysis of flow in elastic tube when subjected to an oscillatory pressure gradient was studied by Wang and Tarebell [46]. They used perturbation techniques to solve the nonlinear version of the problem. They assumed that the wall motion is small. Their results indicated that nonlinear convective acceleration induces finite mean pressure gradient and mean wall shear rate even when no mean flow occurs. It

is shown that the induced mean wall shear rate is proportional to Womersley unsteadiness parameter (α), where α is large. In addition, they also observed that the steady flow structure in the core could be influenced by wave reflection. Johnson *et al*. [46] numerically studied pulsatile flow in a uniform deformable vessel. They calculated the shear rates and velocity profiles in relatively short, uniform segments of arteries, such as canine artery. Tutty and Pedley [48] analytically studied the flow in a non-uniform channel. A small amplitude inviscid theory was derived in which the force displacement of the streamlines was governed by a linearized Kortweg-de Vries equation. Shim and Kamm [49] numerically simulated flow through compliant tubes with linear tapes in wall thickness using finite element analysis. Computational results for an axisymmetric tube show that as the cross-sectional area decreases with the reduction in downstream pressure, the flow rate increases and reaches a maximum.

Recently, Zhao and Ahmed. [50] developed a general method for simulation of fluid flows with moving and compliant boundaries on unstructured grids using Arbitrary Lagrangian Eulerian (ALE) approach. A high-order upwind characteristics-bases finite volume scheme and an implicit dual time stepping method mesh was employed for the simulation of unsteady flows and the fluid-structure interaction. Furthermore, they have adopted a new dynamic mesh method to handle the large deformation of the flow field. The dynamic mesh method and the solver are validated for an unsteady channel flow with a moving indentation. It is observed that the dynamic mesh method is very robust and able to handle large deformation without excessive distortion of the dense mesh near the wall. They have also solved the membrane equation by the same implicit dual time stepping

scheme for improved stability and efficiency in order to calculate the arbitrary wall movement and variable tension along the membrane.

Effects of wall motion and compliance on flow patterns in the ascending Aorta was investigated by Jin *et al* [51]. They conducted a computational Fluid Dynamics (CFD) study using the vascular geometry and vessel movement obtained in vivo from magnetic resonance imaging (MRI) to simulate flow patterns in the ascending aorta. MRI derived geometry and velocities were imposed as boundary conditions, which included both radial expansion contraction and translational motion of the wall. It was found that the computed results were in agreement with the MR data only when full wall motion was included in the model, suggesting that the flow patterns observed in the ascending aorta arise not only from the geometric curvature of the arch but also from the motion of the aorta resulting form its attachment to the beating heart.

2.3. Rheological Investigations

In most of the studies mentioned above, the flowing blood is assumed to be Newtonian. The assumption of Newtonian behavior of blood is acceptable for high shear rate flow, It is not, however, valid when the shear rate is low as is the flow in smaller arteries and in the downstream of the stenosis. It has been pointed out that in some diseased conditions, blood exhibits remarkable non-Newtonian properties. Thurston [52] has shown that blood, being a suspension of enumerable number of cells, possesses significant viscoelastic properties in the frequency range of physiological importance.

Deutsch and Phillips [53] experimentally studied the red cell suspensions and blood plasma to small disturbances in circular Coutte flow for the stability of human blood. They confirmed the viscoelastic nature of whole blood and blood cell suspensions. They found that the blood plasma to be Newtonian. They identified two mechanisms by which elasticity may arise in blood namely red cell deformability and red cell aggregation. Liepsch and Morvec [54] investigated the flow in a right 90° bifurcation under steady flow conditions. They found a striking influence of the non–Newtonian properties of polyacrylamide solution on the axial velocity distribution. Especially the size and the location of the region of flow reversal were affected by the non-Newtonian properties of the fluid. Ku and Liepsch [55] studied the axial velocity distribution in a 90° bifurcation under pulsatile flow conditions, also using polyacrylamide solution. They found a reduction of the size of the region with flow reversal for the non-Newtonian fluid in a rigid model. It has to be remarked though, that polyacrylamide solution is much more elastic than blood.

The laminar steady and nonsteady flow of non-Newtonian fluids through a tube was studied by Theodorou and Bellet [56]. Velocity distribution, the pressure drop along the tube and the wall stress were determined. Nakamura and Swada [57] numerically studied the laminar steady flow of non-Newtonian fluid through an axisymmetric stenosis using the finite element methods. The results showed that the non-Newtonian property of blood decreases the axial force acting on the stenosis. The role of non-Newtonian characteristics (such as shear rate dependent viscosity and viscoelasticity) on flow behavior across the sudden expansion step in a circular pipe was investigated by Pak *et.al*

[58] for a wide range of Reynolds numbers including the turbulent flow. The reattachment lengths for the viscoelastic fluids in the laminar flow regime are found to be much shorter than those for the Newtonian fluid. However, in the turbulent flow regime, the reattachment length for the viscoelastic fluids is tow or three times longer than those for water, and gradually increases with increasing concentration of viscoelastic solutions.

The effect of nonaxisymmetric hematocrit distribution on the flow of human and cat blood in small blood vessels of the microcirculation was studied by Das *et al* [59]. Human blood was described by Quemada's rheological model and the cat blood was described by Casson's model. Investigation of the non-Newtonian steady flow in a carotid bifurcation model by Gijsen *et al.* [60-61] indicated that the shear thinning is the dominant non-Newtonian property of blood and the viscoelasticity may be ignored for the prediction of the velocity distribution.

Hussain *et al*. [62] investigated the qualitative analysis of parameters that affect apparent blood viscosity at different low shear rates. i.e. between $1s^{-1}$ and 100 s^{-1}. Viscosity profile of a large number of blood samples from thromboembolic stroke cases and age and sex matched health controls were studied which confirmed non-Newtonian power law behavior of blood. The power law coefficients, n and k, which are unique to each blood sample, were related with blood viscosity parameters in the form of a mathematical equation by performing non-linear regression analysis. The calculation of n and k of a blood sample using the equation of obtained, provided a quick information on its apparent viscosity values at any given shear rate without visocometry. The calculated

and the experimental viscosity were found in good agreement within a permissible error range.

Buchanan *et al*. [63] studied the rheological effects on pulsatile hemodynamics in a stenosed tube. They considered a transient laminar axisymmetric flow through a tube with a smooth local area of reduction of 75%. The influences of three rheology models (i.e. Newtonian, power law and Quemada) were investigated using an experimentally validated control volume method. Three Womersley numbers were compared for a sinusoidal input with a mean Reynolds number of 200. The results showed that for the highest Womersley number considered, a second co-rotating vortex was formed distal to the primary vortex. It was found that the shear-thinning rheological models have a secondary effect on the flow field that primary appears in terms of subtle changes to the hemodynamic wall parameters. The non-Newtonian models affected the entrainment of fluid like particles in the post-stenotic region measurably. The particle residence time (PRT), defined as the ratio of transient to steady residence times, was found to be less than or equal to unity for the majority of fluid elements for all rheologies and Womersley numbers considered.

Shalman *et al.* [64] established a relationship between actual hemodynamic conditions and the parameters that define stenosis severity in the clinical setting in stenosed coronary artery. A constant flow regulation mechanism resulted in coronary flow reserve (CFR) and fractional flow reserve (FFR) values that were within the physiological range, while a constant wall-shear stress model yielded unrealistic values. Neofytou and Drikakis [65] numerically investigated the instability of non-Newtonian flow in a channel

with a sudden expansion. Three non-Newtonian models, Casson, Power-Law and Quemada models were employed. Two groups of three cases were considered for all the models. In the first group were the cases of constant *Bi*=0.1,0.06 and 0.02 and varying Re and in the second group were the cases of constant *Re*=400,500, and 600 and varying *Bi.* Three stages of transition from symmetric to asymmetric condition are observed for all the models. The length of the vortices at the point of transition from symmetry to asymmetry is the same for all three non-Newtonian models. Chen and Liu [66] numerically investigated the influence of the non-Newtonian property of fluid as well as of curvature and out-of-plane geometry in the non-planar daughter vessel on wall shear stress (WSS) and flow phenomena. The results supported that the non-planarity of blood vessels and the non-Newtonian properties of blood are an important factor in hemodynamics and may play a significant role in vascular biology and pathophysiology. Recently, Mandal [67] numerically solved the problem of non-Newtonian and non-linear blood flow through a stenosed artery. The non-Newtonian behavior of the streaming blood is characterized by the generalized Power-law model. The model was employed to study the effects of the taper angle, wall deformation, severity of the stenosis within its fixed length, steeper stenosis of the same severity, nonlinearity and on-Newtonian rheology of the flowing blood on the flow field.

2.4. Objectives of the Present Work

Based on the cited literature, it can be concluded that no work was published on the subject of blood flow in an axisymmetric tube with a moving indentation, which closely

resembles the flow in arteries and veins. The overall objective of this study is to simulate blood flow inside a tubular passage, which has a time varying shape. The simulation is to be carried out numerically by using an appropriate Computational Fluid Dynamics (CFD) model. This task will be achieved by assuming the blood as a Newtonian fluid and later attempting a more realistic model. In this regard, the thesis is directed towards achieving the following tasks:

1. Choosing and Setting up a numerical model for the time dependent blood flow in a moving indented 2D channels.

2. Validation of the above model, with an experimental data available in the literature Pedley [14].

3. Simulating new cases for an axisymmetric tube with a moving indentation considering the following parameters:

    a) Varying the frequency of the moving indentation.

    b) Introducing the steady and pulsatile flow at the inlet.

    c) Considering the Newtonian and non-Newtonian effects of the blood.

Hence, the result of the study is expected to contribute to the literature in this field and enhance the understanding of blood flow in arteries and veins.

CHAPTER 3

MATHEMATICAL MODELLING

In order to attempt to model blood flow, the problem must be restricted to a specific area. As the order of magnitude of the problem increases or decreases, many assumptions made initially fail to hold. Flow in arteries can be considered a continuum. That is, the elements of blood seem to be continuous with each other, with no empty spaces in between. In fact, even though blood is composed of many different elements, the continuum hypothesis implies that every "point" in the fluid represents a fluid element, and that the properties at that point, represent the properties of that fluid element.

3.1. Problem Statement and Boundary Conditions

In the present study two different geometries are simulated:

3.1.1. Two-Dimensional Planar With a Moving Indentation-Validation of the Computational Model

3.1.1.1. Description of the Problem

The first problem considered is that of 2-D flow in a channel with a moving indentation as shown in Figure 3.1. The shape of the indentation is the same as that considered by Ralph and Pedley [43]. The time varying height of the indentation is given by:

$$y_w(x,t) = \begin{cases} h(t) & for\ 0 < x < x_1 \\ 0.5h(t)\{1-\tanh[a(x-x_2)]\} & for\ x_1 < x < x_3 \\ 0 & for\ x > x_3 \end{cases} \tag{3.1}$$

$$h(t) = 0.5h_{\max}[1-\cos(\omega t)] \tag{3.2}$$

where $a = 4.14, x_1 = 4b, x_3 = 6.5b, x_2 = 0.5(x_1 + x_3)$. Here ω is the radial frequency $2\pi/t_0$, t_0 is period of oscillation of the moving indentation, b is the unblocked channel height and is taken as 1cm. The maximum blockage of the channel cross section is $h_{\max}(= 0.38b)$ occurs at the middle of the period. The geometry of the indentation is symmetric around $x = 0, i.e.\ y(-x) = y(x)$. The indentation accelerates into the channel for the first quarter of the period and goes on advancing but decelerates in the second quarter of the

period. It accelerates towards the wall for the third quarter of the period, and then decelerates back to its flush position in the final quarter of the period.

3.1.1.2. Governing Equations

In order to write the governing equations in dimensionless form, we first introduce the following dimensionless variables,

$$U = \frac{u}{U_0},\ V = \frac{v}{U_0},\ P = \frac{p}{\rho U_0^{\,2}},\ X = \frac{x}{b},\ Y = \frac{y}{b},\ \tau = \frac{t}{t_0} \tag{3.3}$$

where u and v are the dimensional velocity components in x and y directions respectively, p is the pressure, t is time, U_0 is the average velocity at the inlet and ρ is the density of the fluid. The governing equations can be expressed as:

Conservation of Mass

$$\frac{\partial U}{\partial X} + \frac{\partial V}{\partial Y} = 0 \tag{3.4}$$

Conservation of X-momentum

$$\frac{1}{2\pi}\frac{\alpha^2}{\mathrm{Re}}\frac{\partial U}{\partial \tau} + U\frac{\partial U}{\partial X} + V\frac{\partial U}{\partial Y} = -\frac{\partial P}{\partial X} + \frac{1}{\mathrm{Re}}\left[\frac{\partial^2 U}{\partial X^2} + \frac{\partial^2 U}{\partial Y^2}\right] \tag{3.5}$$

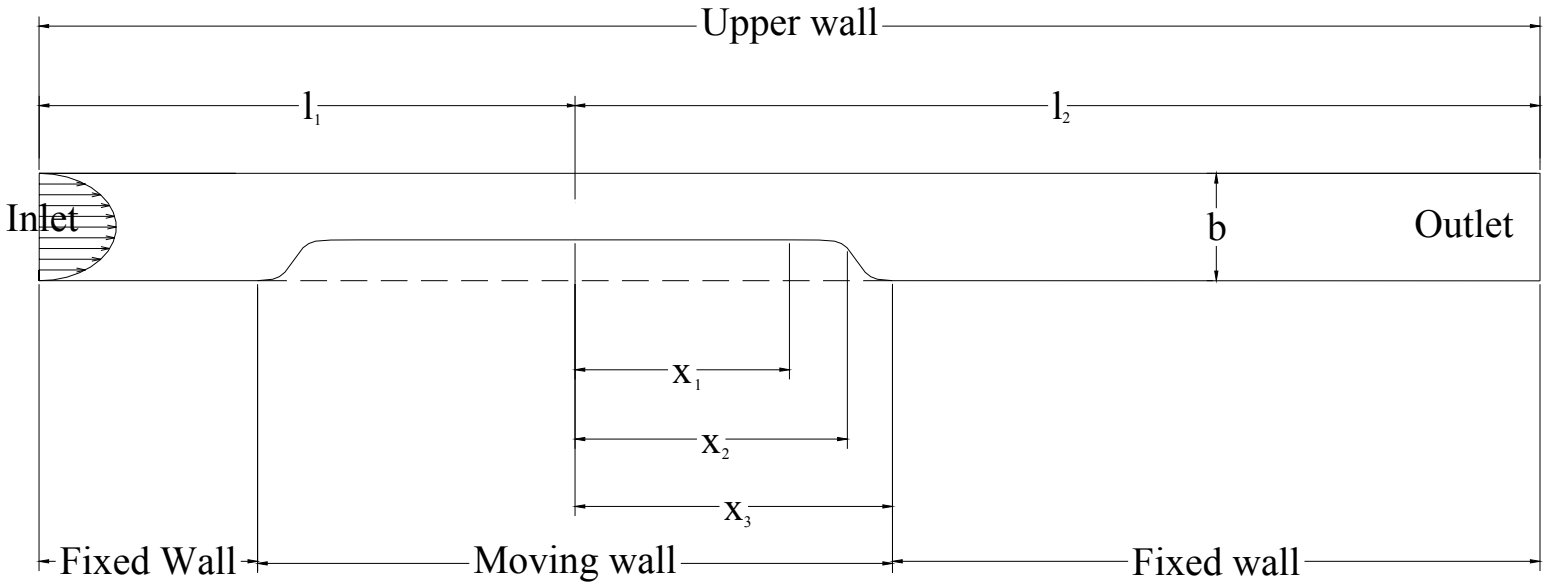

Figure 3.1 Geometry of 2-D moving indented channel (not to sale): $b = 1cm,\ l_1 = 10cm, l_2 = 18cm$.

Conservation of Y-momentum

$$\frac{1}{2\pi}\frac{\alpha^2}{\mathrm{Re}}\frac{\partial V}{\partial \tau}+U\frac{\partial V}{\partial X}+V\frac{\partial V}{\partial Y}=-\frac{\partial P}{\partial Y}+\frac{1}{\mathrm{Re}}\left[\frac{\partial^2 V}{\partial X^2}+\frac{\partial^2 V}{\partial Y^2}\right] \tag{3.6}$$

where Re is the Reynolds number based on the channel height and α is the Womersley parameter respectively which are defined as

$$\mathrm{Re}=\frac{U_0 b}{\upsilon},\quad \alpha=b\sqrt{\frac{\omega}{\upsilon}} \tag{3.7}$$

where υ is the kinematic viscosity of the fluid. It should be noted that Ralph and Pedley [43] have defined the non-dimensional frequency using the Strouhal number.

$$St=\frac{b}{U_0 t_0}=\frac{\alpha^2}{2\pi\,\mathrm{Re}} \tag{3.8}$$

Here, we have used the Womersly parameter 'α' which is more commonly used (Liepsch and Morvec, [54] for similar situations.

At the start of fluid motion (τ=0), the flow is assumed to be steady and fully developed in the entire flow domain and the velocity components are given by

$$U(X,Y)=6Y(1-Y);\qquad V(X,Y)=0\qquad at\quad \tau=0 \tag{3.9}$$

The boundary conditions are expressed in terms of the conditions at inlet, at the walls and at exit of the flow domain. The velocity profile at inlet (X=-l_1/b) is assumed to be parabolic and invariant with time, thus

$$U(X=-l_1/b, Y, \tau) = 6Y(1-Y); \qquad V(X=-l_1/b, Y, \tau) = 0 \tag{3.10}$$

At the stationary wall (Y=1), the no slip condition is applied while the velocity components at the moving indentation are derived from equations (3.1) and (3.2). These are expressed as:

$$U = 0; \quad V = 0 \qquad \text{at} \quad Y=1 \tag{3.11 a}$$

$$U=0;\ V=0.5\omega h_{max} Sin(\omega t) \text{ at } Y=y_w/b \text{ and } 0<X<X_1 \tag{3.11 b}$$

$$U = \frac{-V}{0.095 a Sec^2 h[ab(X-X_2)](1-Cos(2\pi\tau))}\ ; \tag{3.11 c}$$

$$V = \frac{0.596905}{U_0 t_0}\left[1 - Tanh[ab(X-X_2)]\right] Sin(2\pi\tau) \text{ at } Y=y_w/b \text{ and } X_1<X<X_3 \tag{3.11 d}$$

At the exit section, the pressure distribution is considered to be constant, thus

$$P = P_{amb} (=0) \qquad \text{at } X=l_2/b \tag{3.12}$$

3.1.2. Axisymmetric Flow In A Tube With A Moving Indentation

3.1.2.1. Description of the Problem

The problem considered is that of two-dimensional axisymmetric flow in a tube of circular cross section as shown in Figure 3.2. Here the upstream and downstream lengths are 10cm and 18cm respectively. The time varying shape of the indentation is given by the analytic function,

$$r_w(x,t) = \begin{cases} r_0 - h(t) & for\ 0 < x < x_1 \\ r_0 - 0.5h(t)\{1 - \tanh[a(x - x_2)]\} & for\ x_1 < x < x_3 \\ r_0 & for\ x > x_3 \end{cases} \tag{3.13}$$

$$h(t) = 0.5h_{\max}[1 - \cos(\omega t)] \tag{3.14}$$

where $a = 4.14, x_1 = 4b, x_3 = 6.5b, x_2 = 0.5(x_1 + x_3)$, r_0 is the radius of the tube and is taken as 1cm. The maximum blockage of the tube cross-section $h_{\max}(= 0.38r_0)$ occurs at $\tau = 0.5$. The geometry of the indentation is symmetric around $x = 0, i.e.\ r(-x) = r(x)$.

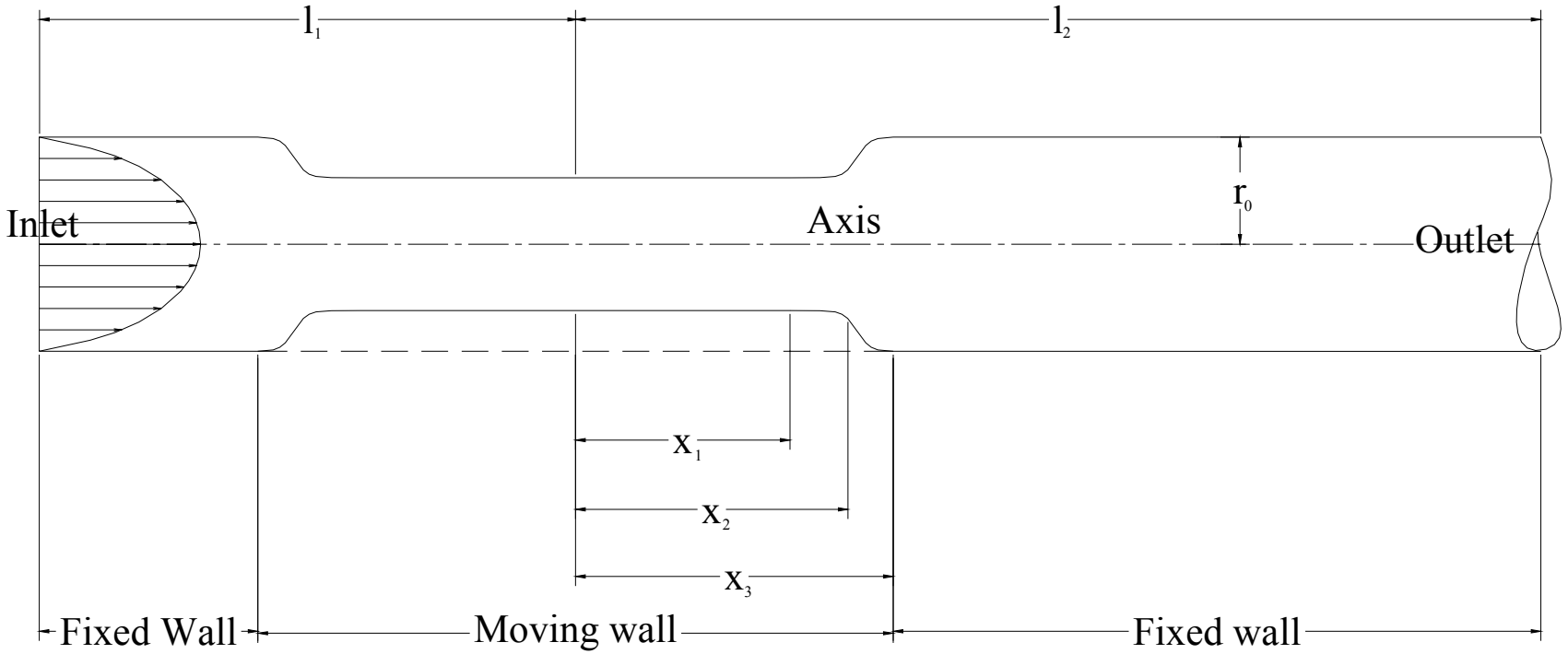

Figure 3.2 Geometry of 2-D axisymmetric tube with moving indentation (not to scale): $r_0 = 1cm,\ l_1 = 10cm, l_2 = 18cm$.

3.1.2.2. Governing Equations

Using the nondimensional variables,

$$U = \frac{u}{U_0}, V = \frac{v}{U_0}, P = \frac{p}{\rho U_0^{\,2}}, X = \frac{x}{r_0}, R = \frac{r}{r_0}, \tau = \frac{t}{t_0} \tag{3.15}$$

where u and v are the dimensional velocity components in x and r direction respectively, p is the pressure, t is the time, U_0 is the average velocity at the inlet, r_0 is the radius of the tube, ρ is the density of the fluid; the governing equations have the following form:

Conservation of Mass

$$\frac{\partial U}{\partial X} + \frac{1}{R}\frac{\partial (RV)}{\partial R} = 0 \tag{3.16}$$

Conservation of X-momentum

$$\frac{1}{\pi}\frac{\alpha^2}{\mathrm{Re}}\frac{\partial U}{\partial \tau} + U\frac{\partial U}{\partial X} + V\frac{\partial U}{\partial R} = -\frac{\partial P}{\partial X} + \frac{2}{\mathrm{Re}}\left[\frac{\partial^2 U}{\partial X^2} + \frac{\partial^2 U}{\partial R^2} + \frac{1}{R}\frac{\partial U}{\partial R}\right] \tag{3.17}$$

Conservation of r-momentum

$$\frac{1}{\pi}\frac{\alpha^2}{\mathrm{Re}}\frac{\partial V}{\partial \tau} + U\frac{\partial V}{\partial X} + V\frac{\partial V}{\partial R} = -\frac{\partial P}{\partial R} + \frac{2}{\mathrm{Re}}\left[\frac{\partial^2 V}{\partial X^2} + \frac{\partial^2 V}{\partial R^2} + \frac{1}{R}\frac{\partial V}{\partial R} - \frac{V}{R^2}\right] \tag{3.18}$$

where Re is the Reynolds number based on the tube diameter and α is the Wormersley, parameter which are defined as

$$\mathrm{Re} = \frac{2U_0 r_0}{\upsilon}, \quad \alpha = r_0\sqrt{\frac{\omega}{\upsilon}} \tag{3.19}$$

where υ is the kinematic viscosity of the fluid.

At the start of motion (τ=0), a steady Poiseuille flow with an average velocity U_0 is assumed at the entrance of the flow domain, thus

$$U(X,R) = 2(1-R^2);\ V(X,R) = 0 \qquad at \qquad \tau = 0 \tag{3.20}$$

The boundary conditions are expressed in terms of the conditions at inlet, at the walls and at exit of the flow domain. The velocity profile at inlet (X=-l_1/b) is assumed to be parabolic and invariant with time for the steady inlet cases, thus

$$U(X = -l_1/b, R, \tau) = 2(1-R^2); \quad V(X = -l_1/b, R, \tau) = 0 \tag{3.21 a}$$

For the unsteady inlet case, the input pulse selected is sinusoidal i.e.

$$U(X = -l_1/b, R, \tau) = 2(U_0 + U_m Sin(\omega t))\left(1-\left(\frac{r}{r_0}\right)^2\right); V(X = -l_1/b, R, \tau) = 0 \tag{3.21 b}$$

At the stationary wall ($R=1$), the no slip condition is applied while the velocity components at the moving indentation are derived from equations (3.13) and (3.14). These are expressed as:

$$U = 0; \quad V = 0 \quad \text{at} \quad R=1 \tag{3.22 a}$$

$$U=0;\ V=0.5\omega h_{max} Sin(\omega t) \text{ at } R=r_w/r_0 \text{ and } 0<X<X_1 \tag{3.22 b}$$

$$U = \frac{-V}{0.095 a Sec^2 h[ar_0(X - X_2)](1 - Cos(2\pi\tau))}; \tag{3.22 c}$$

$$V = \frac{0.596905}{U_0 t_0}\left[1 - Tanh[ar_0(X - X_2)]\right] Sin(2\pi\tau) \text{ at } R=r_w/r_0 \text{ and } X_1<X<X_3 \tag{3.22 d}$$

At the exit section, the pressure distribution is considered to be constant, thus

$$P = P_{amb} (=0) \qquad \text{at } X=l_2/b \tag{3.23}$$

At the axis,

$$V = 0 \text{ and } \frac{\partial U}{\partial R} = 0 \quad \text{at } R=0 \tag{3.24}$$

3.2. Blood Rheology

Early investigators conceptualized blood as a viscous fluid, assuming that the viscosity controls its flow properties. But blood is not a fluid in the ordinary sense; it is a fluidized suspension of elastic cells. In 1972, G. B. Thurston was the first to measure the viscoelastic properties that control the pulsatile flow of blood. The viscoelasticity reflects the cumulative effects of many blood parameters such as plasma viscosity, red blood cell deformability, aggregation, and hematocrit.

Fluids that cannot be described by the Navier-Stokes Equation are called non-Newtonian fluids. Further, if these fluids possess elastic properties as well as viscous properties, then they are called viscoelastic fluids. Mathematical models for viscoelastic fluids are constantly being developed and tested in an attempt to improve the modeling process for these fluids. Two differential models for viscoelastic fluids are:

3.2.1. The UCM Model

The Maxwell model for the flow of a viscoelastic fluid is a linear model put forward by Maxwell J. C., in 1867. When this model is generalized to arbitrary flows by putting it in tensor form, and the upper convected time derivative is used in place of the partial time derivative, one obtains the quasi-linear Upper Convected Maxwell model, or UCM model. The constitutive equation for this model is given below:

$$\lambda \overset{\nabla}{\tau} + \tau = 2\eta D \tag{3.25}$$

Where λ is the relaxation time of the fluid, η is the viscosity of the fluid and D is the rate of Deformation of tensor given here as

$$D = \frac{1}{2}(\nabla u + \nabla u^T) \tag{3.26}$$

$\overset{\nabla}{\tau}$ is the upper convected time derivative of the stress tensor, defined by:

$$\overset{\nabla}{\tau} = \frac{\partial \tau}{\partial t} + (u.\nabla)\tau - \nabla u.\tau - \tau.(\nabla u)^T \tag{3.27}$$

The value of the relaxation time indicates the extent of the elastic component of the fluid. As the relaxation time increases, so the elasticity of the fluid increases. A relaxation time of zero retrieves the Newtonian constitutive equation.

3.2.2. THE Oldroyd-B Model

In 1929, Jeffreys. H., put forward the Jeffreys model. When the partial time derivatives in this model are replaced by upper convected time derivatives, one obtains the quasi-linear Oldroyd-B model. The constitutive equation for this model is given below:

$$T + \lambda_1 \overset{\nabla}{T} = 2\eta(D + \lambda_2 \overset{\nabla}{D}) \tag{3.28}$$

Where λ_1 and λ_2 are respectively the relaxation and retardation times of the fluid, η is the zero shear-rate-viscosity of the fluid, D is the rate of deformation tensor given here as

$$D = \frac{1}{2}(\nabla u + \nabla u^T) \tag{3.29}$$

T is the extra stress tensor and may be decomposed as

$$T = \tau + 2\eta_2 D \tag{3.30}$$

where τ satisfies the UCM model

$$\lambda_1 \tau + \tau = \overset{\nabla}{\tau} + 2\eta D \tag{3.31}$$

$\eta_1$and η_2 are defined by

$$\eta = \eta_1 + \eta_2, \ \lambda_2 = \frac{\eta_2}{\eta_1}\lambda_1 \tag{3.32}$$

$\overset{\nabla}{T}$ is the upper-convected derivative of *T*, $\overset{\nabla}{D}$ is the upper-convected derivative of *D*.

It can be shown that the Oldroyd-B model is equivalent to a linear combination of the UCM model and the Newtonian model. If the relaxation time and retardation time are equal, then the model is equivalent to the Newtonian model, with the viscosity of the Newtonian fluid equal to the zero-shear-rate viscosity of the Oldroyd-B fluid. If the relaxation time is equal to zero, one obtains the model for a second order fluid with vanishing normal stress coefficient. If the retardation time is equal to zero, the UCM model is retrieved.

Blood is considered to be non-Newtonian and the shear stress of flowing blood is often expressed with relations like

$$\sqrt{\tau} = \sqrt{\tau_y} + k\sqrt{\dot{\gamma}} \tag{3.33}$$

Where $\dot{\gamma}$ is strain rate (du/dy), τ_y is a constant that is the yield stress in shear and κ is an experimental constant. Graphically,

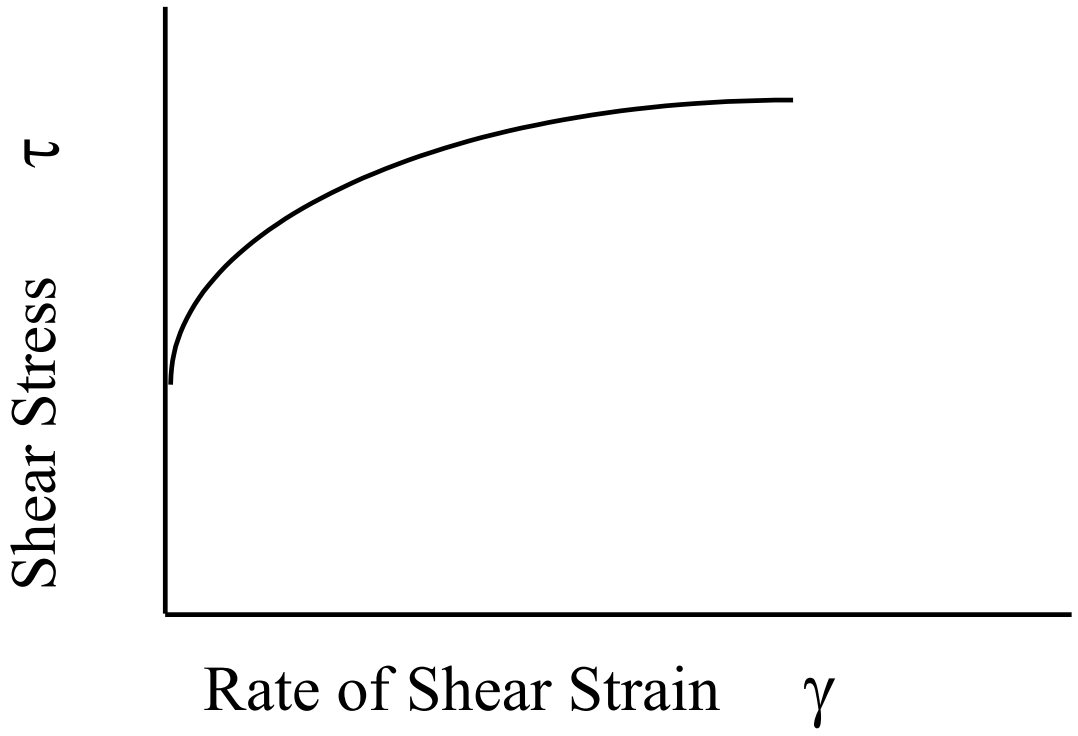

Figure 3.3 Graph between shear stress Vs Rate of Shear Strain.

3.3. Newtonian and Non-Newtonian Fluid

A Newtonian fluid is one, which exhibits the following property. The shear stress, or resisting force τ, and velocity gradient, or rate of deformation $\frac{du}{dy}$, are linearly related by

$$\tau = \mu \frac{du}{dy} \tag{3.34}$$

where μ is the coefficient of viscosity.

A non-Newtonian fluid is a fluid in which the viscosity changes with the applied shear force. As a result, non-Newtonian fluids may not have a well-defined viscosity. For non-Newtonian fluids, the shear stress can be written in terms of non-Newtonian viscosity η:

$$\overline{\overline{\tau}} = \eta(\overline{\overline{D}})\overline{\overline{D}} \tag{3.35}$$

where η is a function of the shear rate $\dot{\gamma}$ and $\overline{\overline{D}}$ is a rate of deformation tensor and is defined by

$$\overline{\overline{D}} = \left(\frac{\partial u_j}{\partial x_j} + \frac{\partial u_i}{\partial x_j} \right) \tag{3.36}$$

$\dot{\gamma}$ is also related to the second invariant of $\overline{\overline{D}}$ and is defined as

$$\dot{\gamma} = \sqrt{\overline{\overline{D}} : \overline{\overline{D}}} \tag{3.37}$$

3.4. Non-Newtonian Models

3.4.1. Non-Newtonian Power Law

The apparent whole blood viscosity, which is the ratio of shear stress to shear rate at a particular rate of shear, can be expressed as

$$\eta = \begin{cases} \eta_{\min} & for\ \dot{\gamma} > \dot{\gamma}_{\max} \\ k\dot{\gamma}^{n-1} & for\ \dot{\gamma}_{\min} < \dot{\gamma} < \dot{\gamma}_{\max} \\ \eta_{\max} & for\ \dot{\gamma} < \dot{\gamma}_{\min} \end{cases}$$

where k is the average viscosity of the fluid (the consistency index), n is a measure of the deviation of the fluid from Newtonian (power-law index).

shows the variation of viscosity with shear rate according to the non-Newtonian power law. Here $\eta_{\min}$ and $\eta_{\max}$ are respectively, the lower and upper limits of the power law. The figure shows the how the viscosity is limited by $\eta_{\min}$ and $\eta_{\max}$ at low and high shear rates.

The power law model is know to be limited to approximately three decades of accuracy and for the rheological data here $\dot{\gamma}_{\max} = 100\,s^{-1}$ and $\dot{\gamma}_{\min} = 10\,s^{-1}$. Table 3.1 shows the non-Newtonian model parameters.

Table 3.1 Non-Newtonian Power-Law model parameters

Parameters	List
η_∞ (kg/m-s)	0.0032
η_0(kg/m-s)	0.02
k	0.1086
n	0.735

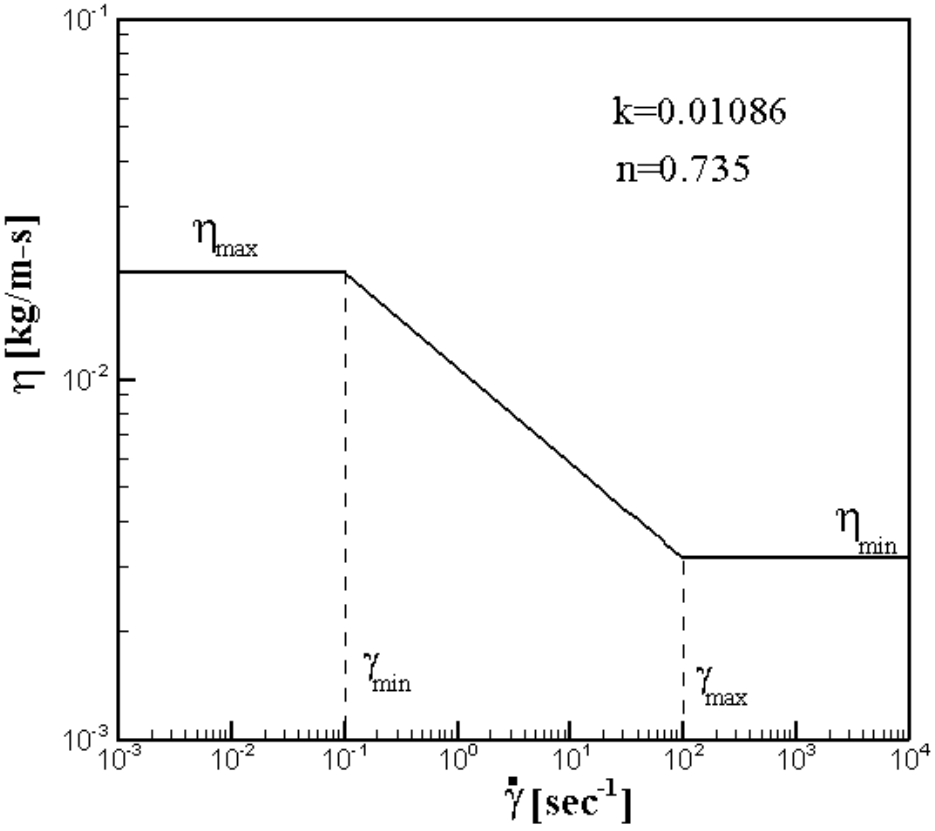

Figure 3.4 Variation of Viscosity with Rate of Strain According to the Non-Newtonian Power Law.

3.4.2. The Carreau Model

The Carreau model attempts to describe a wide range of fluids by the establishment of a curve-fit to piece together functions for both Newtonian and shear-thinning (n<1) non-Newtonian laws. In the Carreau model, the viscosity is

$$\eta = \eta_\infty + (\eta_0 - \eta_\infty)\left[1 + (\dot{\gamma}\lambda)^2\right]^{(n-1)/2}$$

where the parameters n, λ, η_0 and η_∞ are dependent upon the fluid. λ is the time constant, n is the power-law index, η_0 and η_∞ are, respectively, the zero and infinite shear viscosities. Figure 3.5 shows how viscosity is limited by η_0 and η_∞ at low and high shear rates. n can be varied to obtain the power-law region of the shear-thinning behavior. Relaxation time, λ, when increased while keeping all the other parameters constant shifts the power-law region to the right. Thus it dictates the shear-rates at which the power-law transition takes place. The power law index n governs the power-law regime in general. Table 3.2 shows the Carreau model parameters.

Table 3.2 Carreau model parameters

Parameters	List
η_∞ (kg/m-s)	0.0032
η_0 (kg/m-s)	0.05
λ(sec)	8.2
n	0.2128

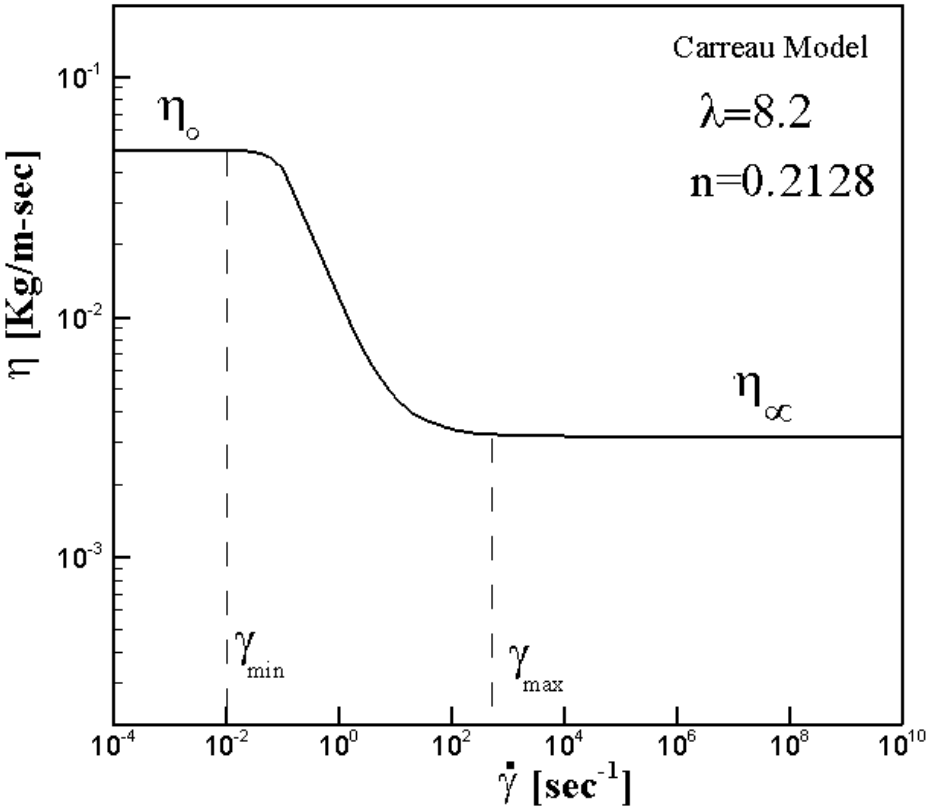

Figure 3.5 Variation of Viscosity with Rate of Strain According to the Carreau Model.

3.4.3. The Carreau-Yasuda Model

The Carreau-Yasuda model looks like:

$$\eta = \eta_\infty + (\eta_0 - \eta_\infty)\left[1 + (\dot{\gamma}\lambda)^a\right]^{(n-1)/a}$$

where $\dot{\gamma}$ is the shear rate, η_∞ is the shear rate viscosity at infinite shear rates, η_0 is the shear rate viscosity and λ is the relaxation time in seconds. Parameters a and n can be varied to obtain the power-law region of shear-thinning behavior. Relaxation time, λ, when increased while keeping all the other parameters constant shifts the power-law region to the right. Thus it dictates the shear-rates at which the power-law transition takes place. Parameter 'a' dictates the curvature at the top of the curve. A higher 'a' means a sharper transition of viscosity into the knowledge of these parameters become necessary while implementing a Carreau-Yasuda model into numerical simulations. Table 3.3 shows the Carreau-Yasuda model parameters. Figure 3.6 shows how viscosity is limited by η_0 and η_∞ at low and high shear rates.

Table 3.3 Carreau-Yasuda model parameters

Parameters	List
η_∞ (kg/m-s)	0.0032
η_0 (kg/m-s)	0.016
λ(sec)	8.2
n	0.2128
a	0.64

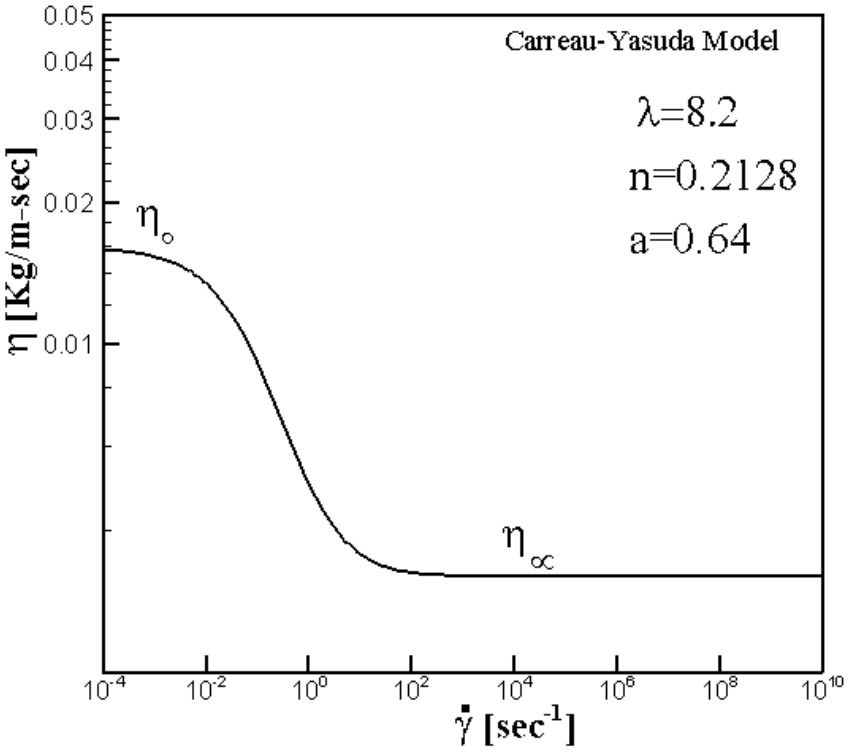

Figure 3.6 Variation of Viscosity with Rate of Strain According to the Carreau-Yasuda Model.

CHAPTER 4

NUMERICAL SOLUTION

4.1. Introduction

In the previous chapter the mathematical modeling of blood flow in axisymmetric tube to simulate the physics of the blood flow in arteries and veins is described. This modeling process results in partial differential equations that do not yield an analytical solution due to mathematical complexities involved and hence some other methods of solution are required. To solve these equations numerical methods can be employed, which are able to handle problems of any degree of complexity. A grid is drawn to cover the whole domain. With a sufficiently fine grid distribution, the complete distribution of the velocity can be expressed in terms of its values at neighboring grid points. Thus, the task of the numerical method is to evaluate velocity at each grid point. In a numerical scheme, a set of algebraic equations is derived from the governing differential equations for the grid-point values of the velocity. The accuracy of the obtained results depends mainly upon the proper selection of grid and time increments. But detail and accuracy somehow require computational effort (calculation time and computer memory).

Hence, in developing a numerical scheme, the primary consideration is a trade-off between the model detail and computational effort.

4.2. Numerical Method

Several techniques of numerical analysis exist. Among them most famous are finite difference, finite volume, finite element, spectral and pseudo-spectral methods. The finite volume technique is used in the present simulation for its simplicity and accuracy [69] Before proceeding to the finite volume method, it is appropriate to define basic properties of numerical solutions that determine their level of accuracy.

These properties include:

- Convergence
- Consistency
- Stability

Convergence is the property of a numerical method to produce a solution, which approaches the exact solution as the grid spacing; control volume size or element size is reduced to zero.

Consistency is the property of a numerical method to produce systems of algebraic equations, which can be demonstrated to be equivalent to the original governing partial differential equations as the grid spacing tends to zero.

Stability is associated with the growth or damping of errors as the numerical method proceeds and hence it describes whether or not the dependent variable is bounded. For transient analysis, the dependent variable is unstable if the solution oscillates with amplitude that increases with time. If a technique is not stable even round of errors in the initial data can cause wild oscillations or divergence.

Convergence is usually very difficult to establish theoretically and in practice Lax's Theorem is used, which states that for linear problems a necessary and sufficient condition for convergence is that the method is both consistent and stable. In CFD methods this theorem is of limited use since the governing equations are non-linear. In such problems consistency and stability are necessary conditions for convergence, but not sufficient.

The inability to prove conclusively that a numerical solution scheme is convergent is perhaps somewhat unsatisfying from a theoretical standpoint, but there is no need to be too concerned since the process of making the mesh spacing very close to zero is not feasible on computing machines with a finite representation of numbers. Round of errors would swamp the solution long before a grid spacing of zero is actually reached. In CFD, there is a need of codes that produce physically realistic results with good accuracy in simulations with finite (sometimes quite coarse) grids. Patankar [69] has formulated rules, which yield robust finite volume calculation schemes. The three crucial properties of robust methods include:

- Conservativeness

- Boundedness
- Transportiveness

Conservativeness is the property of a numerical scheme, which is associated with the consistent expressions for fluxes of the fluid property through the cell faces of adjacent control volumes.

Boundedness is akin to stability and requires that in a linear problem without sources the solution is bounded by the maximum and minimum boundary values of the flow variable. Boundedness can be achieved by placing restrictions on the magnitude and signs of the coefficients of the algebraic equations. Although flow problems are non-linear it is important to study the boundedness of a finite volume scheme for closely related but linear, problems.

Finally all flow processes contain effects due to convection and diffusion. In diffusive phenomena, such as heat conduction, a change of temperature at one location affects the temperature in more or less equal measure in all directions around it. Convective phenomena involve influencing exclusively in the flow direction so that a point only experiences effects due to changes at upstream locations. Transportiveness must account for the directionality of influencing in terms of the relative strength of diffusion to convection.

Conservativeness, boundedness and transportiveness are now commonly accepted as alternatives for the more mathematically rigorous concepts of convergence, consistency and stability [70].

4.3. Discretization

The discretization process is essentially an exercise of engineering judgment. The number, shape, size and configuration of the discrete volumes (control volumes) must be in such a way that the original body is simulated as close as possible. The general objective of such discretization is to divide the body into finite control volumes sufficiently small so that the simple models can adequately approximate the true solution. At the same time, one must remember that too fine a subdivision leads to extra computational effort.

For a given differential equation, the discretization equations can be derived in many ways as follows:

4.3.1. Taylor Series Formulation

The usual procedure for deriving finite-difference equations consists of approximating the derivatives in the differential equations via a truncated Taylor series. This is explained in detail by Lapidus and Pinder [68].

4.3.2. Finite Volume Formulation

This discretization technique is used in the present numerical calculations. In this discretization technique, the solution domain is divided into a number of non-overlapping control volumes such that there is one control volume surrounding each grid point. The differential equation is integrated over each control volume to yield the discretization equation. Thus, the discretization equation represents the same conservation principle over a finite region as the differential equation over an infinitesimal region. This direct interpretation of the discretization equation makes the method easy to understand in physical terms; the coefficients in the equation can be identified, even when they appear in a computer program, as familiar quantities such as flow rate, conductance, areas, volumes, diffusivities, etc. The control volume approach can be regarded as a special case of the method-weighted residuals Patankar [69] in which the weighted function is chosen to be unity over a control volume and zero everywhere else. Although the main reasons for choosing the control volume formulation are its simplicity and easy physical interpretation, the formulation has also been shown, for a limited set of test problems, to be more accurate than the Galerkin method Patankar [69] which is a more popular weighted residual technique.

4.4. Discritization of the Governing Transport Equation

The finite difference counterpart of the general partial differential equation is derived by supposing that each variable is enclosed in its own control volume and then by

integrating the partial differential equation over the control volume with some suitable assumption of field-variable profile within the finite volume.

For the purpose of solution the flow domain is overlaid with a number of grids whose center points or nodes denote the location at which all variables except velocities are calculated. The latter are computed at locations midway between the two pressure points. Thus the normal velocity components are directly available at the control volume faces, where they are needed for the scalar transport –convection-diffusion-computations. The nodes of a typical grid cluster for two dimensions are labeled a P, N, S, E, and W. This is show in Figure 4.1.

The integration of each term can be obtained with reference to the control volume for a typical node P with its four nearest neighbors, N,S, E, and W, in the spatial domain and P_0 in the time domain. The integration yields

$$\int_{t}^{t+\Delta t}\left\{\int_{CV}\left(\frac{\partial}{\partial t}(\rho\phi)-S_{\phi}\right)d\forall+\oint_{CS}[n.(\rho u_j\phi-\Gamma_{\phi}grad\phi)]dA\right\}dt=0 \tag{4.1}$$

where ρ is the density, u_j is the velocity vector, A is the surface area vector, Γ_{ϕ} is the diffusion coefficient for ϕ, S_{ϕ} is the source of ϕ per unit volume.

Divergence theorem gives

$$\int_{t}^{t+\Delta t}\left\{\int_{CV}\left(\frac{\partial}{\partial t}(\rho\phi)-S_{\phi}\right)d\forall+\oint_{CV}\left[\frac{\partial}{\partial x_j}\left(\rho u_j\phi-\Gamma_{\phi}\frac{\partial\phi}{\partial x_j}\right)\right]d\forall\right\}dt=0 \tag{4.2}$$

or

$$\int_{t}^{t+\Delta t}\left\{\left(\frac{\partial}{\partial t}(\rho\phi)-S_{\phi}\right)\Delta\forall+\left[\left(\rho u_j\phi-\Gamma_{\phi}\frac{\partial\phi}{\partial x_j}\right)\Delta A_j\right]_{L_1}^{L_2}\right\}dt=0 \tag{4.3}$$

or

$$\int_{t}^{t+\Delta t}\left\{\left(\frac{\partial}{\partial t}(\rho\phi)-S_{\phi}\right)\Delta\forall+\left[J_i\Delta A_j\right]_{L_1}^{L_2}\right\}dt=0 \tag{4.4}$$

Where L_1 denotes w or s, L_2 e or n and J_j the total flux (convection plus diffusion) across the face *'j'*.

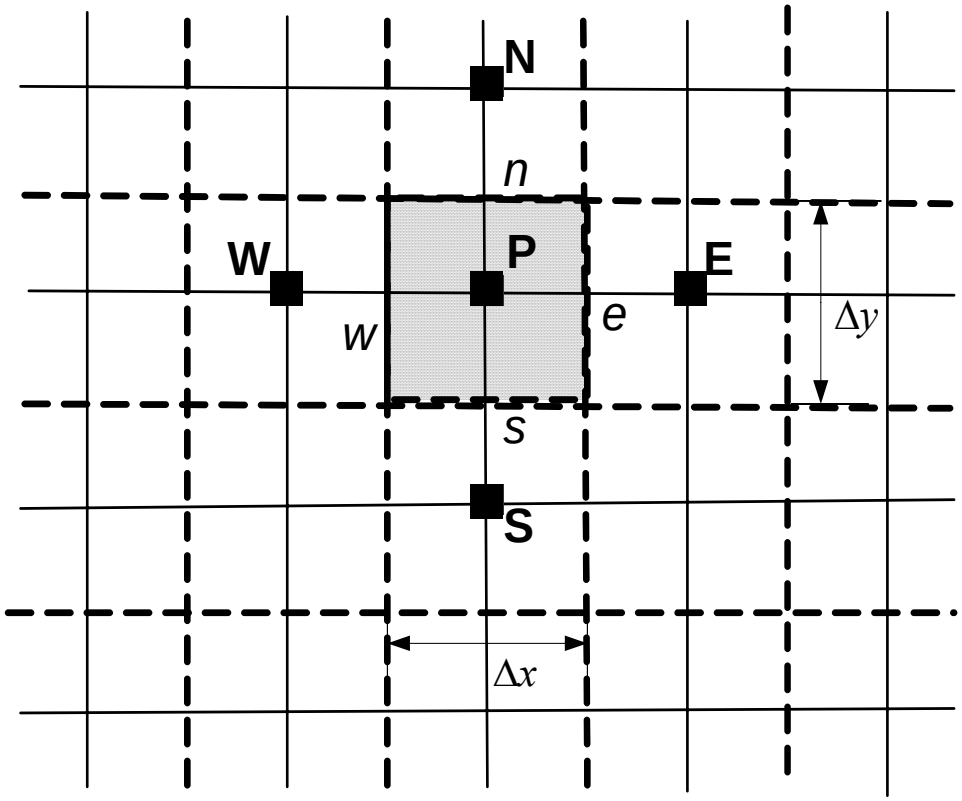

.

Figure 4.1 Control volume for the two-dimensional situation

If S_ϕ is independent of time then Eq. (4.4) becomes

$$\left[\frac{\rho_P\phi_P - \rho_P^0\phi_P^0}{\Delta t} - S_\phi\right]\Delta\forall + J_e - J_w + J_n - J_s = 0 \tag{4.5}$$

Where J_e, J_w, J_n and J_s are the integrated total fluxes over the control volume faces; i.e., J_e stands for $J_x\Delta A_x$ over the interface e, and so on. Where the superscript '0' is used for old values (i.e., the values at previous time step).

The linearization of the source term gives

$$S_\phi = S_0 + S_P\phi_P \tag{4.6}$$

Now Eq. (4.5) becomes

$$\left(\frac{\rho_P\phi_P - \rho_P^0\phi_P^0}{\Delta t}\right)\Delta\forall + J_e - J_w + J_n - J_s = \left(S_0 + S_P\phi_P\right)\Delta\forall \tag{4.7}$$

Now integration of the continuity equation in a similar manner to Eq. (3.24) gives

$$\int_t^{t+\Delta t}\left\{\int_{CV}\left[\frac{\partial\rho}{\partial t} + \frac{\partial}{\partial x_j}\left(\rho u_j\right)\right]d\forall\right\}dt = 0 \tag{4.8}$$

or

$$\int_{t}^{t+\Delta t}\left\{\frac{\partial \rho}{\partial t}\Delta\forall+\left[\rho u_j \Delta A_j\right]_{L_1}^{L_2}\right\}dt=0 \tag{4.9}$$

or

$$\int_{t}^{t+\Delta t}\left\{\frac{\partial \rho}{\partial t}\Delta\forall+\left[F_j \Delta A_j\right]_{L_1}^{L_2}\right\}dt=0 \tag{4.10}$$

or

$$\left(\frac{\rho_P-\rho_P^0}{\Delta t}\right)\Delta\forall+F_e-F_w+F_n-F_s=0 \tag{4.11}$$

Where F_j is the mass flux throught the face *'j'*, F_e, F_w, F_n, and F_s are the mass flow rates through the faces of the control volume; i.e. F_e stands for $F_x \Delta A_x$ over the interface e, and so on.

Multiplying Eq. (4.11) by ϕ_P, subtracting the resulting equation from Eq. (4.7) and knowing that;

$$J_e-F_e\phi_P=a_E(\phi_P-\phi_E) \tag{4.12}$$

$$J_w - F_w\phi_P = a_W(\phi_W - \phi_P) \tag{4.13}$$

$$J_n - F_n\phi_P = a_N(\phi_P - \phi_N) \tag{4.14}$$

$$J_s - F_s\phi_P = a_S(\phi_S - \phi_P) \tag{4.15}$$

One can develop the following algebraic equation [69].

$$a_P\phi_P = a_E\phi_E + a_W\phi_W + a_N\phi_N + a_S\phi_S + b) \tag{4.16}$$

Where

$$a_P = a_E + a_W + a_N + a_S + a_P^0 - s_P\Delta\forall \tag{4.17}$$

$$a_P^0 = \frac{\rho_P^0\Delta\forall}{\Delta t} \tag{4.18}$$

$$b = a_P^0\phi_P^0 + S_0\Delta\nabla \tag{4.19}$$

$$a_E = D_E A\left(\left|P_E\right|\right) + \left|\left|-F_E, 0\right|\right| \tag{4.20}$$

$$a_W = D_W A(|P_W|) + [|F_W, 0|] \tag{4.21}$$

$$a_N = D_N A(|P_N|) + [|-F_N, 0|] \tag{4.22}$$

$$a_S = D_S A(|P_S|) + [|F_S, 0|] \tag{4.23}$$

And P_e, P_w, P_n, and P_s are the Peclet numbers: i.e. P_e stands for $\frac{F_e}{D_e}$ and so on; D_e, D_w, D_n, and D_s are the diffusion conductances; i.e., D_e stands for $\frac{\Gamma_e \Delta y}{(\delta x_e)}$ and so on. The values of $A(|P|)$ are given in [69] for different schemes. In the present study, second order upwind scheme is employed.

Equation (4.16) is written for each of the variables, u, v, ρ and T at every cell. Although the control volumes adjacent to the boundary treated differently from the interior ones and need different algebraic formulation, it is possible to have a unified formulation to calculate the field variable in the near boundary region through the use of source term [70].

4.4.1. First-Order Upwind Scheme

In the first-order upwind scheme, quantities at cell faces are determined by assuming that the cell-center values of any field variable represent a cell-average value and hold throughout the entire cell; the face quantities are identical to the cell quantities. Thus in first-order upwinding, the face value ϕ_f is set equal to the cell-center value of ϕ in the upstream cell.

4.4.2. Second-Order Upwind Scheme

In second-order upwind scheme, quantities at cell faces are computed using a multidimensional linear reconstruction approach Barth and Jespersen [71]. In this approach, higher-order accuracy is achieved at cell faces through a Taylor series expansion of the cell-centered solution about the cell centroid. Thus, when second-order up-winding is selected, the face value ϕ_f is computed using the following expression:

$$\phi_f = \phi + \nabla\phi \cdot \Delta s \tag{4.24}$$

where ϕ and $\nabla\phi$ are the cell-centered value and its gradient in the upstream cell, and Δs is the displacement vector from the upstream cell centroid to the face centroid. This formulation requires the determination of the gradient $\nabla\phi$ in each cell. This is computed using the divergence theorem, which in discrete form can be written as

$$\nabla\phi = \frac{1}{V}\sum_{f}^{N_{faces}} \tilde{\phi}_f A \tag{4.25}$$

Here the face values $\tilde{\phi}_f$ are computed by averaging ϕ from the two cells adjacent to the face. Finally, the gradient $\nabla\phi$ is limited so that no new maxima or minima are introduced.

4.5. Computation of the Flow Field

The solution of the general transport equation (3.46) presents two new problems:

- The convective term of Eq. (3.46) contains non-linear inertia terms.
- The continuity, momentum, energy, species and turbulence equations, represented by Eq. (3.46), are intricately coupled because every velocity component appearing in each equation. The most complex issue to resolve is the role played by pressure. It appears in the momentum equations, but there is evidently no transport equation for pressure.

4.5.1. Solution Algorithms for Pressure-Velocity Coupling

If the pressure field, which appears as a major part of the source term, is unknown then equation (4.16) applied at all the nodal points yields a set of algebraic equations but the resulting velocity field may not satisfy the continuity equation. The problems of determining the pressure and satisfying continuity are overcome by adjusting the pressure field using pressure-velocity coupling. In the present study the SIMPLE algorithm

Patankar and Spalding [72] is used for the pressure-velocity coupling. The acronym SIMPLE stands for Semi-Implicit Method for Pressure-Linked Equations. In this algorithm, the pressure field p^* is first assumed. The discretized momentum equations are then solved using the assumed pressure field to yield velocity components u^* and v^*. Now the correction, p', defined as the difference between the correct pressure field p and the assumed pressure field p^*, is calculated and a better approximation of the pressure field can be obtained using $p = p^* + p'$. Similarly, the velocity components are corrected by adding the increments u' and v' to the assumed velocity components u^* and v^*. The whole process of the SIMPLE algorithm is explained in the flow diagram given in Figure 4.1.

4.5.2. Convergence Criterion

The use of an iterative solution method necessitates the definition of a convergence and stopping criteria to terminate the iteration process. The measure of convergence is a norm on the change in the solution vector between successive iterations. The iterative algorithm is terminated after a fixed number of iterations if the convergence has not been achieved. This criteria is used to prevent slowly convergent or divergent problems from wasting computation time. Convergence in this present study is defined to have been obtained after all the following criteria are achieved.

Changes in the x - and y - velocity component are less than 1×10^{-6}

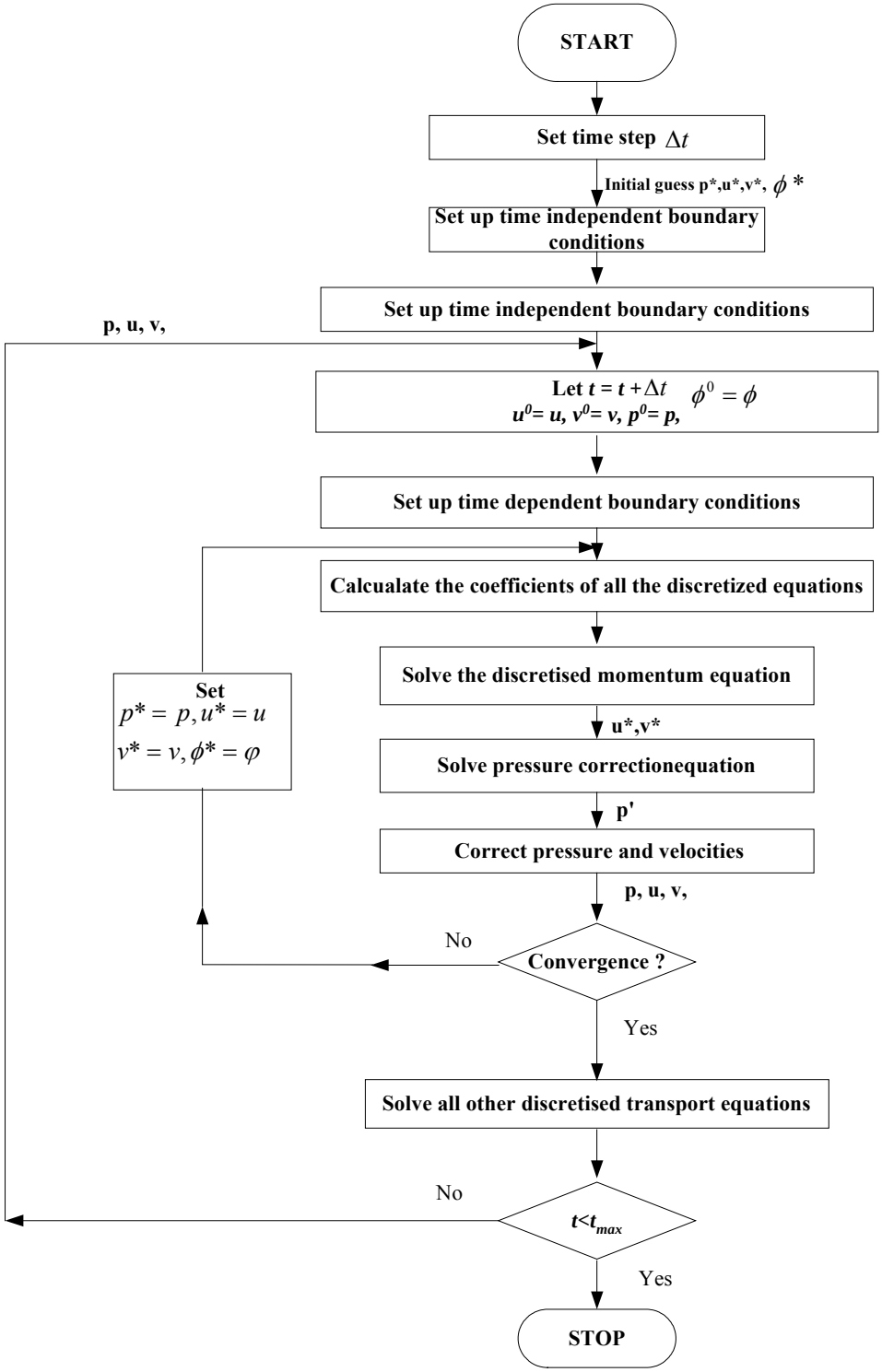

Figure 4.2 The SIMPLE Algorithm.

4.6. Dynamic Mesh Model

The dynamic mesh model in FLUENT [73] can be used to model flows where the shape of the domain is changing with time due to motion on the domain boundaries. The motion can be a prescribed motion (e.g., you can specify the linear and angular velocities about the center of gravity of a solid body with time) or an unprescribed motion where the subsequent motion is determined based on the solution at the current time (e.g., the linear and angular velocities are calculated from the force balance on a solid body). The update of the volume mesh is handled automatically at each time step based on the new positions of the boundaries. To use the dynamic mesh model, you need to provide a starting volume mesh and the description of the motion of any moving zones in the model. FLUENT allows you to describe the motion using either boundary profiles or user-defined functions (UDFs). For the present study, the motion of the moving indented wall was described by means of a User-defined functions (UDF).

4.6.1. Dynamic Mesh Conservation Equations

The integral form of the conservation equation for a general scalar, ϕ, on an arbitrary control volume, V, whose boundary is moving can be written as

$$\frac{\partial}{\partial t}\int_{CV}\rho\phi dV + \int_{\partial V}\rho\phi(u-u_g).dA = \int_{\partial V}\Gamma\nabla\phi.dA + \int_{V}S_\phi.dV \tag{4.26}$$

Where ρ is the fluid density, u is the flow velocity vector, u_g is the grid velocity of the moving mesh, Γ is the diffusion coefficient and S_ϕ is the source term of ϕ. Here ∂V is used to represent the boundary of the control volume V.

The time derivative term in Eq. 4.26 can be written, using a first-order backward difference formula, as

$$\frac{\partial}{\partial t}\int_{CV}\rho\phi dV = \frac{(\rho\phi V)^{n+1} - (\rho\phi V)^{n}}{\Delta t} \tag{4.27}$$

where n and n+1denote the respective quantity at the current and next time level. The *(n+1)* th time level volume V is computed from

$$V^{n+1} = V^{n} + \frac{dV}{dt}\Delta t \tag{4.28}$$

where dV/dt is the volume time derivative of the control volume. In order to satisfy the grid conservation law, the volume time derivative of the control volume is computed from

$$\frac{dV}{dt} = \int_{\partial V} u_g . dA = \sum_{j}^{n_j} u_{gj} . A_j \tag{4.29}$$

Where n_f is the number of faces on the control volume and A_j is the j face area vector. The dot product $u_{gi}.A_j$ on each control volume face is calculated from

$$u_{gj}.A_j = \frac{\delta V_j}{\Delta t} \tag{4.30}$$

Where δV_j is the volume swept out by the control volume face j over the time step Δ t.

4.6.2. Dynamic Mesh Update Methods

Three mesh motion methods are available in FLUENT to update the volume mesh in the deforming regions subject to the motion defined at the boundaries:

- Spring-based Smoothing
- Dynamic Layering
- Local Remeshing

4.6.2.1. Spring-Based Smoothing

In the spring-based smoothing method, the edges between any two mesh nodes are idealized as a network of interconnected springs. The initial spacing of the edges before any boundary motion constitutes the equilibrium state of the mesh. A displacement at a given boundary node will generate a force proportional to the displacement along all the springs connected to the node. Using Hook's Law, the force on a mesh node can be written as

$$F_i = \sum_j^{n_i} k_{ij}(\Delta x_j - \Delta x_i) \tag{4.31}$$

Where $=\Delta x_i$ and Δx_j are the displacements of node i and its neighbor j, n_i is the number of neighboring nodes connected to node i, and k_{ij} is the spring constant (or stiffness) between node i between node i and its neighbor j. The spring constant for the edge connecting nodes i and j is defined as

$$k_{ij} = \frac{1}{\sqrt{\left|(\Delta x_j - \Delta x_i)\right|}} \tag{4.32}$$

At equilibrium, the net force on a node due to all the springs connected to the node must be zero. This condition results in an iterative equation such that

$$\Delta x_i^{m+1} = \frac{\sum_j^{n_i} k_{ij} \Delta x_j^m}{\sum_j^{n_i} k_{ij}} \tag{4.32}$$

Since displacements are known at the boundaries (after boundary node positions have been updated), Eq. 4.32 is solved using a Jacobi sweep on all interior nodes. At convergence, the positions are updated such that

$$\Delta x_i^{n+1} = x_i + \Delta x_i^{m,converged} \tag{4.33}$$

Where *n+1* and *n* are used to denote the positions at the next time step and the current time step, respectively.

4.6.3. Dynamic Layering

In prismatic (hexahedral and/or wedge) mesh zones, you can use dynamic layering to add or remove layers of cells adjacent to a moving boundary, based on the height of the layer adjacent to the moving surface. The dynamic mesh model allows you to specify an ideal layer height on each moving boundary. The layer of cells adjacent to the moving boundary is split or merged with the layer of cells next to it based on the height (*h*) of the cells in layer.

4.6.4. Local Remeshing Method

On zones with a triangular or tetrahedral mesh, the spring-based smoothing method is normally used. When the boundary displacement is large compared to the local cell sizes, the cell quality can deteriorate or the cells can become degenerate. This will invalidate the mesh (e.g., result in negative cell volumes) and consequently, will lead to convergence problems when the solution is updated to the next time step.

To circumvent this problem, FLUENT agglomerates cells that violate the skewness or size criteria and locally remeshes the agglomerated cells. If the new cells satisfy the skewness and the size criteria, the mesh is locally updated with the new cells (with the solution interpolated from the old cells). Otherwise, the new cells are discarded.

For the current simulations spring based smoothing method is used with the following parameters:

Table 4.1 Spring-based smoothing- mesh update parameters

Parameters	Values
Spring Constant factor	0.02
Boundary Node Relaxation	0.7
Convergence Tolerance	0.0001
Number of Iterations	50

CHAPTER 5

RESULTS AND DISCUSSIONS

Based on the cited literature, it can be concluded that no work was published on the subject of flow in an axisymmetric tube with a moving indentation, which closely resembles the flow in arteries and veins. In the present study, a two dimensional numerical model is used to simulate the time-dependent flow in a wall deforming channels. The model is first used to simulate the flow in a 2D channel with a moving indentation for validation [14] purposes. Secondly, the model is extended to simulate the flow in an axisymmetric tube with an indentation moving at a given frequency.

5.1. Two-Dimensional Channel Flow With a Moving Indentation (Newtonian Fluid) - Validation

For the validation of the present computational method, the computational results of some selected cases were compared with the experimental results of Pedley and Stephanoff [14] and the numerical results of Ralph and Pedley [43]. However, the comparison of the prediction with the results of the above-mentioned experiment and

numerical will be made after a brief look on the experimental set-up and the conditions involved in the experiment

Figure 5.1 shows a sketch of the experimental system used by Pedley [14]. The closed channel is 2.5 m long, 10 mm wide and 100 mm deep; it has rigid walls except for the indentation in one vertical wall. The narrower, horizontal walls are made of Perspex, and there are Perspex windows (of length 100mm and 180mm) in the vertical wall oppsite the indentation. The indentation consists of a thick rubber membrane, which begins 1.2 m from the channel inlet, is 165 mm long and over 100 mm deep. It is moulded round an (almost) square piston, 100x100 mm, that can move in and out (see figure). Ideally, when the piston is fully retracted the membrane is flush with the rest of the plane wall; however slight ridges (<0.4 mm) were observed where the membrane passed over the ends of the retracted piston.

The piston was driven sinusoidally, and its amplitude and period were adjustable. During the first half of the cycle the piston pushes the membrane into the channel from the flush position. During the second half of the cycle, when the piston is being retracted, the pressure of the water in the channel holds the membrane against the piston and prevents the two sloping parts of the membrane from bulging into the channel. The displacement of the piston from its retracted position was measured with a RM 700 strain-gauge displacement transducer; the motion of the piston was compared on an oscilloscope screen with sine waves from a waveform generator, and was found to be sinusoidal. A Flostat type-V control valve upstream of the channel kept the flow rate of the water

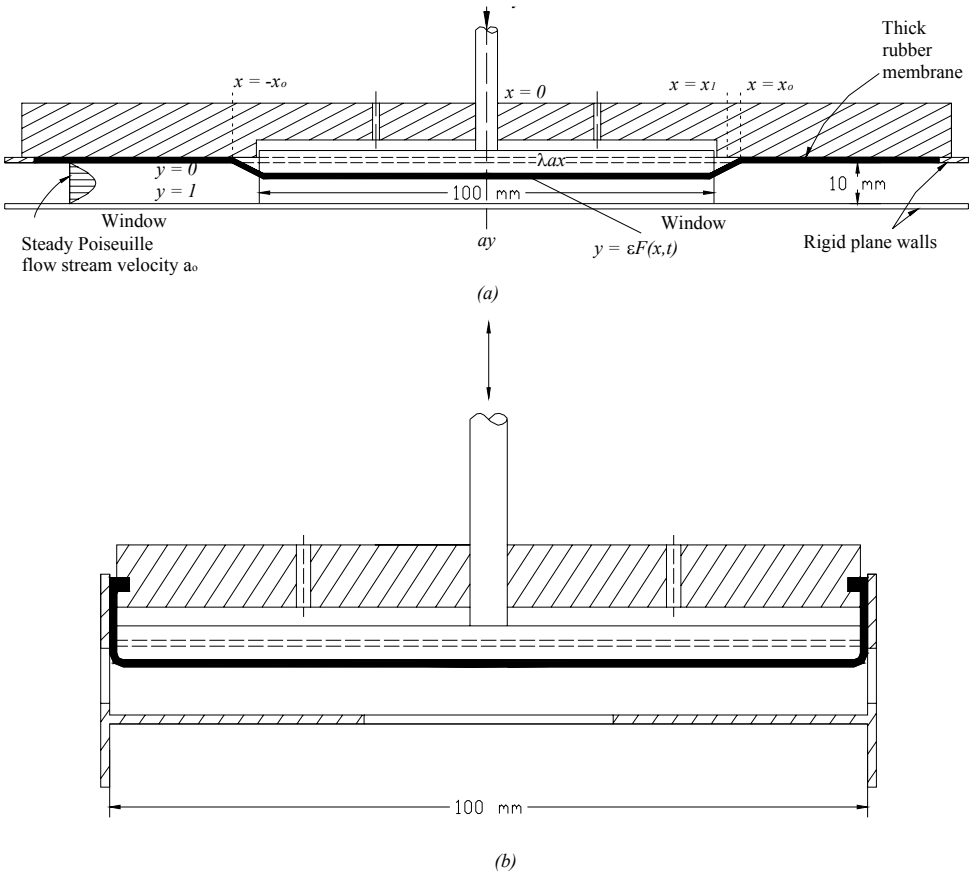

Figure 5.1 (a) Sketch of the horizontal channel midplane, showing the section with the moving indentation in one wall, and windows in the opposite wall. (b) Sketch of the cross section of the channel, showing the membrane wrapped around the piston at the top and bottom.

entering the channel steady, so that the variations of flow rate caused by the piston motion were confined to the downstream segment of the channel. Capturing the images of the resulting flow filed using the photographs, the locations of few wave crests as functions of time were plotted.

5.1.1. Grid independence test

A number of grid independence tests were carried out in the present study. Three meshes with different sizes were tested: Mesh 1 with 24,400 (610 X 40) cells; Mesh 2 with 33,975 (755 X 45) cells and Mesh 3 with 39,600 (880 X 45) cells. A section of the fine grid (Mesh 2) is shown in Figure 5.2 for the time instants $\tau = 0$ and $\tau = 0.5$. The grid is refined downstream of the indentation where the flow is affected by its movement. Figure 5.3(a) and Figure 5.3(b) show the comparison of the longitudinal velocity calculated on different grids at X=5.5 R for $\tau = 0.5$ and $\tau = 0.75$ (both obtained with $\delta t = t_0 / 1000$) respectively. Figure 5.4 (a) and Figure 5.4 (b) show the comparison of the wall shear stress calculated on different grids at $\tau = 0.5$ and $\tau = 0.75$ (both obtained with $\delta t = t_0 / 1000$) respectively. These comparisons show that there is no significant difference in the longitudinal velocity and the wall shear stress observed between the meshes with 33,975 (755 X 45) cells and 39,600 (880 X 45) cells. Hence the finer Mesh 2 is adopted.

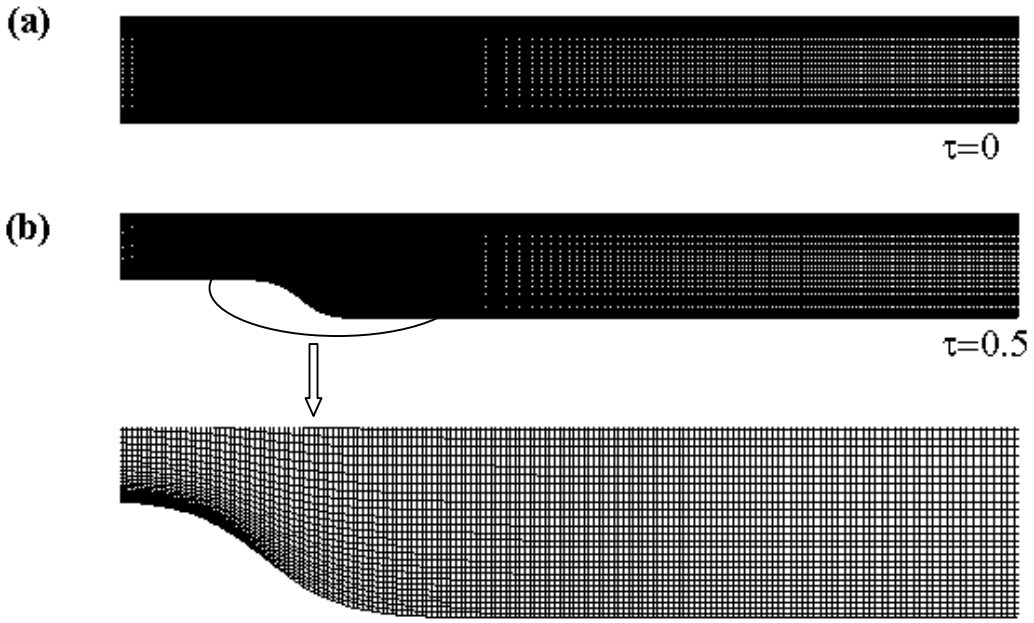

Figure 5.2 Section of the 2-D channel grid with 33,975 (755 X 45) cells at (a) $\tau = 0$ and (b) $\tau = 0.5$ b=1cm, Q_0=0.0306 m^3/min (30,600 ml/min), t_0=5.3 sec.

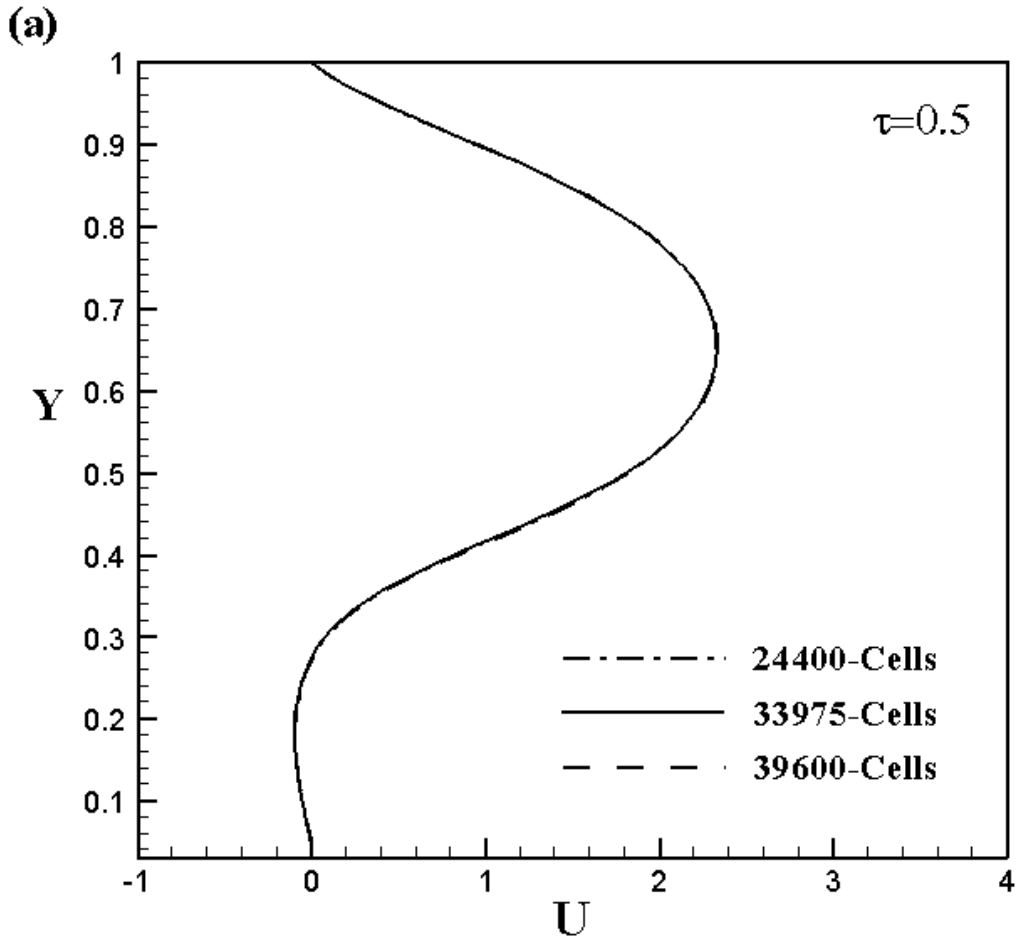

Figure 5.3 (a) Comparison of longitudinal velocity on three grids at τ=0.5 using time step $\delta t = t_0 / 1000$ for 2D-channel.

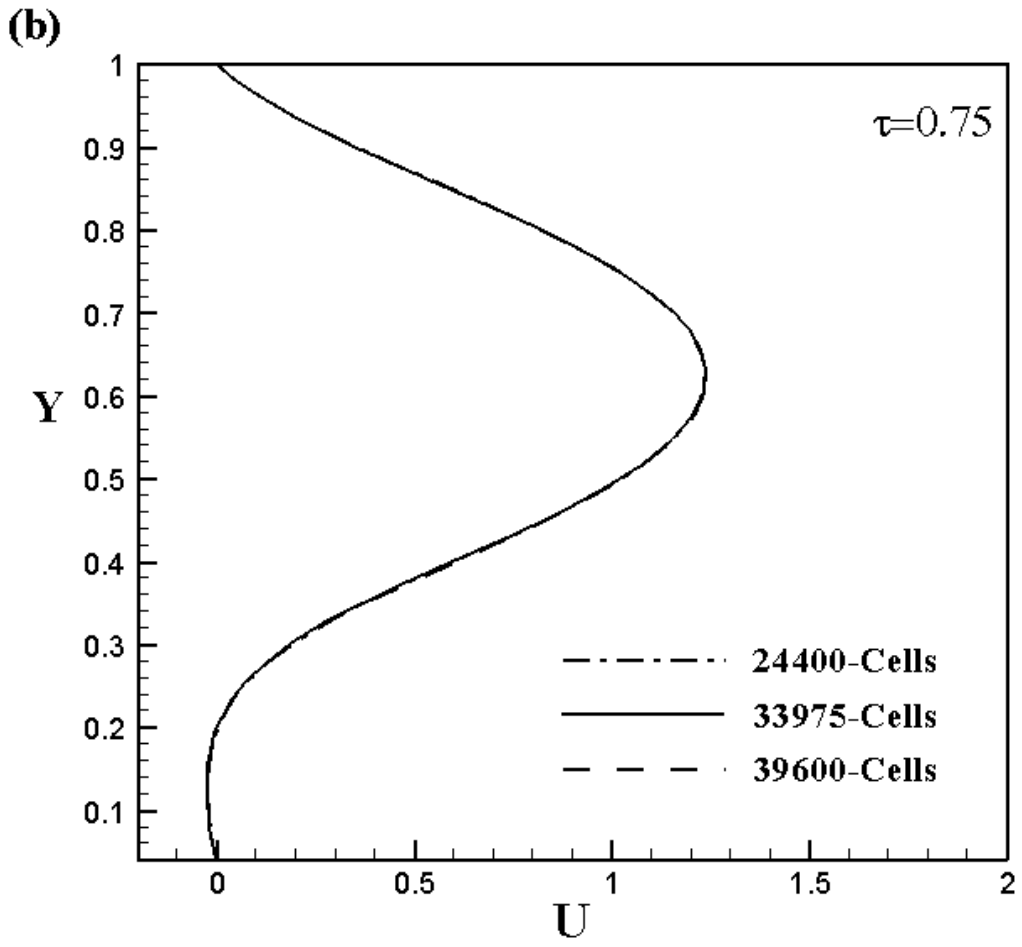

Figure 5.3(b) Comparison of longitudinal velocity on three grids at τ=0.75 using time step $\delta t = t_0 / 1000$ for 2D-channel.

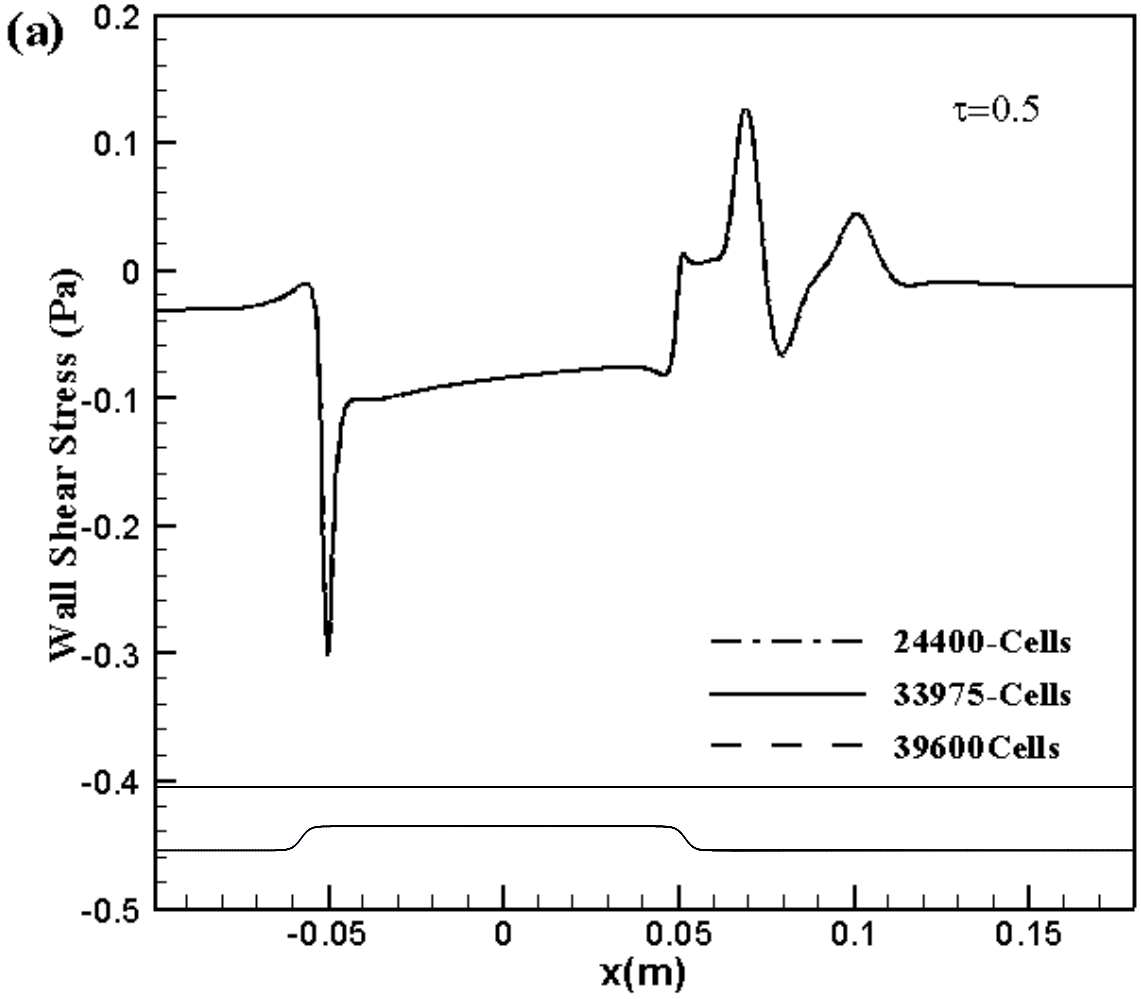

Figure 5.4 (a) Comparison of predicted wall shear stress on three grids at τ=0.5using time step $\delta t = t_0 / 1000$ for a 2D Planar channel.

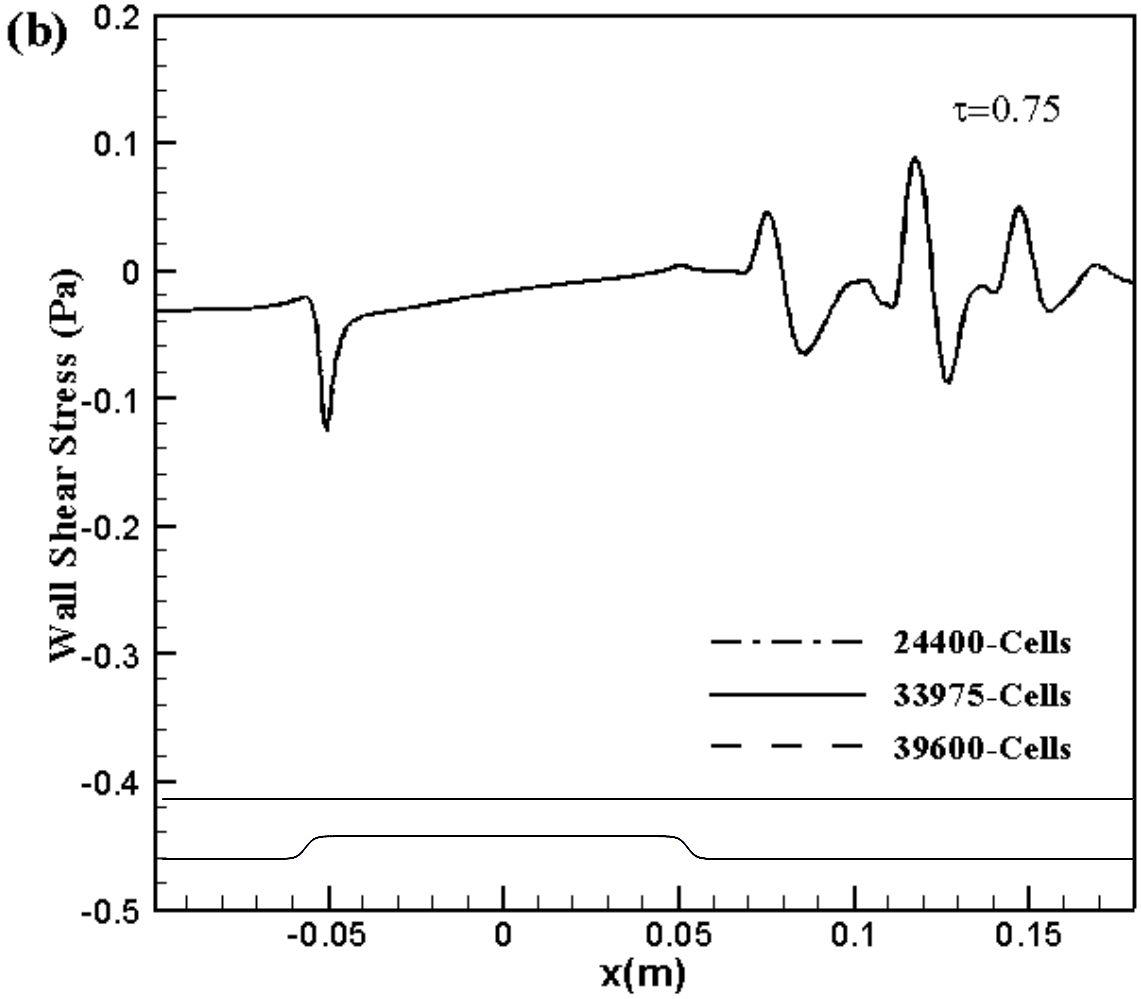

Figure 5.4 (b) Comparison of predicted wall shear stress on three grids at τ=0.75 using time step $\delta t = t_0 / 1000$ for a 2D Planar channel.

5.1.2. Flow Development

The volume flow rate Q_0 upstream of the moving indentation is taken to be fixed which is close to reality. For Re=507, Q_0=0.0306 m^3/min (30,600 ml/min). Figure 5.5 (ii)(a-l) shows the predicted velocity streamlines at τ=0.1 to 1 respectively. Only the section downstream the indentation is shown since the flow upstream is not affected much by its movement. The flow development is found to be the same as that of Pedley [14, 44] and a brief summary is presented here. A train of vorticity waves is generated downstream of the indentation every cycle. At some time between $\tau = 0.2$ and $\tau = 0.25$, separation occurs in the lee of the indentation, and the resulting eddy grows rapidly. A second eddy of opposite sign forms on the upper wall at some distance downstream of the first and a third appears still further downstream on the lower wall and so on until there is a sequence of such eddies of alternating sign, bounded by a wavy core flow.

At time τ=0.6, Figure 5.5 (i)g shows five eddies marked A, B, C, D and E. As time increases not only the number of eddies increases but also the subsequent extent of existing eddies and the amplitude of the core waviness also increases. As the indentation recedes late in the cycle, the eddies shrink in size and strength and are swept downstream of the indentation, but at τ=1, there is again vorticity of uniform sign at each wall Figure 5.5 (ii) shows the instantaneous streamlines obtained by the Pedley at different instants. It can be observed that a qualitative agreement exists between the present numerical results and Ralph and Pedley's [14, 44].

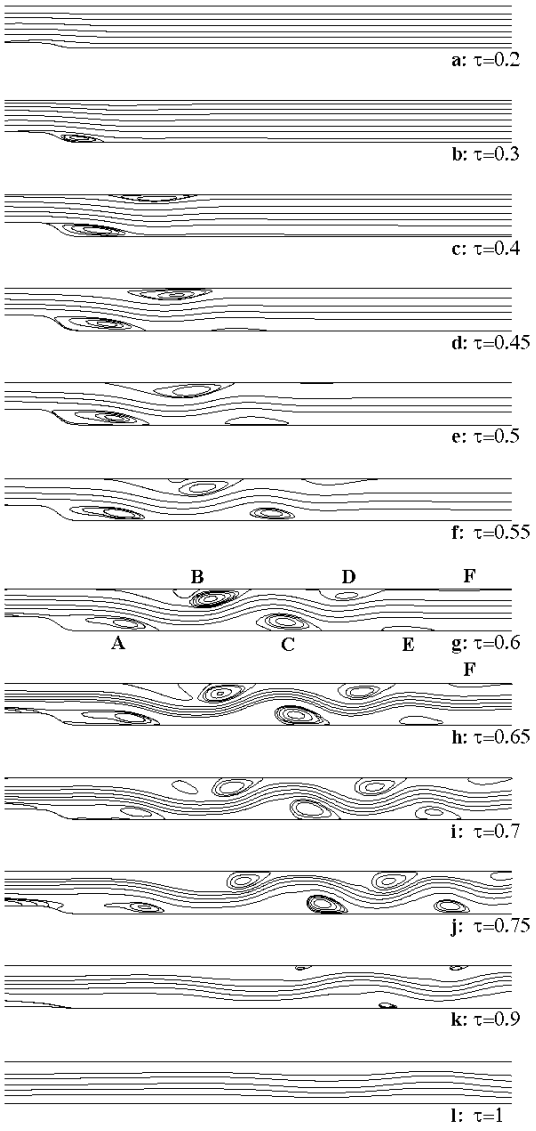

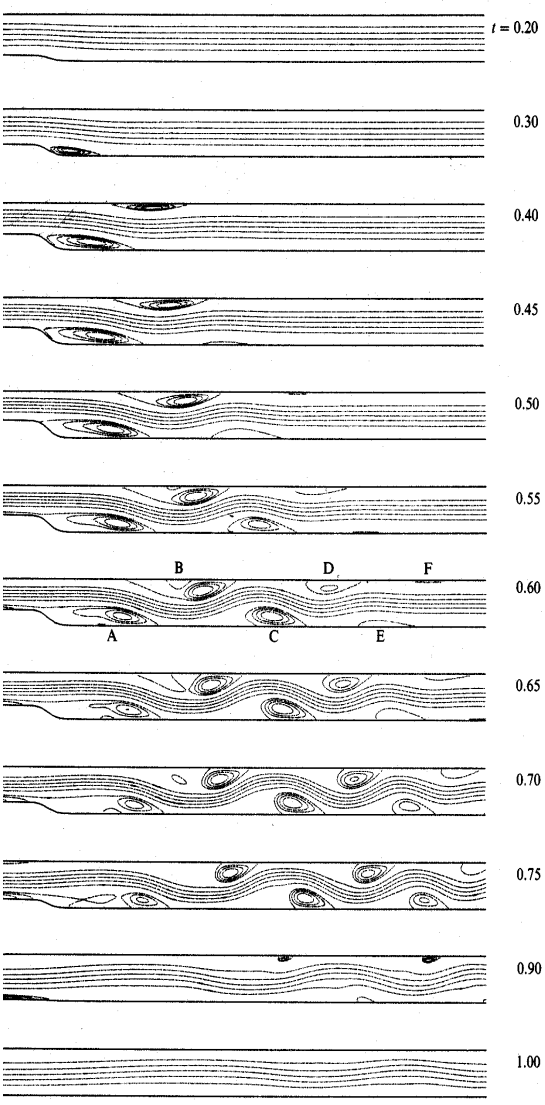

(i) Present Case (ii) Ralph and Pedley [43]

Figure 5.5 Predicted velocity streamlines downstream of the indentation at various times (τ) for a 2D-Planar channel.

Figure 5.6(a), (b), (c) and (d) show the longitudinal velocity profiles at different cross sections of the channel at various time intervals. The velocity profiles are parabolic throughout the cycle at the inlet. As the indentation grows, the profiles become distorted due to the upward movement of the indentation. Separation occurs at the sections where both positive and negative velocity vectors exist. When the indentation moves back, the profiles tend to go back to their original shapes. This trend ultimately creates a wavy core flow along the channel.

Figure 5.7 (a), (b) and Figure 5.8 (a), (b) show the variation of the wall shear stress on the lower (indented) and upper (unindented) wall respectively at various time intervals during the cycle. The wall shear stress is calculated using the following formula,

$$\tau_w = -\mu\left(\frac{\partial u}{\partial y} + \frac{\partial v}{\partial x}\right)$$

where μ is the viscosity, u is the velocity in x-direction and v is the velocity in y-direction. Negative sign is taken to compare the present results with the published results in the literature. They indicate the strength of the eddies, the positions of separation and reattachment (change of sign in wall shear stress) and thus the movement of eddies along the wall. The first four eddies marked A, B, C and D in Figure 5.5 i(f), are the strongest; eddies E and F are relatively weak. Eddy A (marked in Figure 5.5 i(f) is strongest at τ=0.5 (maximum shear stress occurs then); peaks in other eddies occur $0.05t_0$ later, in the order of their appearance. The shear stress variation along the indentation and the opposite wall also indicates an acceleration of the flow in this region when the indentation is moving

inwards ($\tau<0.5$) and a deceleration when it is retracting ($\tau>0.5$). Figure 5.7 and Figure 5.8 also show that the steadiness of the flow upstream of the indentations is hardly affected by the indentation motion.

A quantitative comparison between the present results and the experimental result [14] and the numerical result [43] is shown graphically in Figure 5.9. This comparison is shown as the time evaluation of the positions of crests/troughs of the wave after the indentation. Wave-crest positions as functions of time are obtained from the turning points in the axial direction of stream function at the centre of the channel. According to the Pedley and Stephanoff, the abscissa is defined as

$$x^* = (x - x_1)(10St)^{1/3} / b$$

It can be observed from the figure, that there is a good agreement between the present numerical result and experimental result, with discrepancies within the range of the experimental scatter.

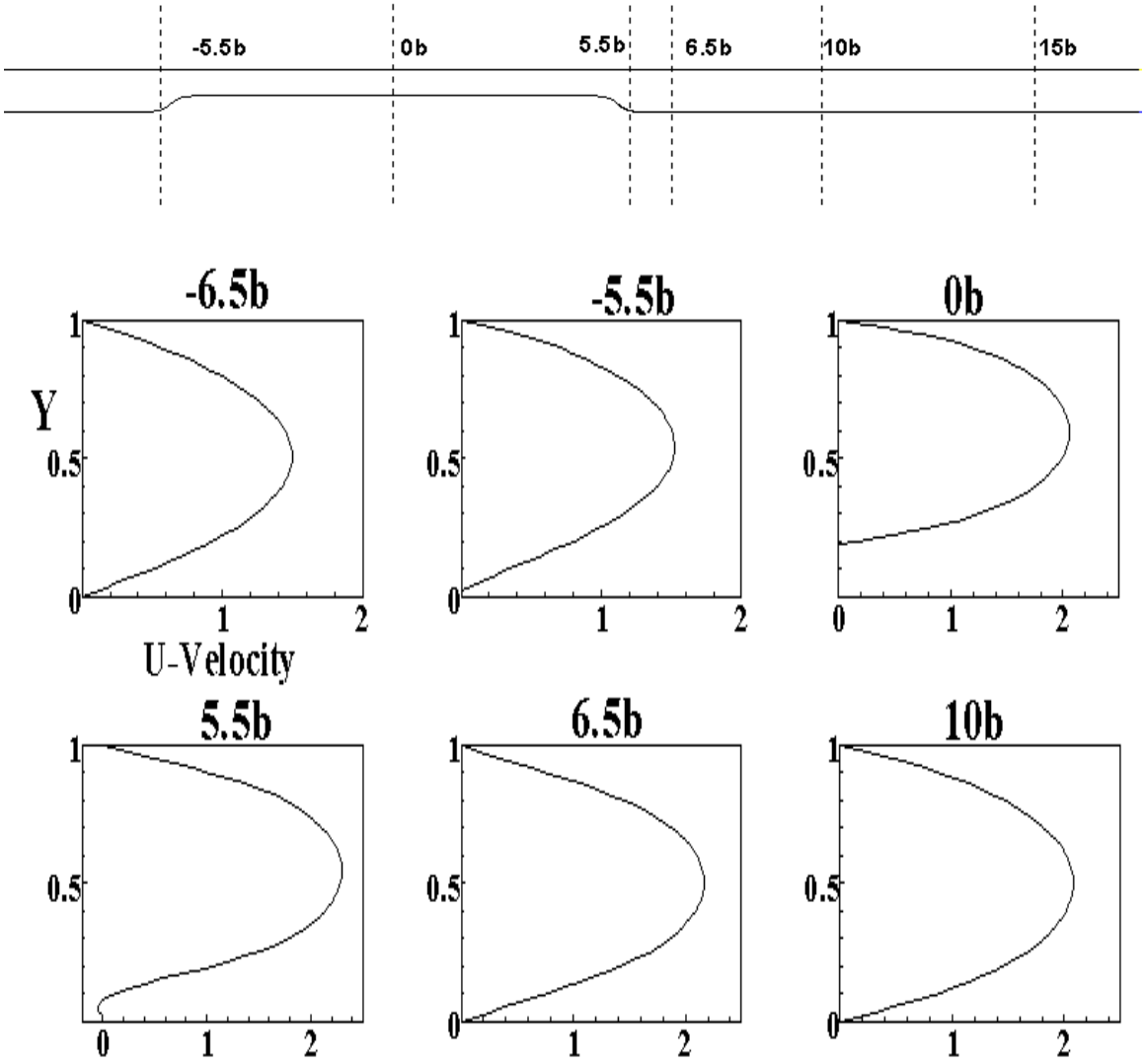

Figure 5.6(a) Velocity Profiles at different cross sections at τ=0.25, for a 2D-Planar channel.

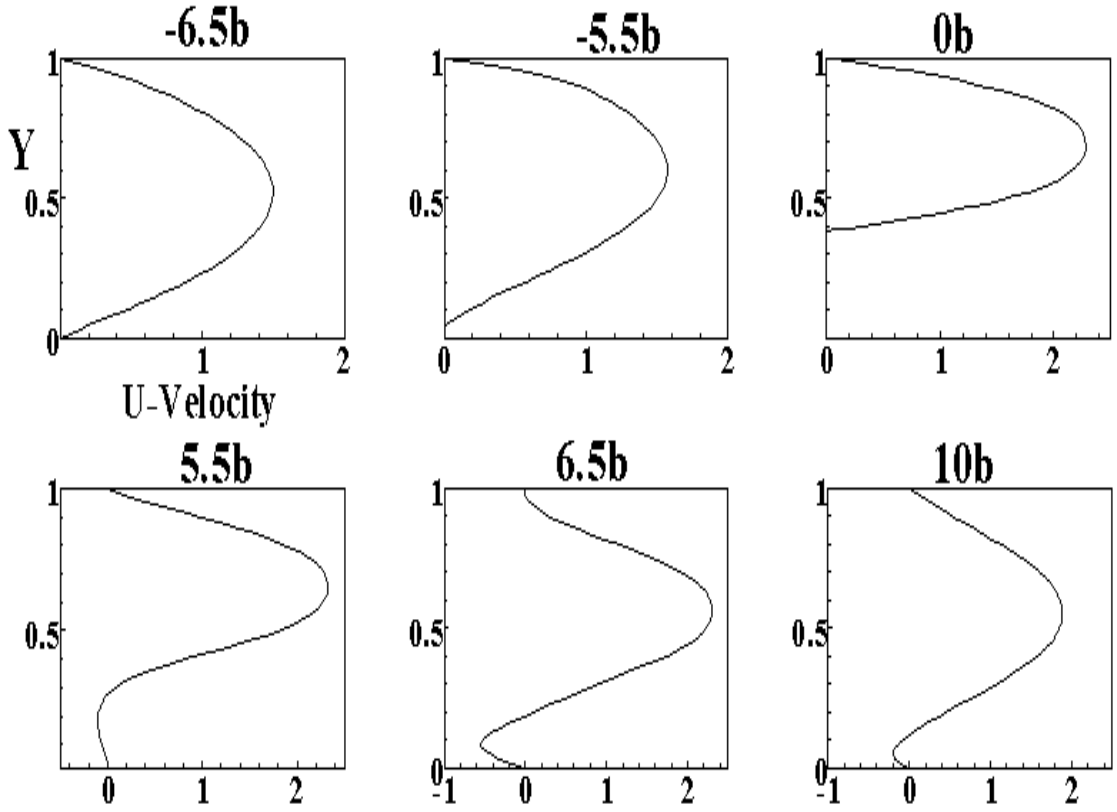

Figure 5.6(b) Velocity Profiles at different cross sections at τ=0.5, for a 2D-Planar channel.

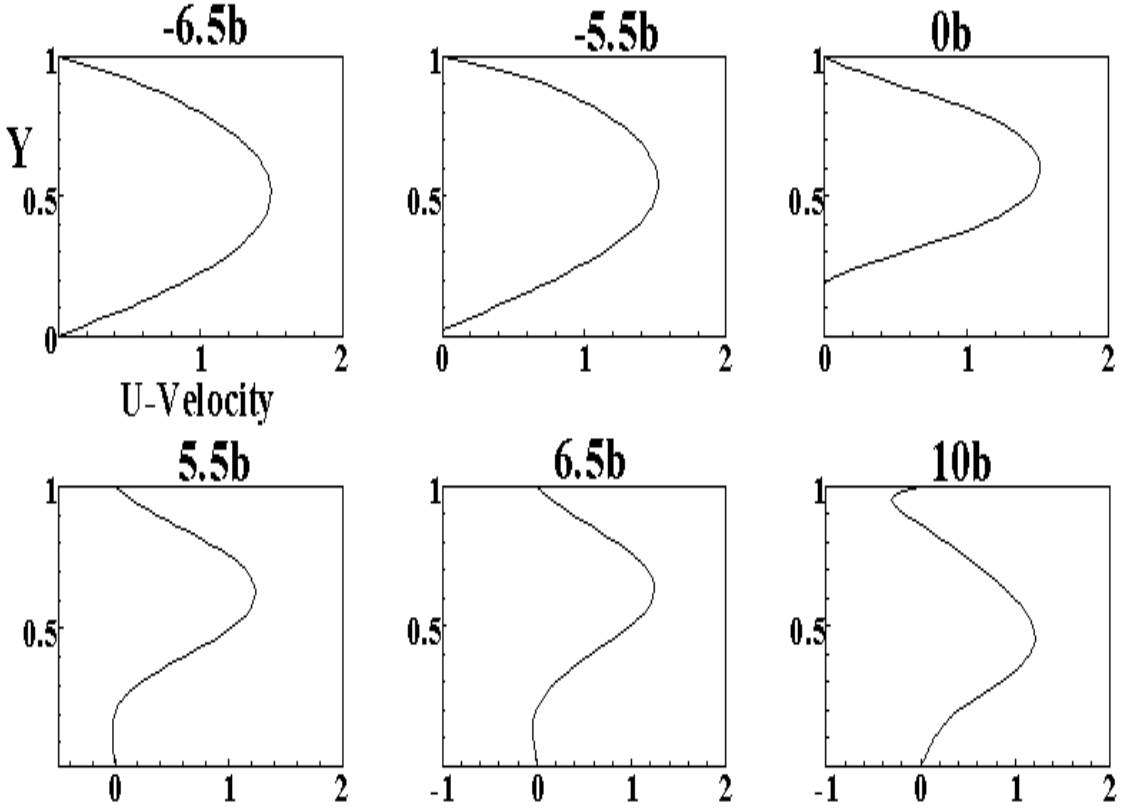

Figure 5.6(c) Velocity Profiles at different cross sections at τ=0.75, for a 2D-Planar channel.

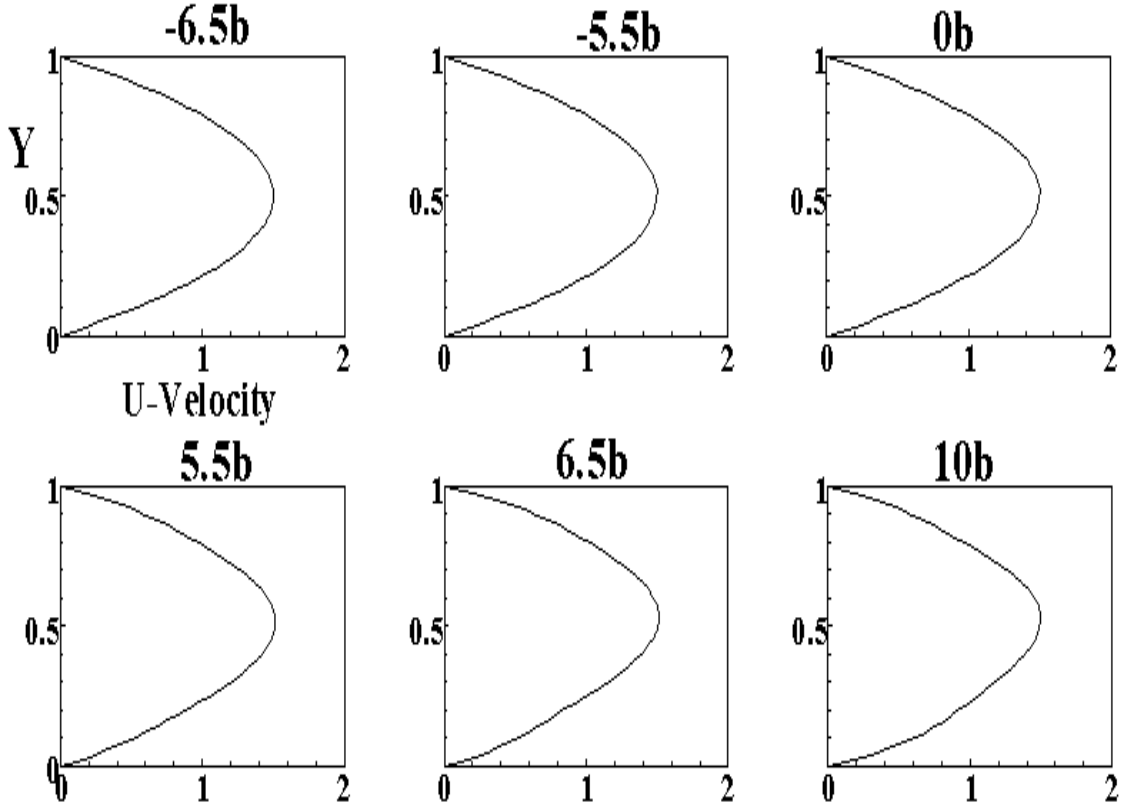

(d) τ=1

Figure 5.6(d) Velocity Profiles at different cross sections at τ=1, for a 2D-Planar channel.

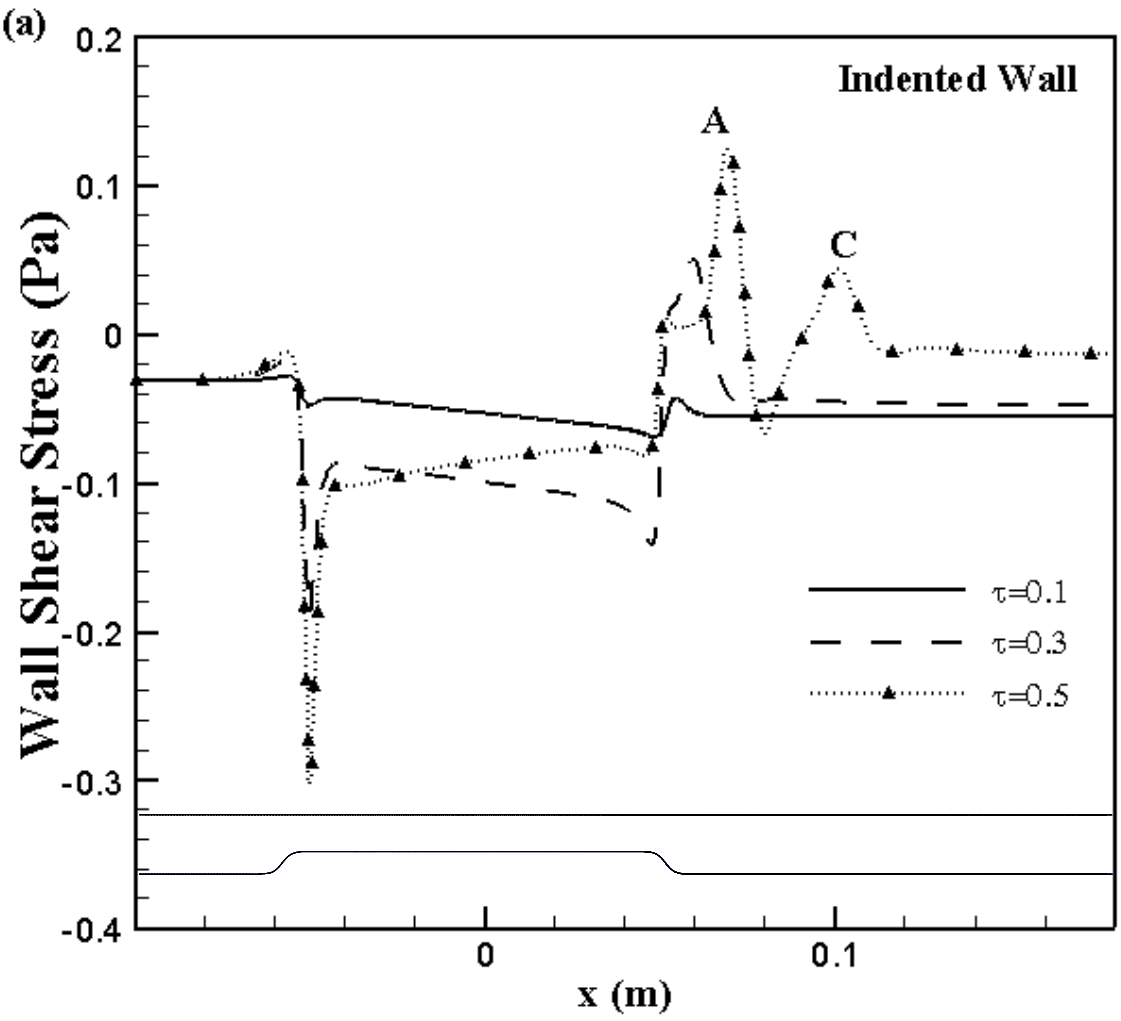

Figure 5.7 (a) Predicted wall shear stress variations during one cycle along the indented wall, τ=0.1 to 0.5, for a 2D-Planar channel.

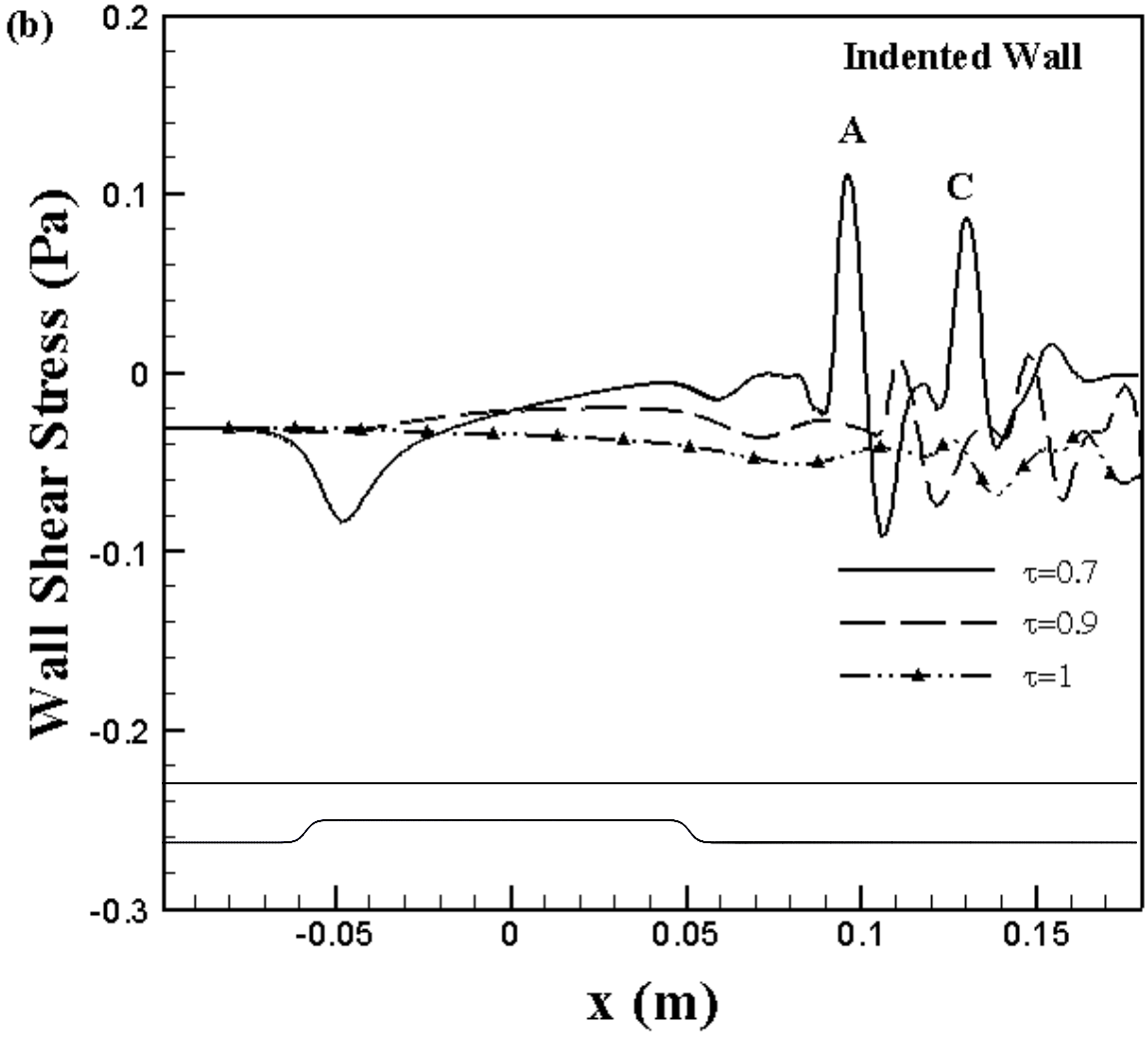

Figure 5.7 (b) Predicted wall shear stress variations during one cycle along the indented wall, τ=0.7 to 1, for a 2D-Planar channel.

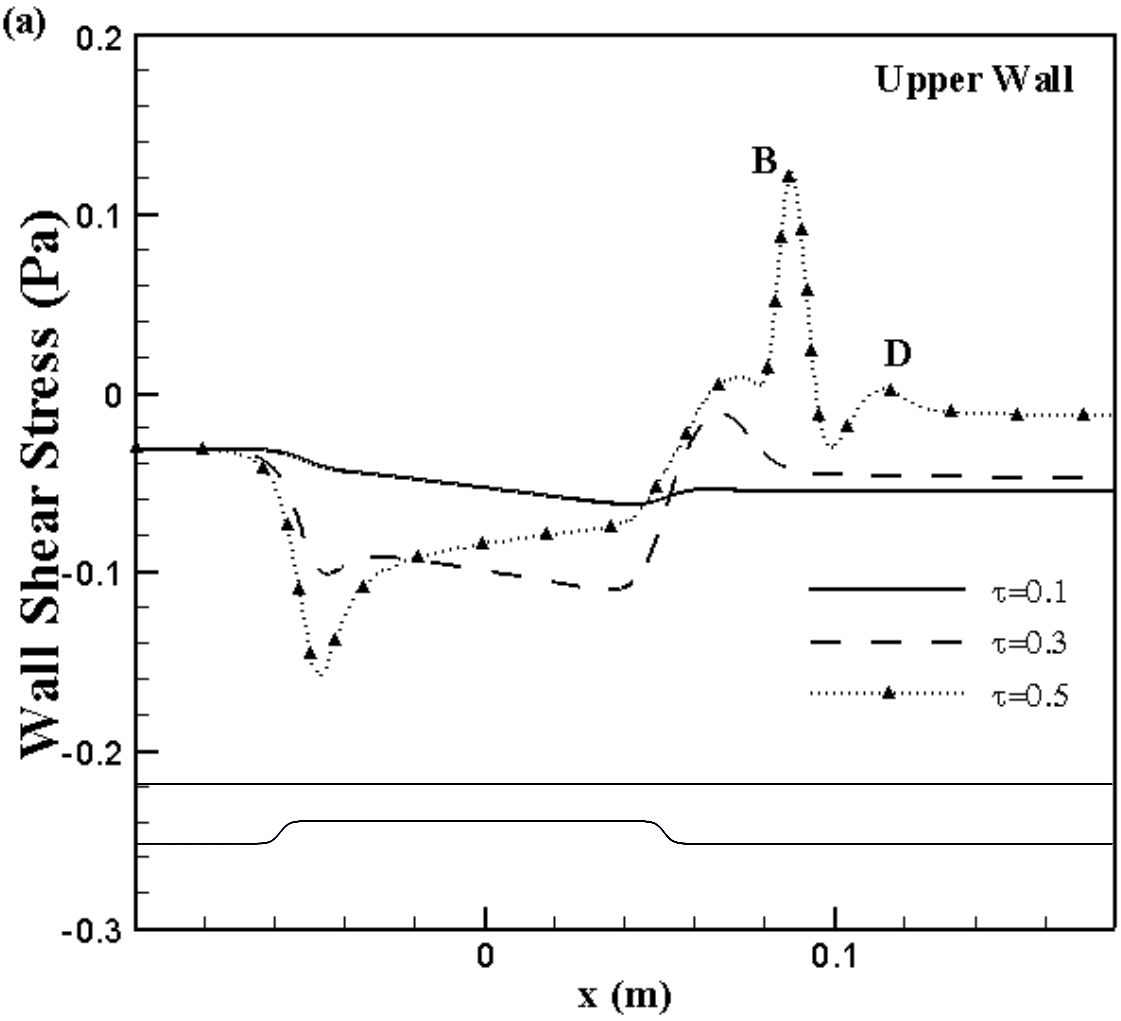

Figure 5.8 (a) Predicted wall shear stress variations during one cycle along the unindented wall, τ=0.1 to 0.5, for a 2D-Planar channel.

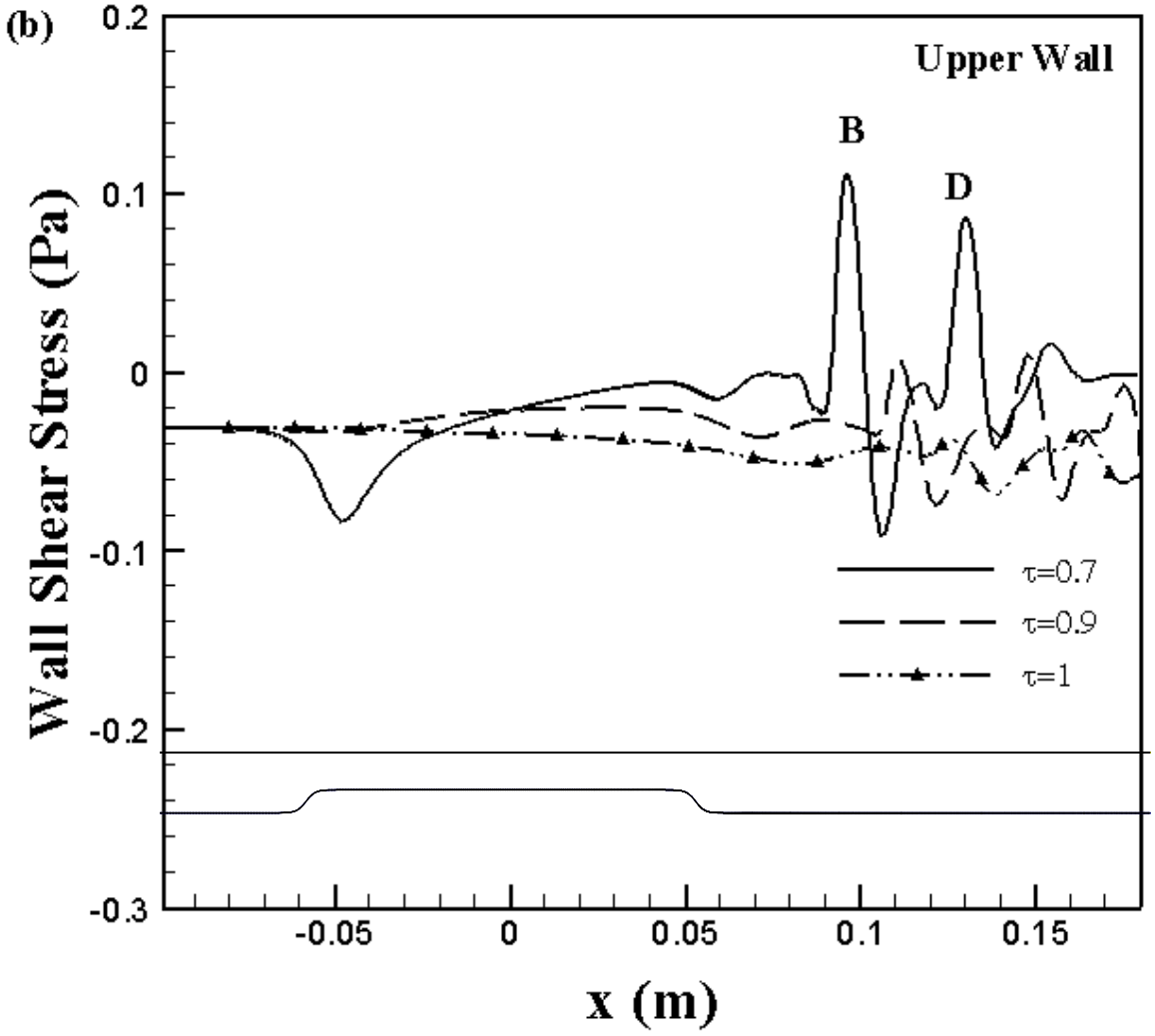

Figure 5.8 (b) Predicted wall shear stress variations during one cycle along the unindented wall, τ=0.7 to 1, for a 2D-Planar channel.

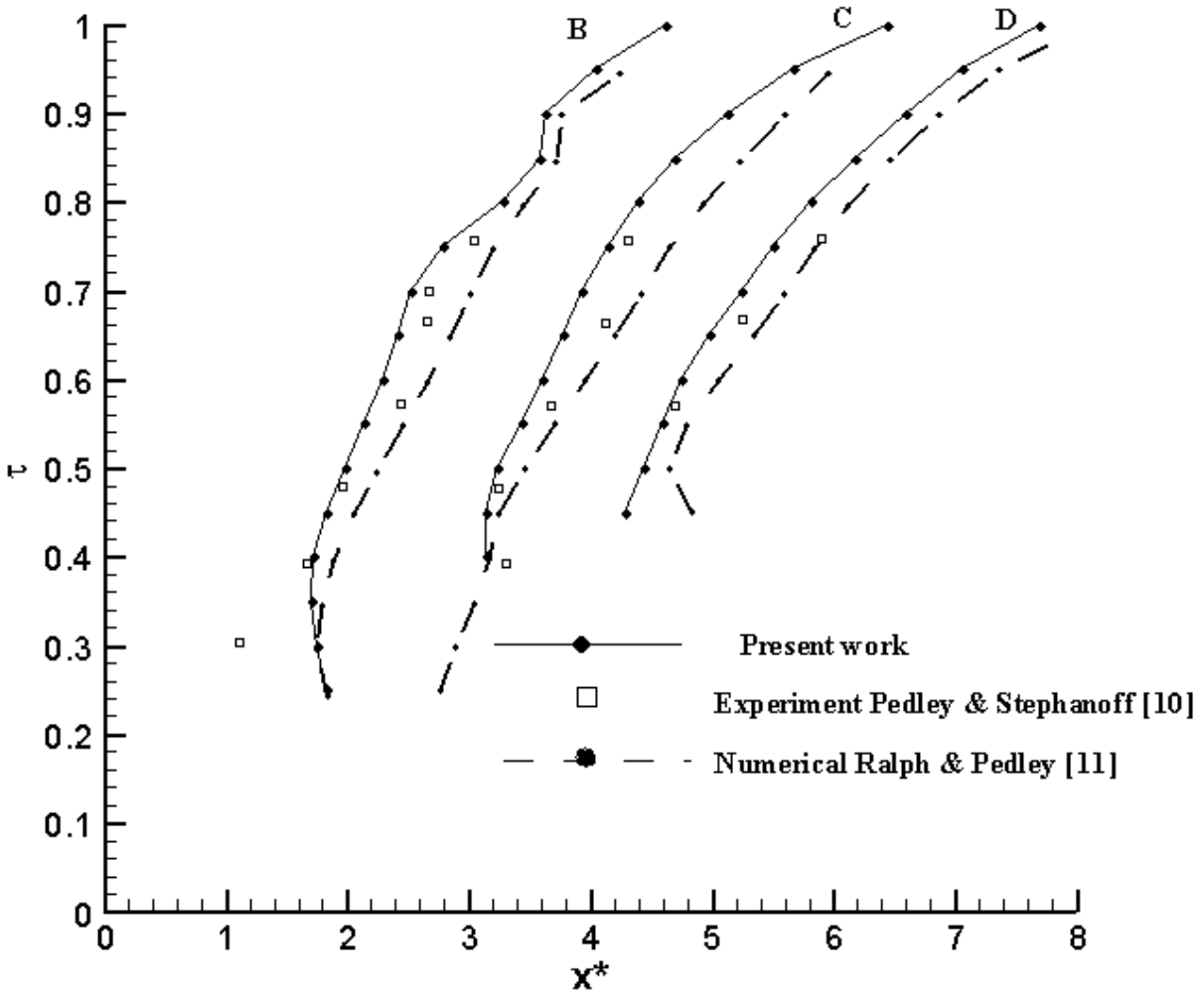

Figure 5.9 Comparison of predicted and experimentally observed position of wave crests and troughs corresponding to eddies B, C and D as functions of time for a 2D-Planar Channel.

5.2. Axisymmetric Flow in a Tube with a Moving Indentation

5.2.1. Grid Independence Test

A number of grid independence studies were carried out for the axisymmetric case. A structured grid has been used for the current computation. Three meshes with different sizes were tested: Mesh 1 with 24,400 (610 X 40) cells; Mesh 2 with 33,975 (755 X 45) cells and Mesh 3 with 39,600 (880 X 45) cells. A section of the Mesh 2 at $\tau = 0$ and $\tau = 0.5$ are shown in Figure 5.10. The grid independence test results for axial velocity and wall shear stress are shown in Figure 5.11(a), (b) and Figure 5.12 (a), (b) respectively. It may be observed that for Mesh 3 the results are in good agreement with the results of Mesh 2. Hence, the Mesh 2 is used for the computation purposes.

5.2.2. Time Dependence Test

Two time increments were used for the coarse grid calculations: $\delta t = t_0 / 1000$ and $\delta t = t_0 / 2000$. The frequency of the moving wall for the time dependence test was taken to be $f_w = 1 Hz$. Figure 5.14 shows comparison of pressure drop (P1-P3) at various time steps. The pressure drop is plotted along the sections, which are shown in Figure 5.13. The figure shows that there is no significant change between the two time increments. Hence, the fine grid calculations were carried out only with the $\delta t = t_0 / 1000$.

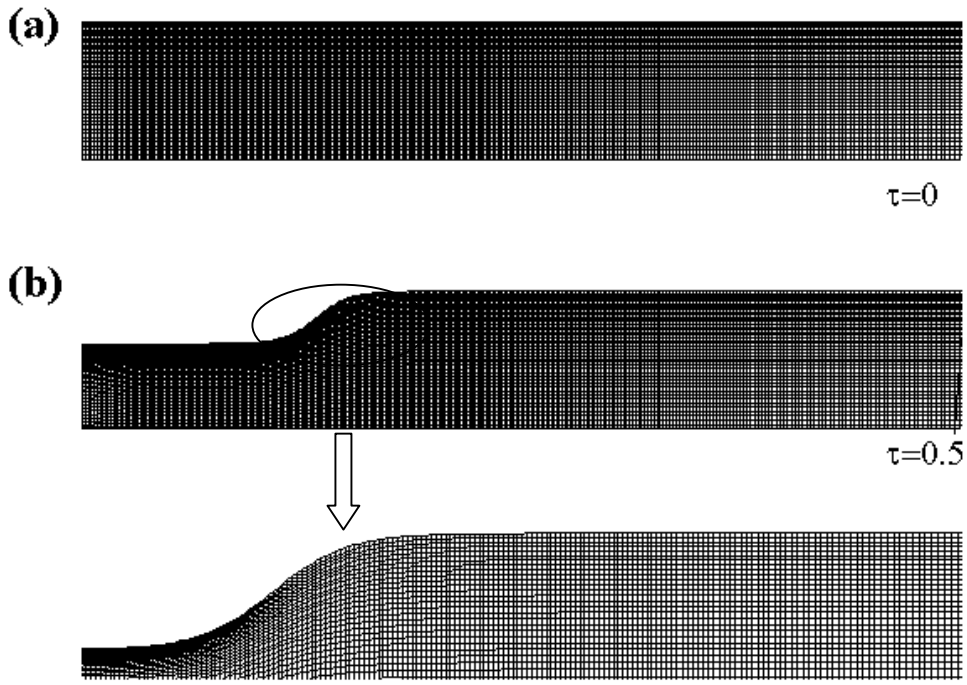

Figure 5.10 Section of the 2D-axisymmetric tube grid (33,975 cells) at (a) $\tau = 0$ and (b) $\tau = 0.5$.

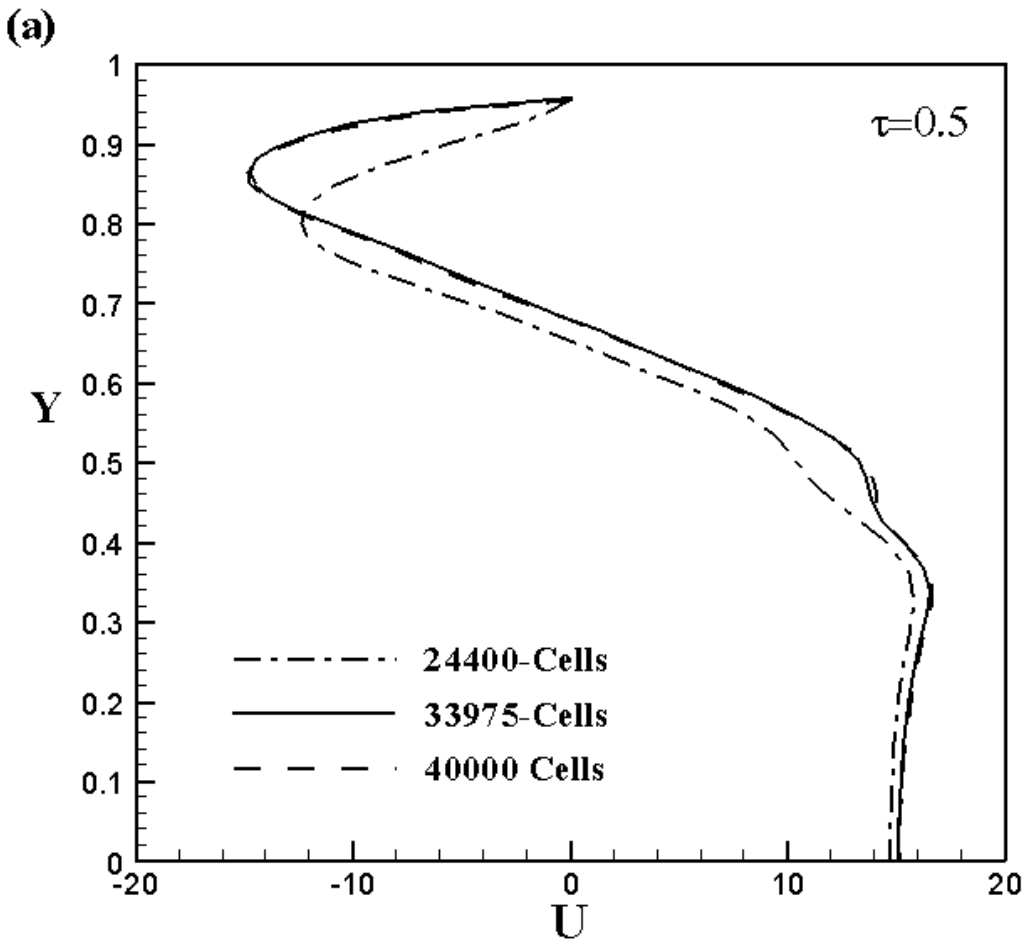

Figure 5.11 (a) Grid independent test for axial velocity at X=5.5 R at τ=0.5 for axisymmetric flow in a tube with moving indentation (Re=200, α=25).

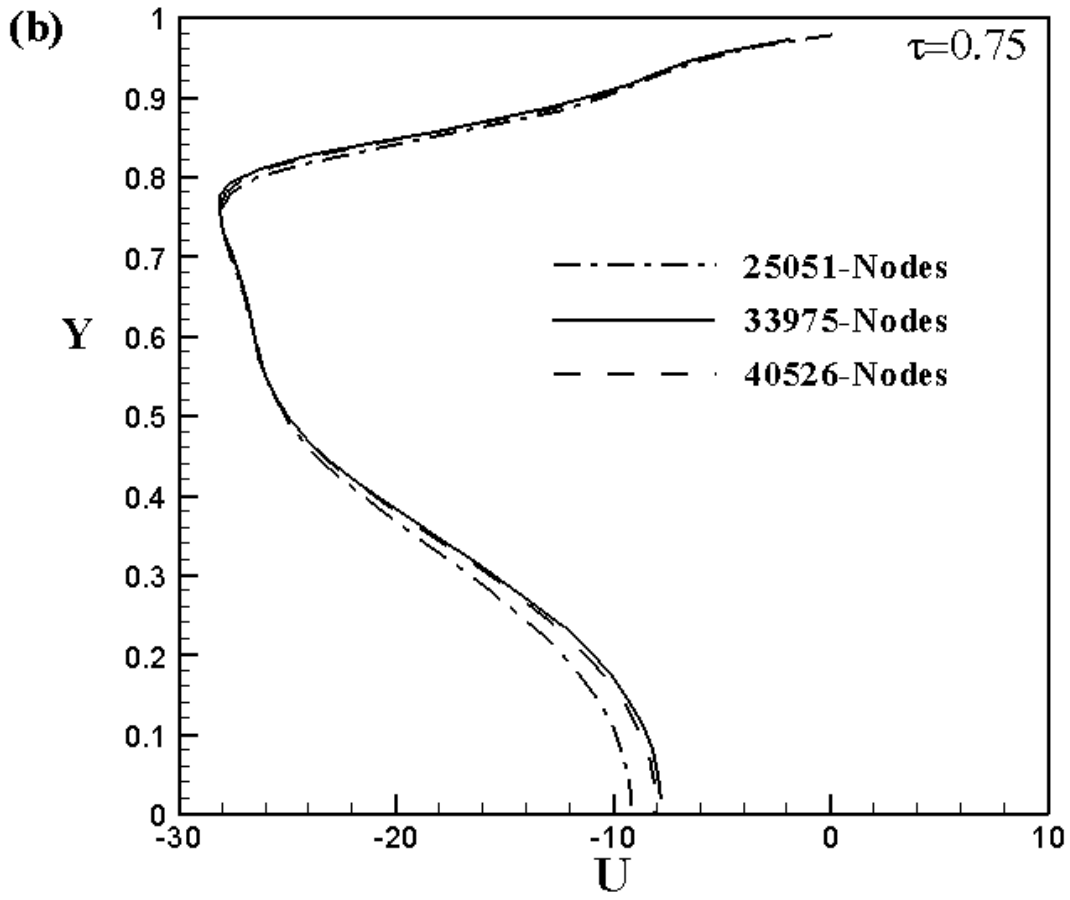

Figure 5.11 (b) Grid independent test for axial velocity at X=5.5 R at τ=0.75 for axisymmetric flow in a tube with moving indentation (Re=200, α=25).

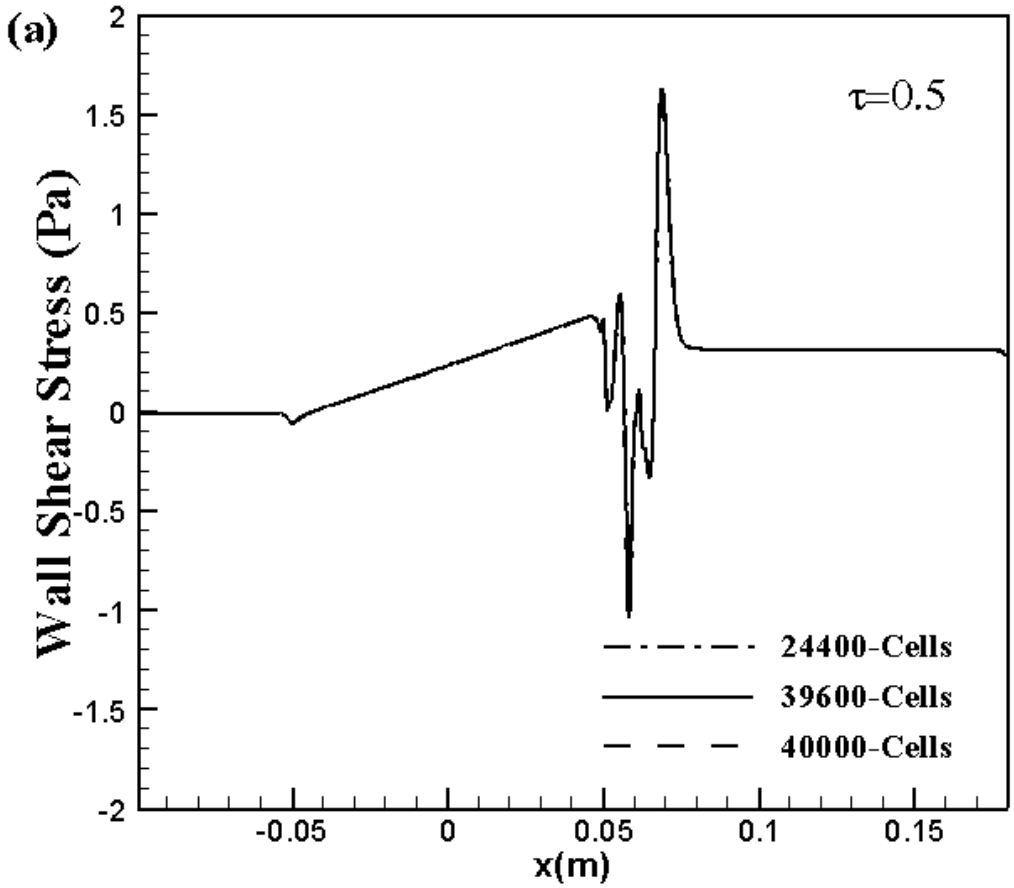

Figure 5.12 (a) Grid independent test for wall shear stress at τ=0.5 (Re=200, α=25).

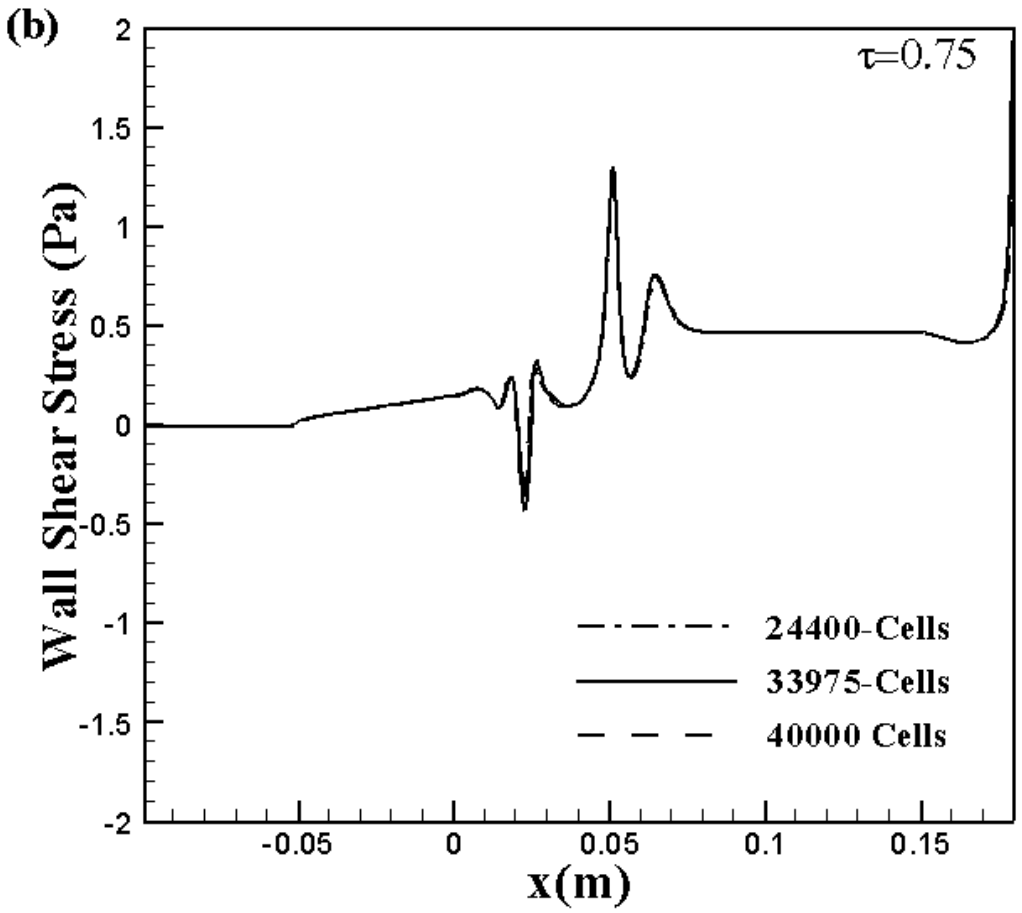

Figure 5.12 (b) Grid independent test for wall shear stress at τ=0.75 (Re=200, α=25).

The pressure drop is negative because of the moving indentation the average weighted pressure at P3 is greater than the pressure at P1.

In the present work, the following cases have been simulated:

Table 5.1 Cases simulated

Frequency	***f_w=0.1 Hz***	***f_w=1 Hz***					
Fluid	Water	Water	Newtonian Blood		Non-Newtonian Blood		
			Steady Inlet	Pulsatile Inlet	Non-Newtonian Power law	Carreau Model	Carreau-Yasuda Model
Cases	Case I	Case II	Case III	Case IV	Case V	Case VI	Case VII

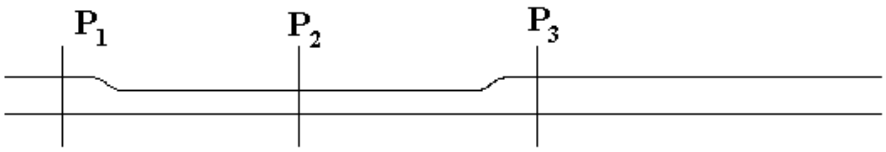

Figure 5.13 Sections at which the pressure is plotted against the time for a 2D-axisymmetric tube.

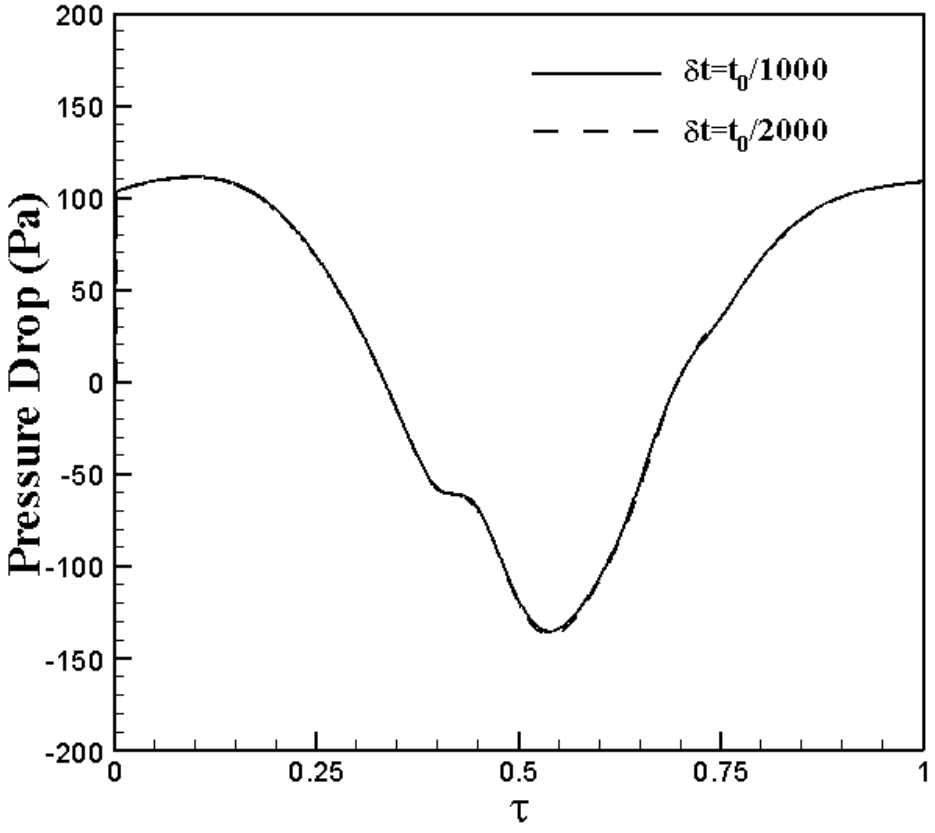

Figure 5.14 Comparison of pressure drop (P1-P3) on two different time increments at the sections shown in Figure 5.13 for a 2D-axisymmetric tube.

5.2.3. Case I-Steady Water Flow with an Indentation frequency of f_w=0.1 *Hz* (Re=200 and α=7.9)

Simulation of the water flow case was done to investigate the behavior of water flow as it is widely used in experimental investigation. The density and dynamic viscosity of water at a temperature of 20°C have values of ρ=998.2 kg/m^3 and μ=1.003x10^{-3}N.s/m^2, respectively. The volume flow rate Q_0 upstream of the moving indentation was taken to be fixed. For Re=200, Q_0=0.000190 m^3/min (190 ml/min).

Figure 5.15 (a-j) show the velocity streamlines at τ =0.1 to 1. At some time between $\tau = 0.2$ and $\tau = 0.25$, separation occurs in the lee of the indentation. During the second quarter of the period, the resulting eddy grows in its size. As the time increases, the length of the eddy increases, and moves downstream with the flow. The length of the eddy is maximum at τ=0.6 (Figure 5.15 g). As the indentation recedes back to its original position, the eddy is swept out and thus settling down to a smooth flow at τ=1.

Figure 5.16 (a), (b), (c) and (d) show the axial velocity profiles at different axial locations at different time intervals for a 2D axisymmetric tube, indentation moving at a frequency of, $f_w = 0.1 Hz$. Reverse flow is observed inside and downstream of the indentation at τ=0.75 (Figure 5.16 (c)). This is due to suction effect of the moving indentation as it moves up towards the wall.

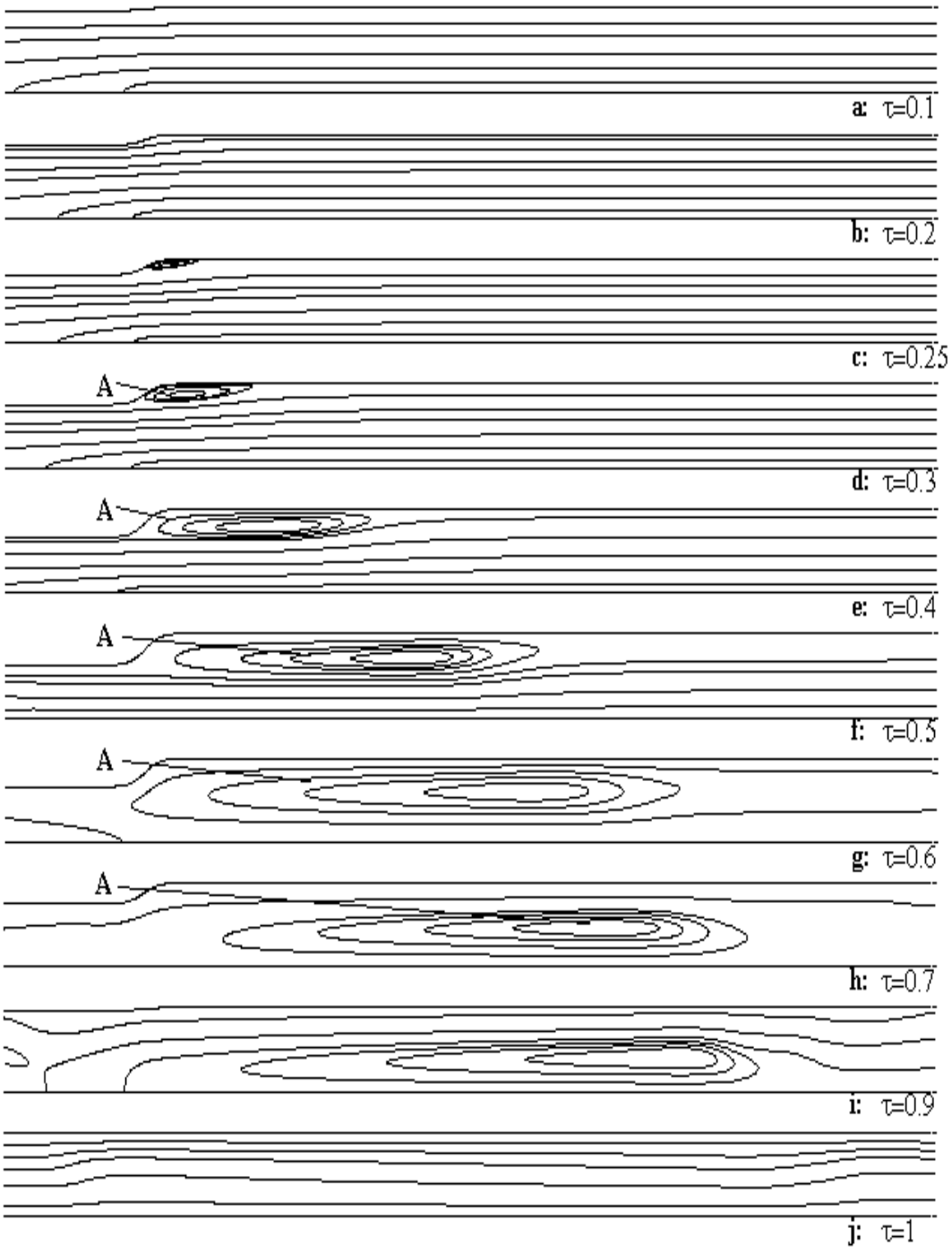

Figure 5.15 Velocity Stream lines downstream of indentation at various times τ for case I (Re=200, α=7.9).

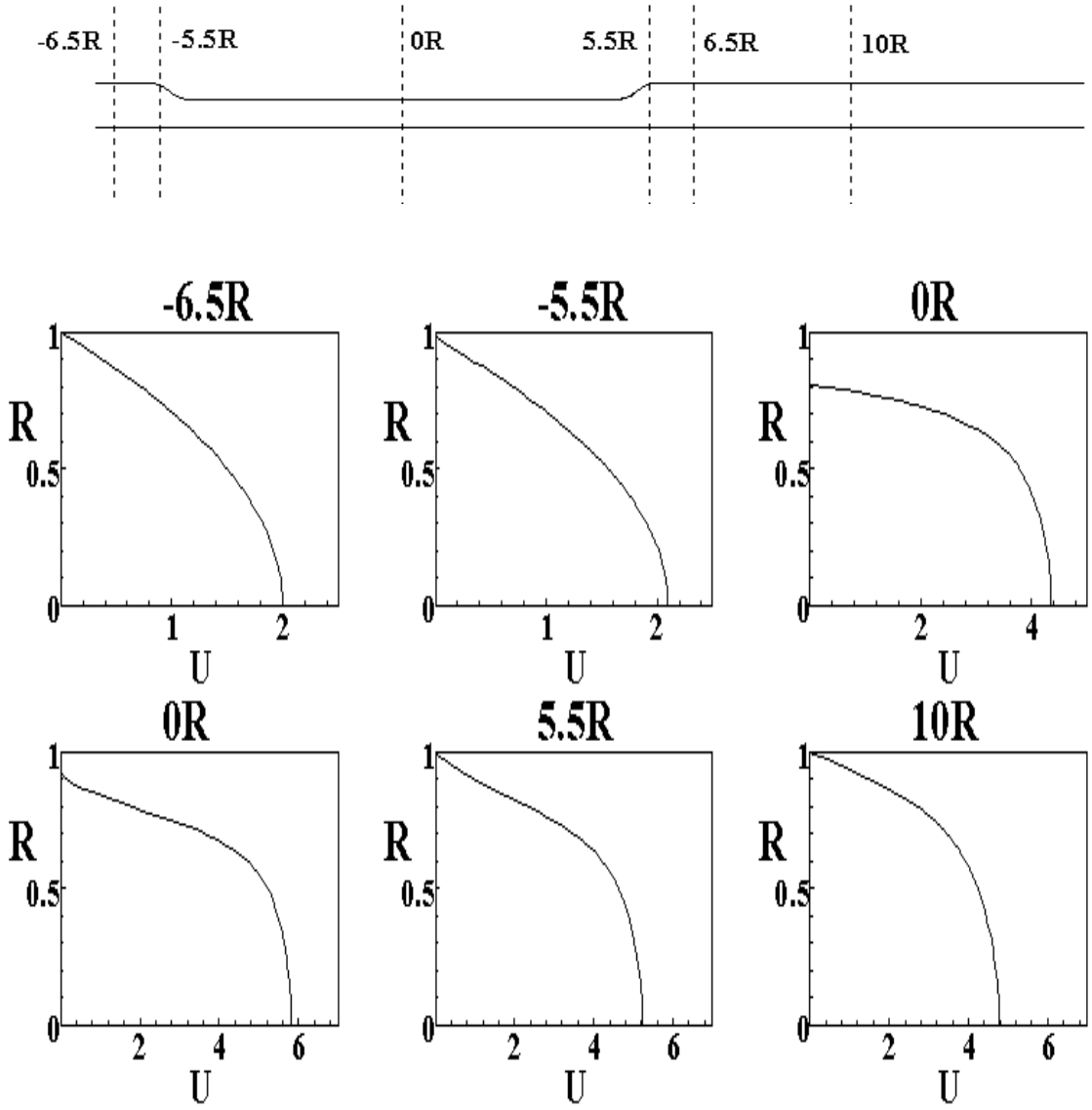

Figure 5.16 (a) Computed Axial Velocity Profiles at different cross sections of the tube for case I (Re=200, α=7.9) at τ=0.25.

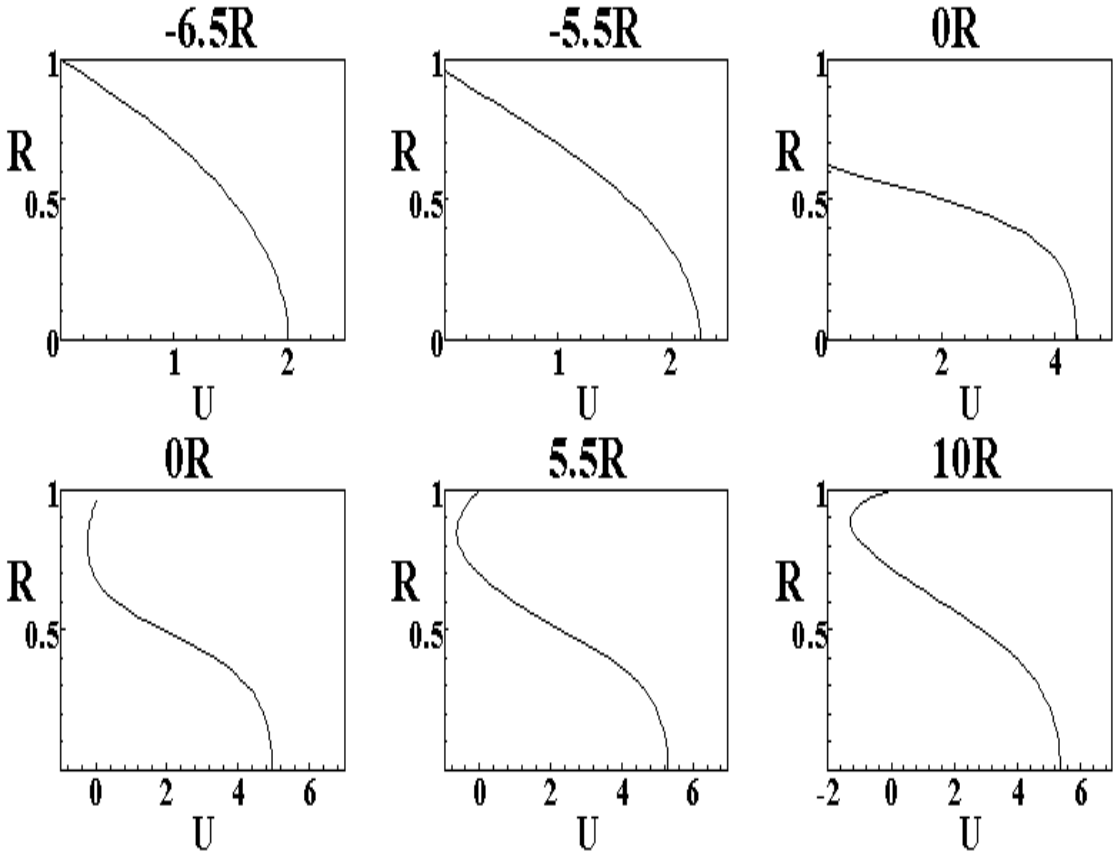

Figure 5.16 (b) Computed Axial Velocity Profiles at different cross sections of the tube for case I (Re=200, α=7.9) at τ=0.5.

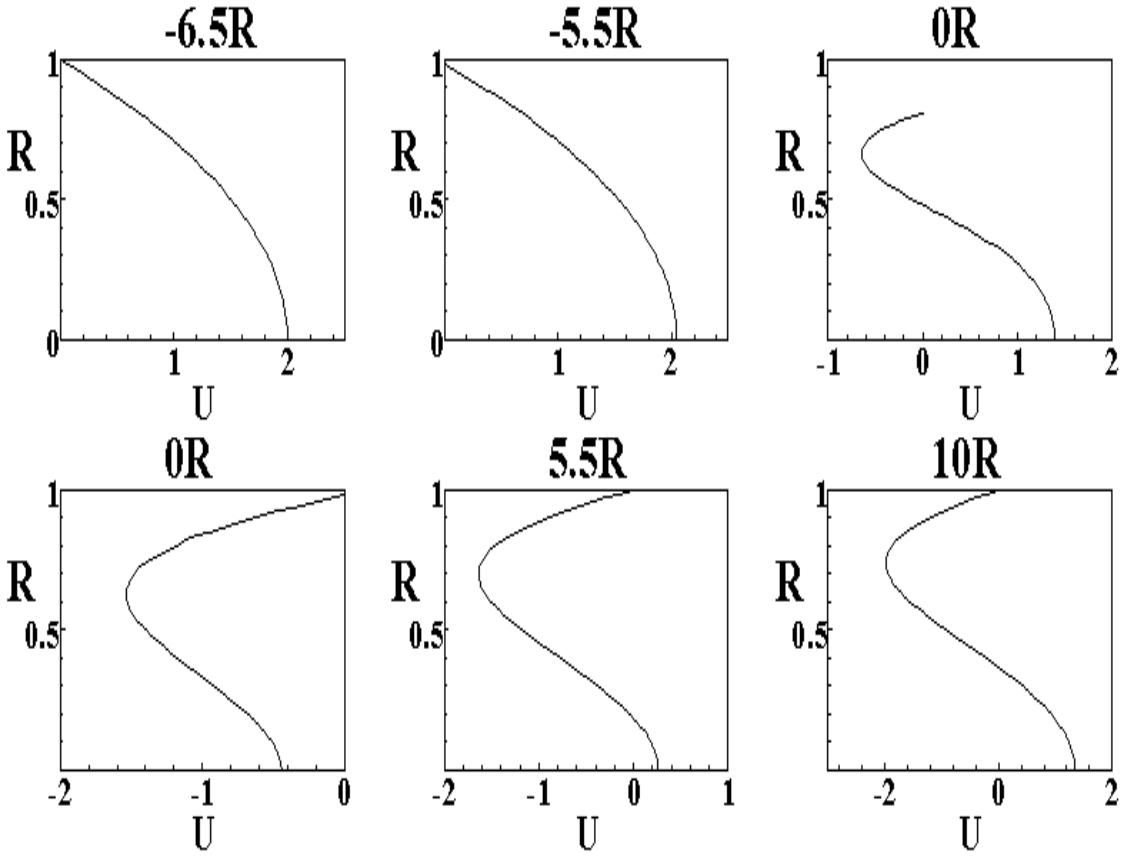

Figure 5.16 (c) Computed Axial Velocity Profiles at different cross sections of the tube for case I (Re=200, α=7.9) at τ=0.75.

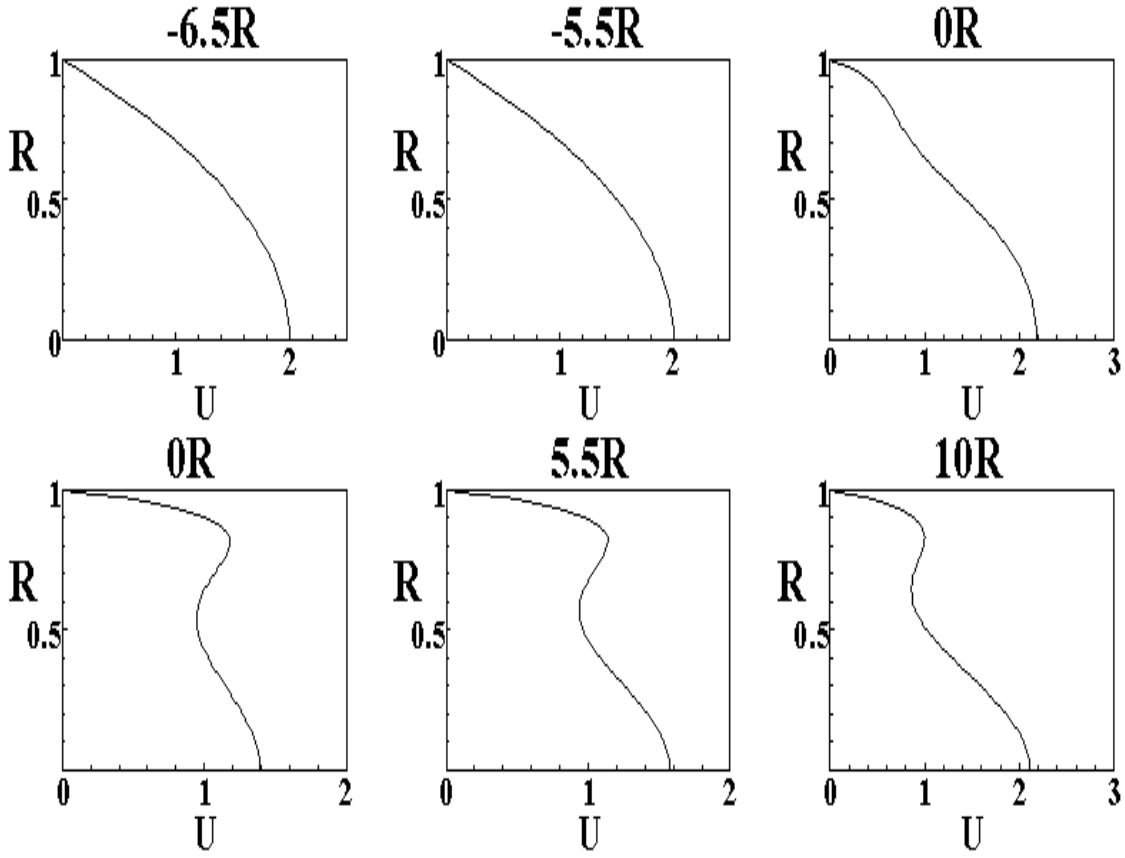

Figure 5.16 (d) Computed Axial Velocity Profiles at different cross sections of the tube for case I (Re=200, α=7.9) at τ=1.

Figure 5.17 (a) and (b) show the variation of the wall shear stress on the upper (indented) wall at various time intervals during the cycle. They indicate the strength of the eddy, the position of separation and reattachment (change of sign in wall shear stress) and thus the movement of eddy along the wall. From these figures, it can be observed that, as the time increases, the eddy is swept towards the downstream. The shear stress variation along the indentation also indicates an acceleration of the flow in this region when the indentation is moving inwards ($\tau < 0.5$); and a deceleration when it is retracting ($\tau > 0.5$). The huge jumps in the wall shear stress from τ=0.6 to τ=0.8 indicates the movement of eddy downstream of the indentation.

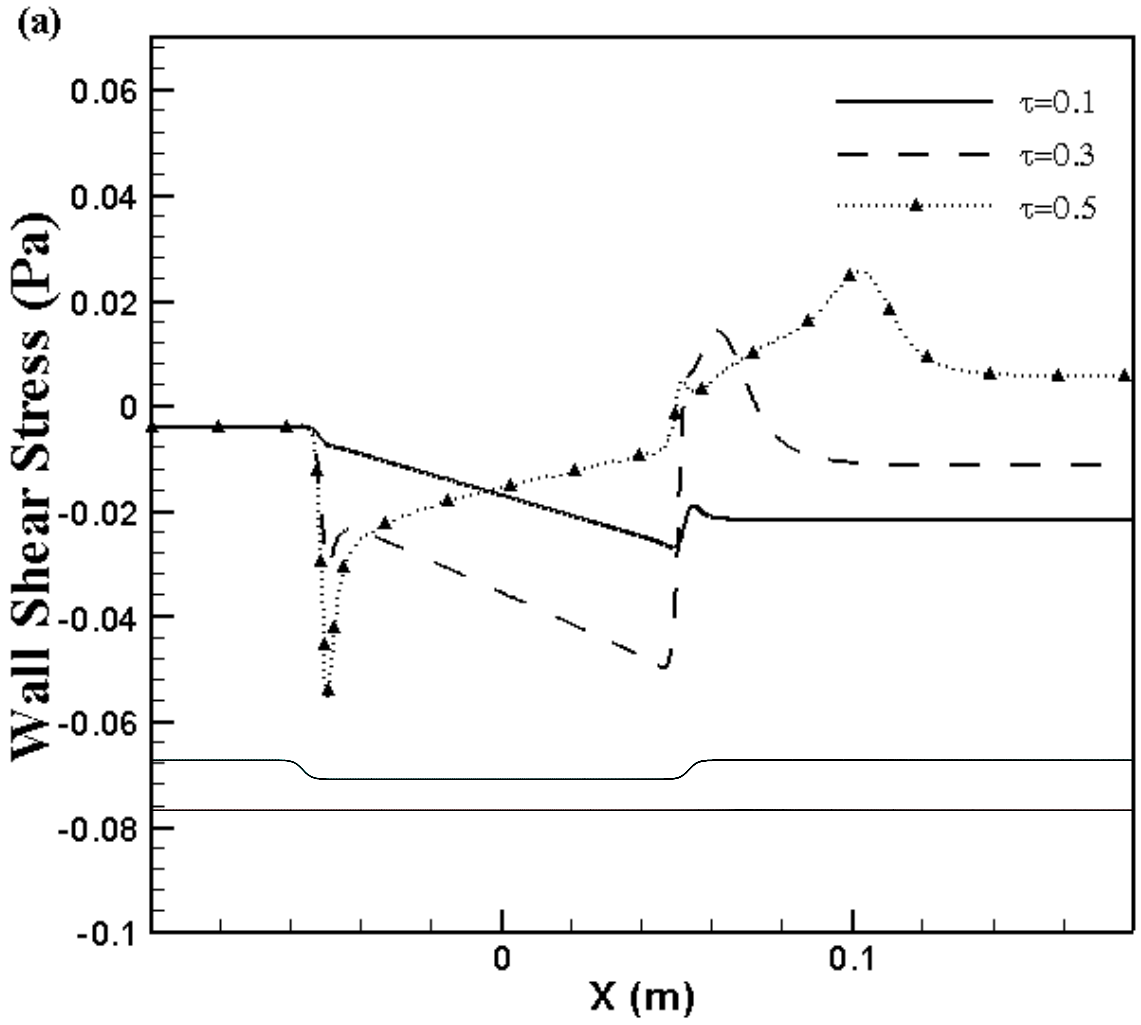

Figure 5.17 (a) Wall shear stress variations during one cycle along the indented wall, $\tau = 0.1 to 0.5$, for case I (Re=200, α=7.9).

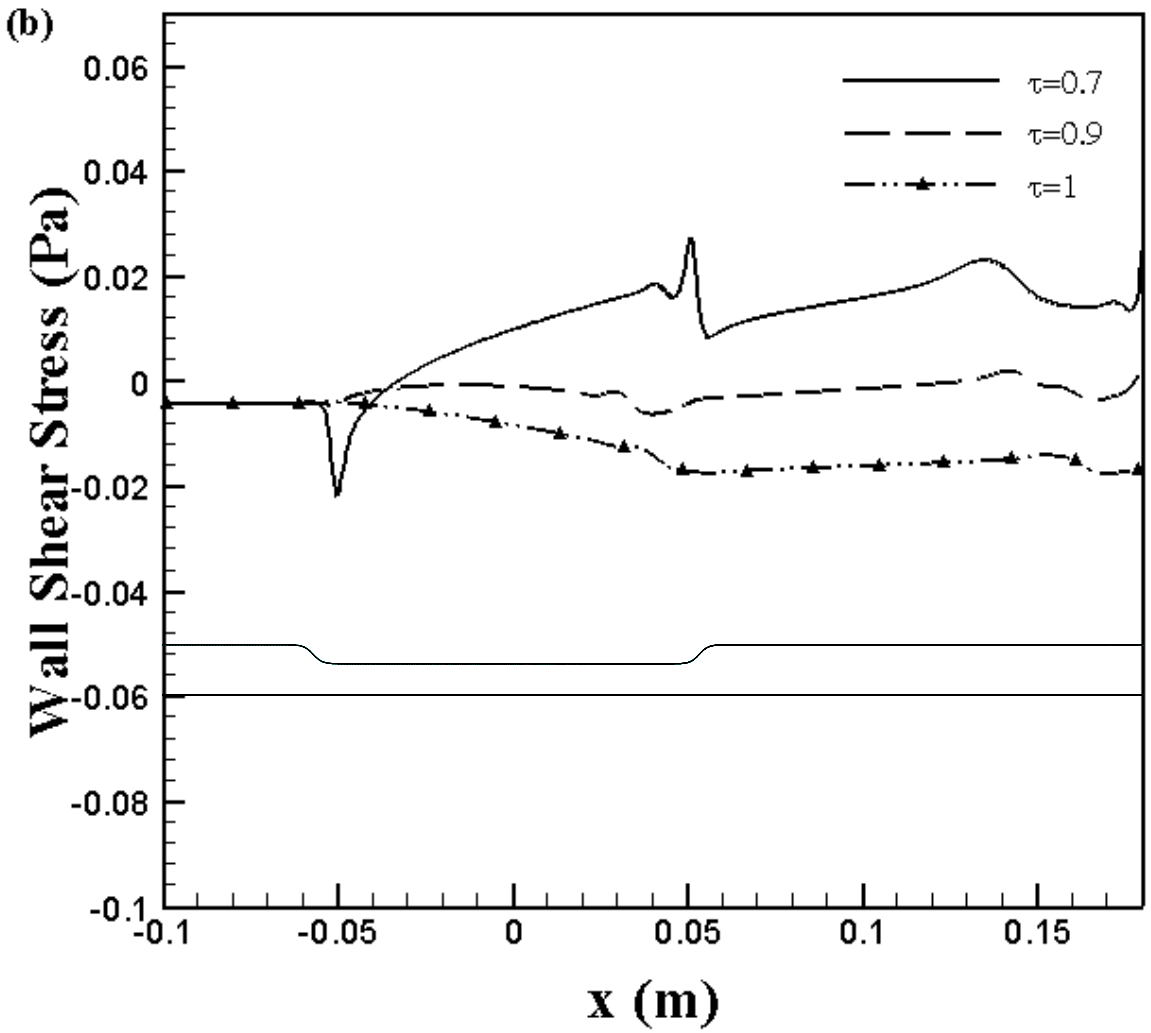

Figure 5.17 (b) Wall shear stress variations during one cycle along the indented wall, $\tau = 0.7\,to\,1$, for case I (Re=200, α=7.9).

5.2.4. Case II Steady Water Flow with an Indentation frequency of f_w=1 Hz (Re=200 and α=25)

The density and dynamic viscosity of water at a temperature of 20°C have values of ρ=998.2kg/m^3 and μ=1.003x10^{-3}N.s/m^2, respectively. The frequency of wall was set at value 1Hz representative of biological flows. The volume flow rate Q_0 upstream of the moving indentation was taken to be fixed. For Re=200, Q_0=0.000190 m^3/min (190 ml/min).

Figure 5.18 (a-p) show the velocity streamlines at τ= 0.1 to 1. Only the section downstream the indentation is shown since the flow upstream is not affected much by its movement. In the first quarter of the period, the indentation accelerates into the tube. At some time between, τ = 0.2 and 0.25 (Figure 5.18c-II) separation occurs in the lee of the indentation and an eddy A appears. The resulting eddy grows in its size and strength with time.

In the second quarter of the period, while the indentation is still advancing but decelerating into the tube, a second eddy B of opposite sign forms near eddy A. As τ increases, these eddies grow in their size and strength. At τ = 0.4, eddy A splits into a pair of co-rotating eddies (eddy A and eddy C, Figure 5.18f-II) with no reattachment point. As a result of which, a permanent region of flow reversal exists distal to the eddy B near the wall region. As τ increases these eddies grow in their size and strength and moves towards

the core of the tube. Also, the depth of the reversal flow region increases, with the time downstream of the indentation, from the wall to the core of the tube (Figure 5.18h-II).

At $\tau = 0.55$ (Figure 5.18i-II), these pair of eddies (eddies A and C) almost block the core flow in the tube and another eddy D appears in the lee of the indentation just beside the eddy B. At $\tau = 0.7$ (Figure 5.18l-II), the reversal flow, downstream of the indentation, sweeps out eddies B, C and D and weakens the eddy A. As the indentation recedes back to its original position, the reverse flow region downstream of the indentation moves back into the indentation zone. The upstream and downstream flows collide with each other in this indentation zone. Hence, at $\tau = 1$ (Figure 5.18p-II), the flow is fully disturbed in the indentation.

According to Stephanoff et al.[13], as the indented wall moves into the channel with higher frequency of oscillation, waves should develop on the core flow downstream of the moving indented wall. In the present case waves do not develop on the core flow because of axisymmetric boundary condition. The axisymmetric boundary condition does not allow the eddy to generate a cross-channel pressure gradient that may cause curvature in the mainstream. In turn, eddy splitting is observed in this case. The mechanism responsible for splitting of eddies is the same as that explained by Ralph and Pedley [43]. The streamlines of the eddy A (Figure 5.18c-II) are concentrated more near the reattachment point and consequently a secondary counter rotating separation region forms. The secondary eddy grows and the primary dividing streamline becomes kinked until primary and secondary streamlines meet and give a pair of co-rotating eddies.

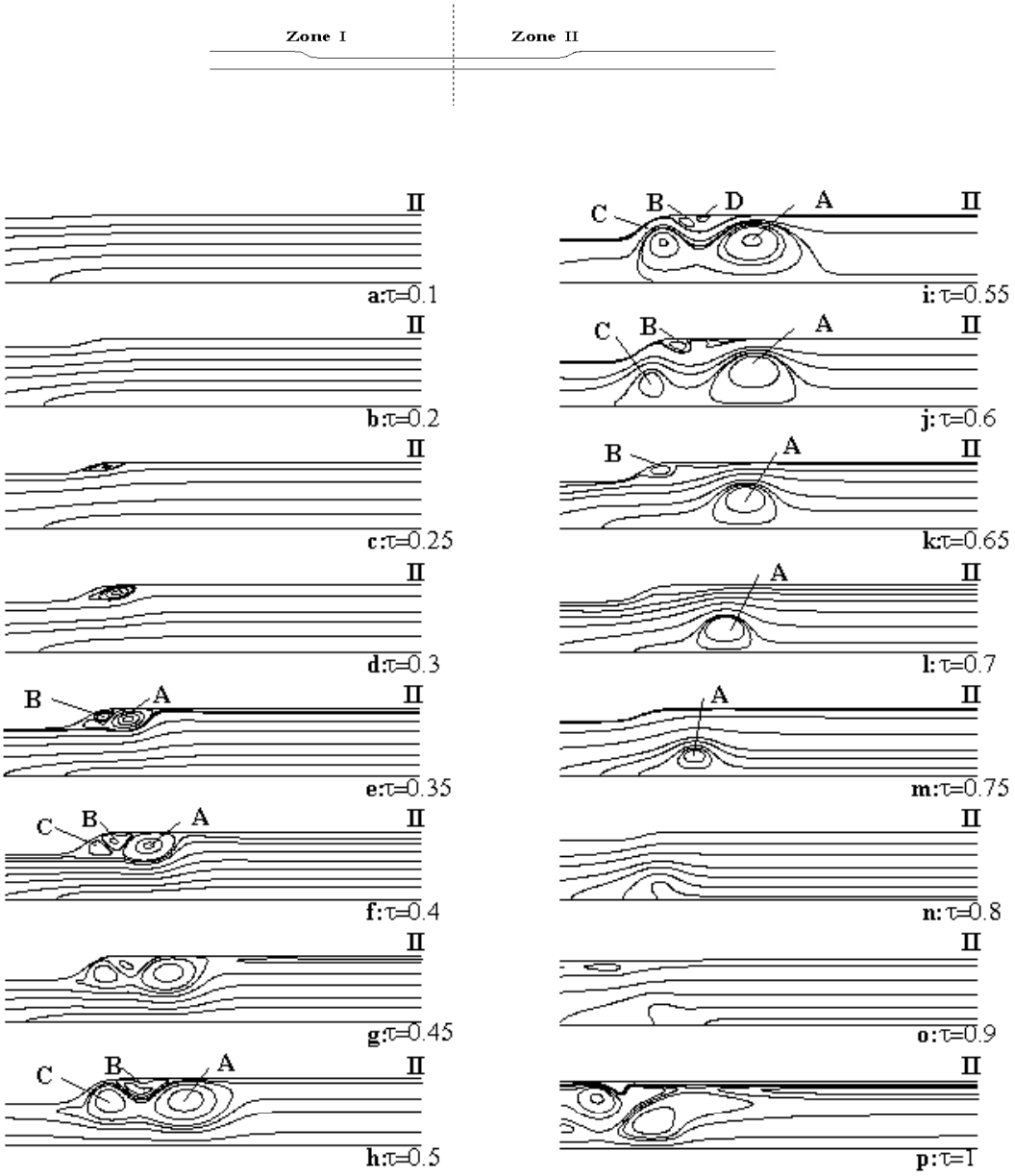

Figure 5.18 Velocity Streamlines at various times τ for case II (Re=200, α=25).

The co-rotating eddy detaches from the wall and disappears.

Figure 5.19(a) and (b) show the variation of the wall shear stress on the upper (indented) wall at various time intervals during the cycle. They indicate the strength of the eddy, the position of separation and the position of reattachment (change of sign in wall shear stress) and thus the movement of eddies along the wall. Eddy separation can be observed from these figures. The wall shear stress, acted by the fluid, upstream of the indentation is dominated mostly by the forward flow but downstream of the indentation it is strongly affected by eddies. The shear stress variation along the indentation also indicates an acceleration of the flow in this region when the indentation is moving inwards ($\tau<0.5$; $d\tau_w/dx<0$); and a deceleration when it is retracting ($\tau>0.5$; $d\tau_w/dx>0$). The wall shear stress is higher than the previous case because of the high frequency of the moving indentation.

Figure 5.20 shows the variation of pressure drop (P1-P2 and P1-P3) along the indentation shown in Figure 5.13. At the beginning of the cycle, while the indentation is accelerating, the pressure drop increases sinusoidally with the time for the first quarter of the cycle. For the second quarter of the cycle, while the indentation is decelerating in to the tube the pressure drop decreases. As the indentation starts receding late in the cycle, the pressure drop increases sinusoidally with time. The pressure drop P1-P3 is greater than the pressure drop P1-P2

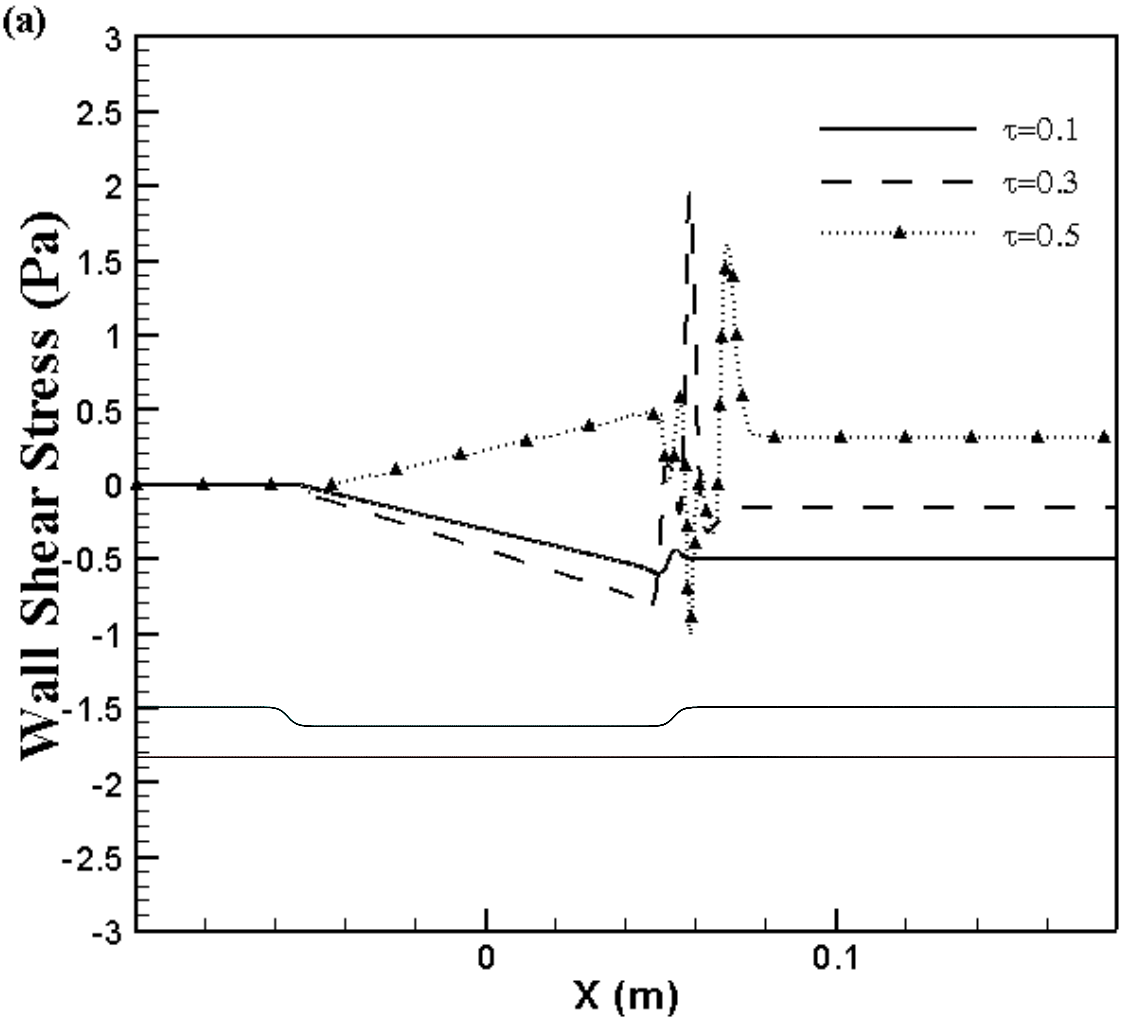

Figure 5.19 (a) Wall shear stress variations during one cycle along the indented wall $\tau = 0.1 to 0.5$ for case II (Re=200, α=25).

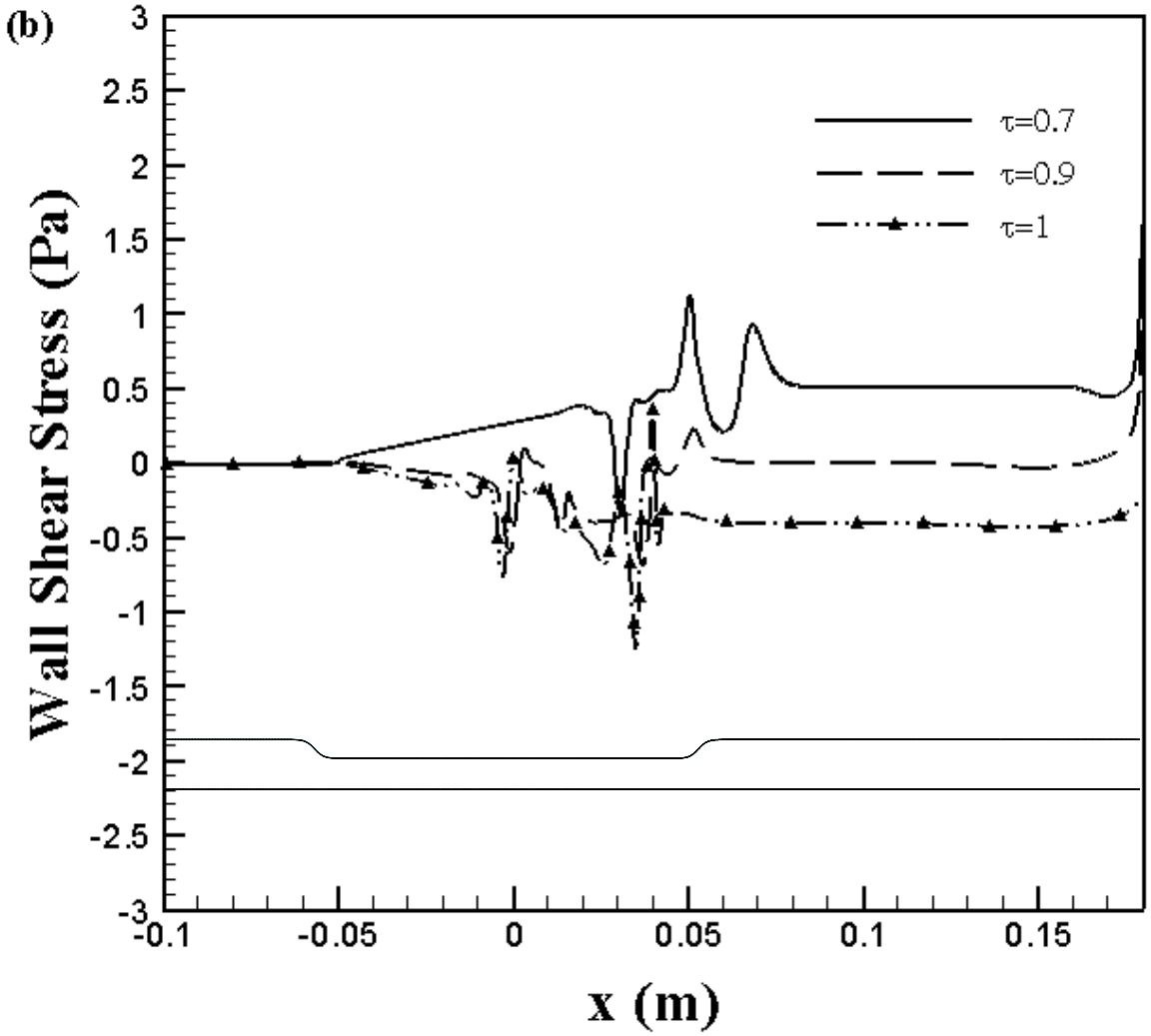

Figure 5.19 (b) Wall shear stress variations during one cycle along the indented wall $\tau = 0.7\,to\,1$ for case II (Re=200, α=25).

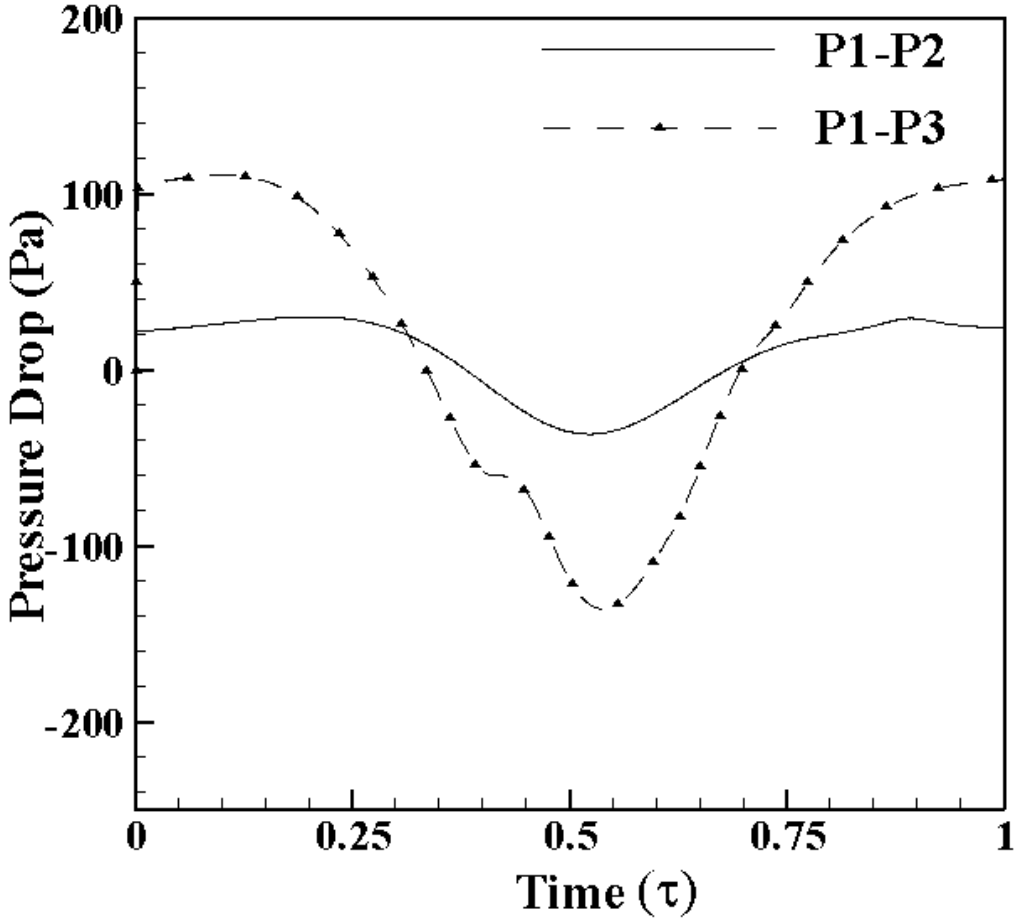

Figure 5.20 Pressure Drop along the indentation for case II (Re=200, α=25).

5.2.5. Case III Steady Newtonian Blood Flow at Inlet with an Indentation frequency of f_w=1 Hz (Re=200, α=13.4)

Eventually we are interested in simulating blood flow. In many studies blood is assumed to be a Newtonian fluid. This is also assumed in this case. For isothermal conditions, the density and dynamic viscosity of blood are taken as ρ=1060kg/m^3 and μ=3.71x10^{-3}N.s/m^2, respectively. The frequency of wall was set at value 1Hz representative of biological flows. The volume flow rate Q_0 upstream of the moving indentation was taken to be fixed. For Re=200, Q_0=0.000660 m^3/min (660 ml/min).

Figure 5.21 (a-p) show the velocity streamlines at τ= 0.1 to 1. In the first quarter of the period, the indentation accelerates into the tube. At some time between, τ = 0.2 and 0.25 (Figure 5.21b-II and c-II) separation occurs in the lee of the indentation and an eddy A appears. The resulting eddy grows in its size and strength with no reattachment point. As a result, a region of flow reversal exists distal to eddy A, near the wall region, downstream of the indentation.

At τ = 0.45 a second, eddy B of opposite sign forms near eddy A (Figure 5.21g) and the eddy A grows in its size and moves towards the core of the tube. At τ = 0.55 (Figure 5.21i), eddy A almost blocks the core flow and the thickness of the reversal flow region increases, downstream of the indentation. At τ = 0.65 (Figure 5.21k), the reverse flow

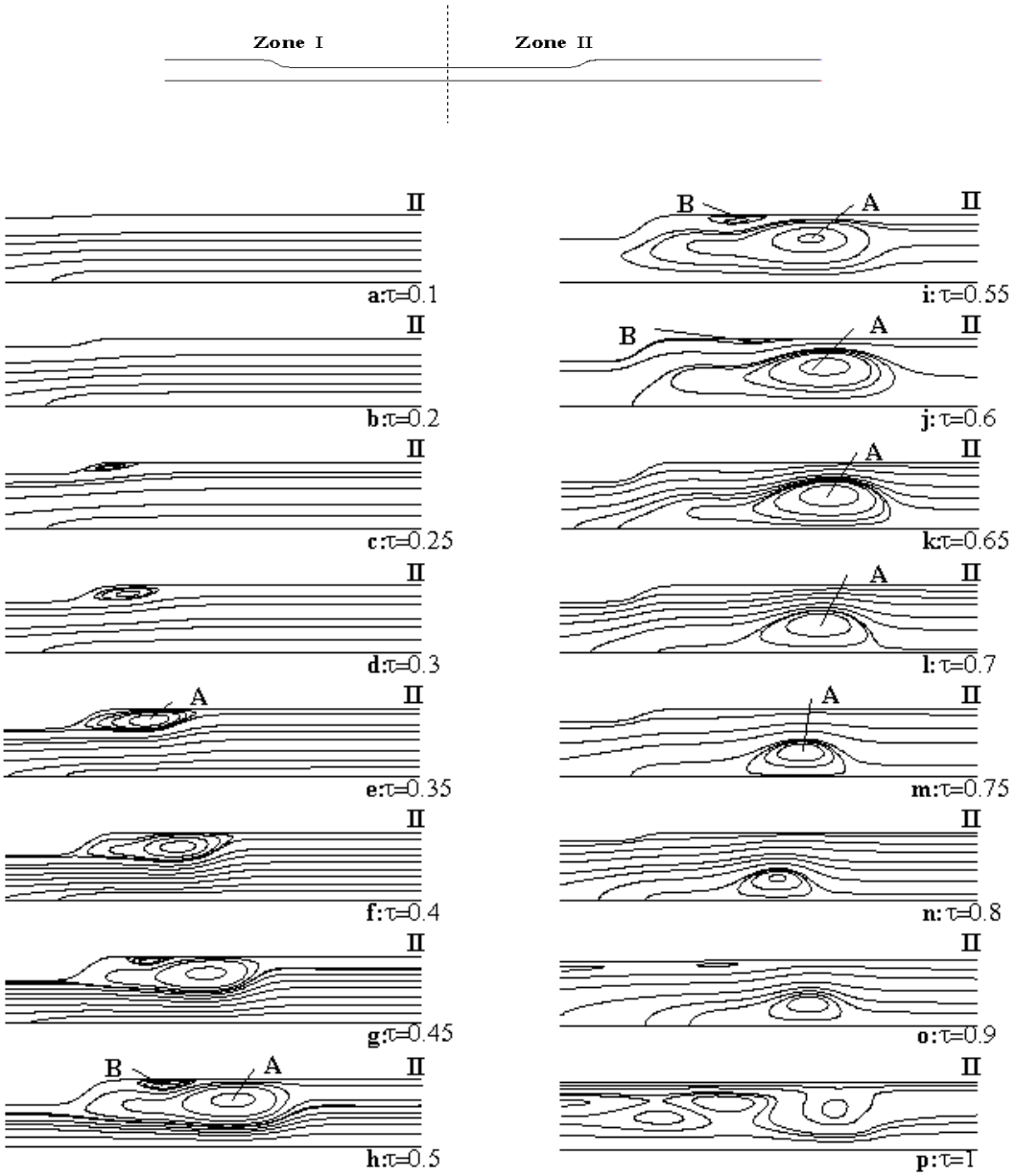

Figure 5.21 Velocity Streamlines at various times τ for steady blood flow-Case III (Re=200, α=13.4).

from the downstream of the indentation sweeps out eddy B. As the indentation recedes back to its original position, the reverse flow region at the downstream moves back into the indentation and collides with the upstream coming flow. Hence, at $\tau = 1$(Figure 5.21r), the flow is fully disturbed in the indentation. Flow does not recover for the next cycle. It may take three or four more cycles to recover the flow.

Figure 5.22 (a) and (b) show the variation of the wall shear stress on the upper (indented) wall at various time intervals during the cycle. They indicate the strength of the eddy; the position of separation and the position of reattachment (change of sign in wall shear stress) and thus the movement of eddies along the wall. Eddy separation can be observed from these figures. The wall shear stress upstream of the indentation is dominated mostly by the forward flow but downstream of the indentation it is strongly affected by the eddies. The shear stress variation along the indentation also indicates an acceleration of the flow in this region when the indentation is moving inwards ($\tau<0.5$; $d\tau_w/dx<0\ \tau < 0.5$; $d\tau_w/dx<0$); and a deceleration when it is retracting ($\tau>0.5$; $d\tau_w/dx>0\ \tau > 0.5$; $d\tau_w/dx > 0$). The shear stresses are higher for the blood compared to water.

Figure 5.23 shows the variation of pressure drop (P1-P2 and P1-P3) across the sections shown in Figure 5.13. For the first quarter of the cycle, the pressure drop increases with the time, while for the second quarter; the pressure drop decreases with time. As the indentation starts receding late in the cycle, the pressure drop

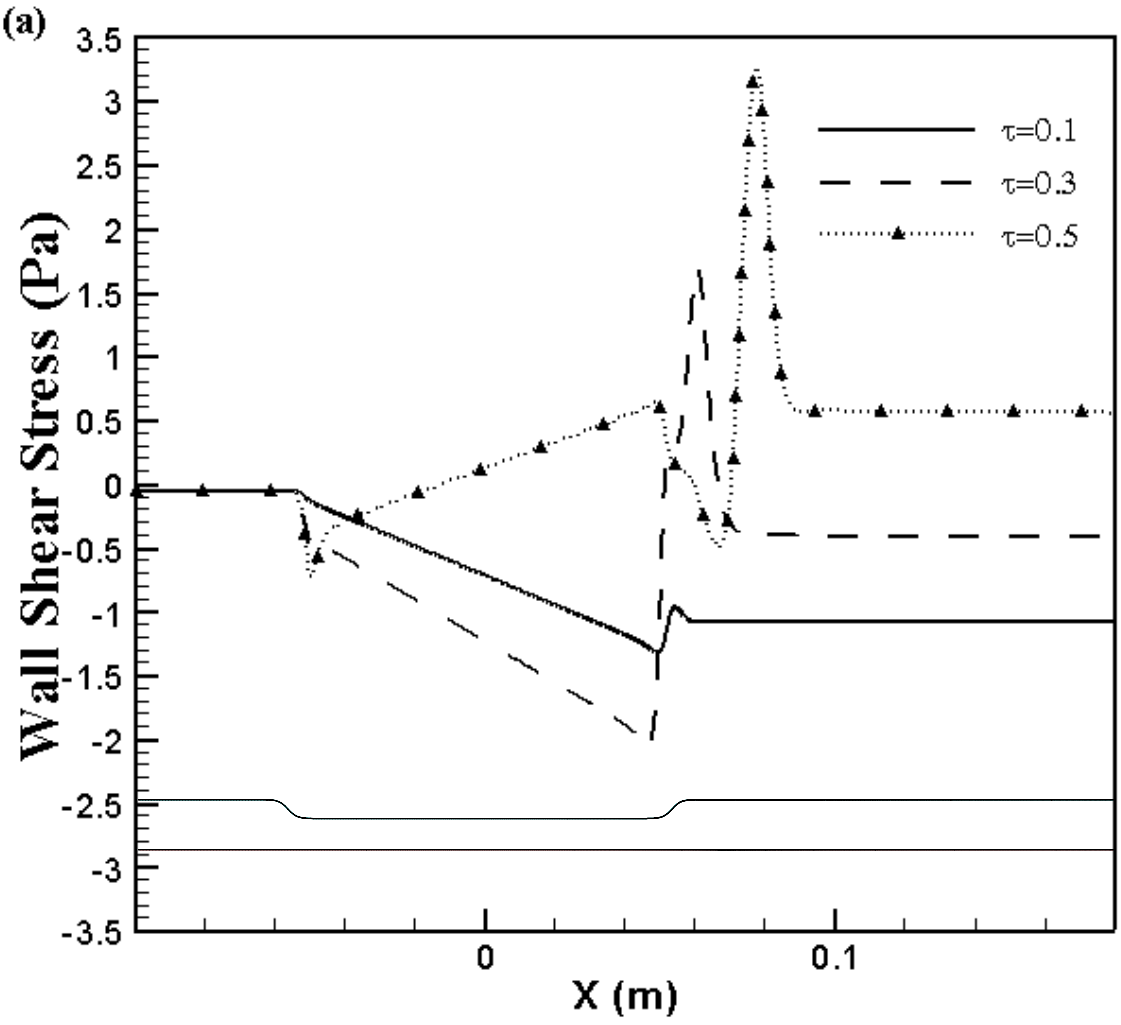

Figure 5.22 (a) Wall shear stress variations during one cycle along the indented wall $\tau = 0.1 to 0.5$ for steady blood flow-Case III (Re=200, α=13.4).

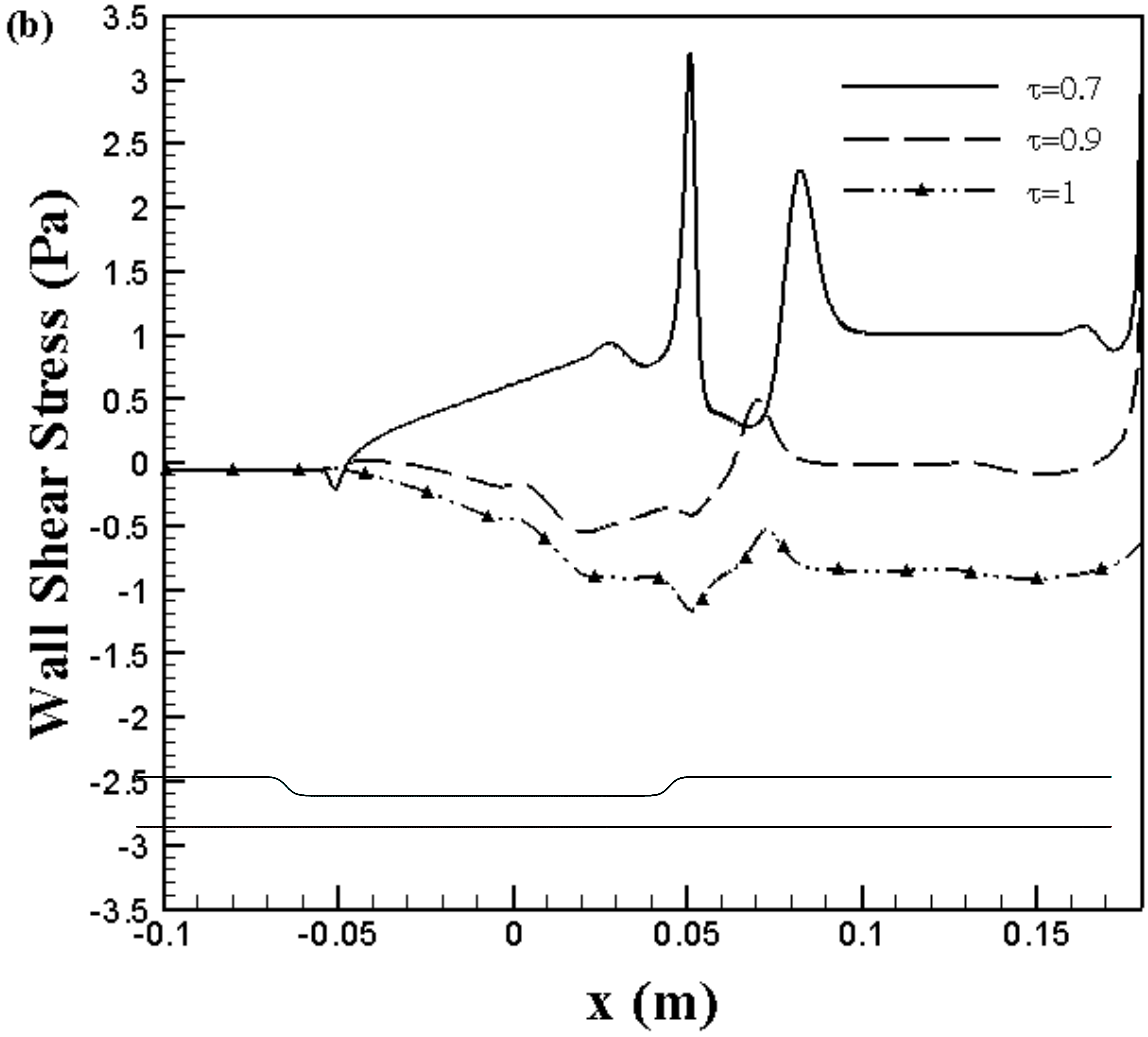

Figure 5.22 (b) Wall shear stress variations during one cycle along the indented wall $\tau = 0.7 to 1$ for steady blood flow-Case III (Re=200, α=13.4).

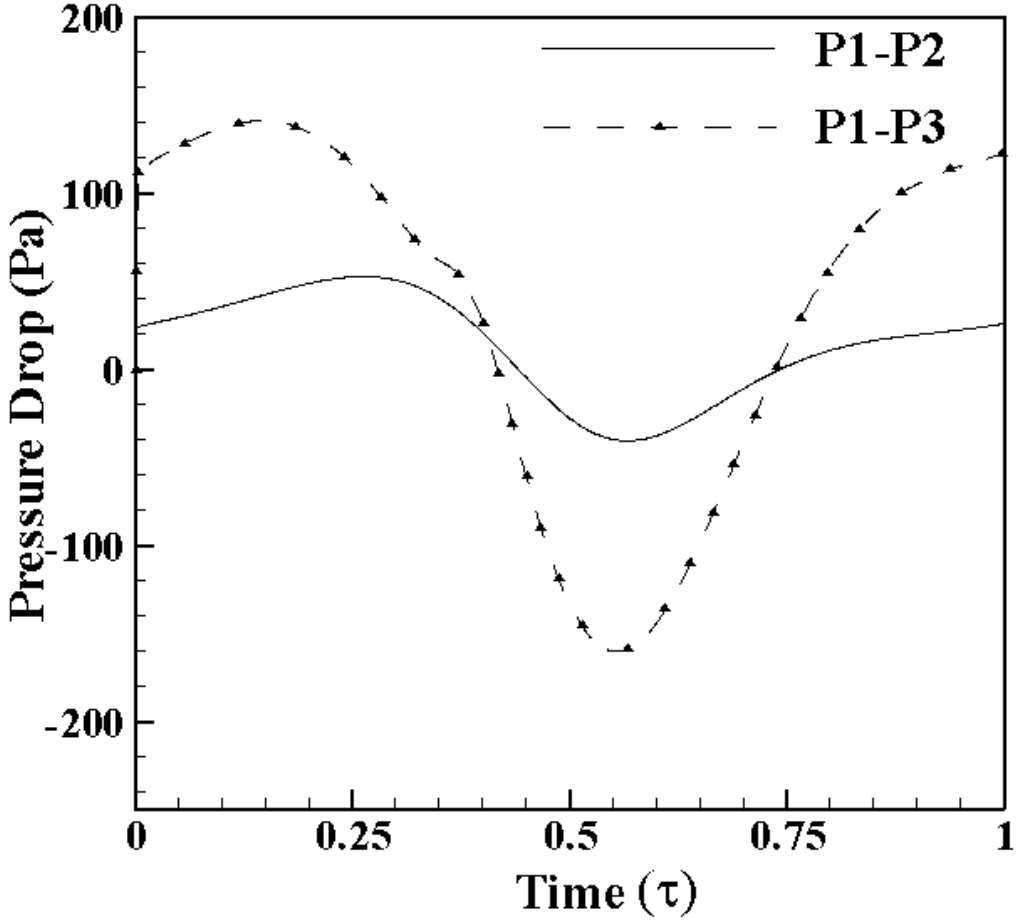

Figure 5.23 Pressure distribution at three different points for steady blood flow-Case III (Re=200, α=13.4).

increases with time showing a sinusoidal pattern. The pressure drop P1-P3 is greater than the pressure drop P1-P2.

5.2.5.1. Comparison Of Water And Blood Flow

Figure 5.24 (a-d) shows the comparison of axial velocity profiles of high and low viscous (blood and water) fluids at different cross sections at various time intervals. The velocities are high for both cases just after the indentation (5.5R). The velocities are not high inside the indentation because of the forward flow upstream of the indentation. It can be observed that the velocity profiles of the blood are damped because of its high viscosity. Hence the blood has low axial velocities in compare with that of water. The velocity profiles also show the separation and recirculation zones. From the figure, it can also be viewed that the reverse flow dominates at the downstream of the indentation as the τ increases.

The main difference that exist between the water and blood is eddy doubling. Doubling of eddy is not observed in the case of blood because of its high viscosity. Concentrating on eddy A, it appears that a detached co-rotating recirculation is about to be formed at τ=0.45 (Figure 5.21h) however it is weak and fails to double the eddy A. Hence, the eddy doubling is not observed in this case. The wall shear stresses obtained for the blood are greater than that of the water because of the higher viscosity of the blood.

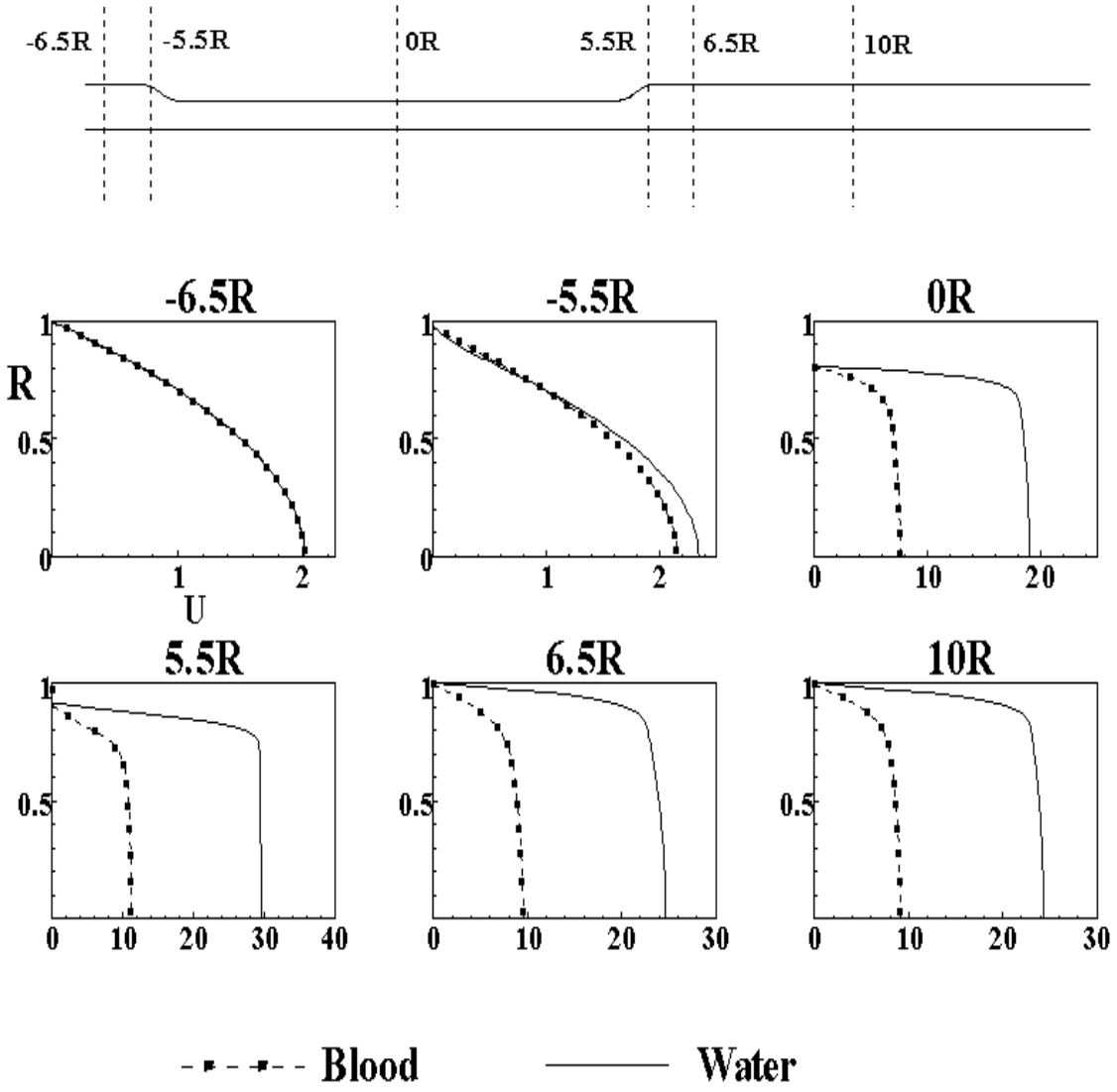

Figure 5.24 (a) Comparison of Axial Velocity profiles for steady blood flow ((Re=200, α=13.4) and steady water flow (Re=200, α=25) at τ=0.25.

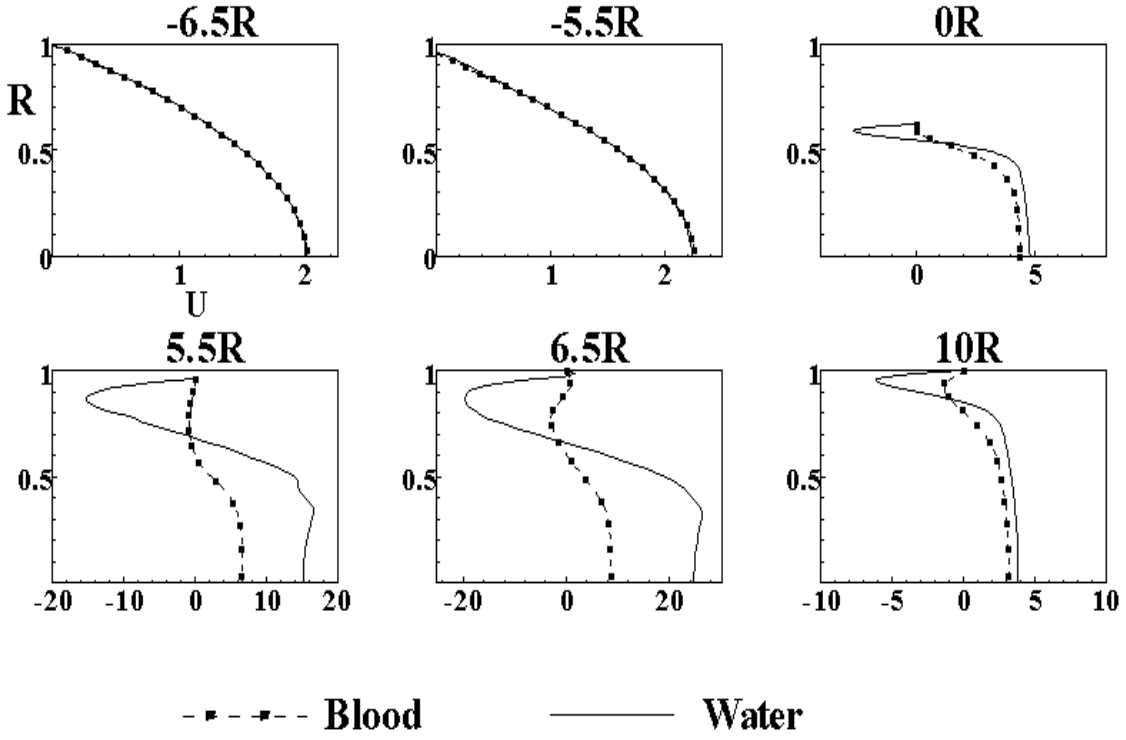

Figure 5.24 (b) Comparison of Axial Velocity profiles for steady blood flow ((Re=200, α=13.4) and steady water flow (Re=200, α=25) at τ=0.5.

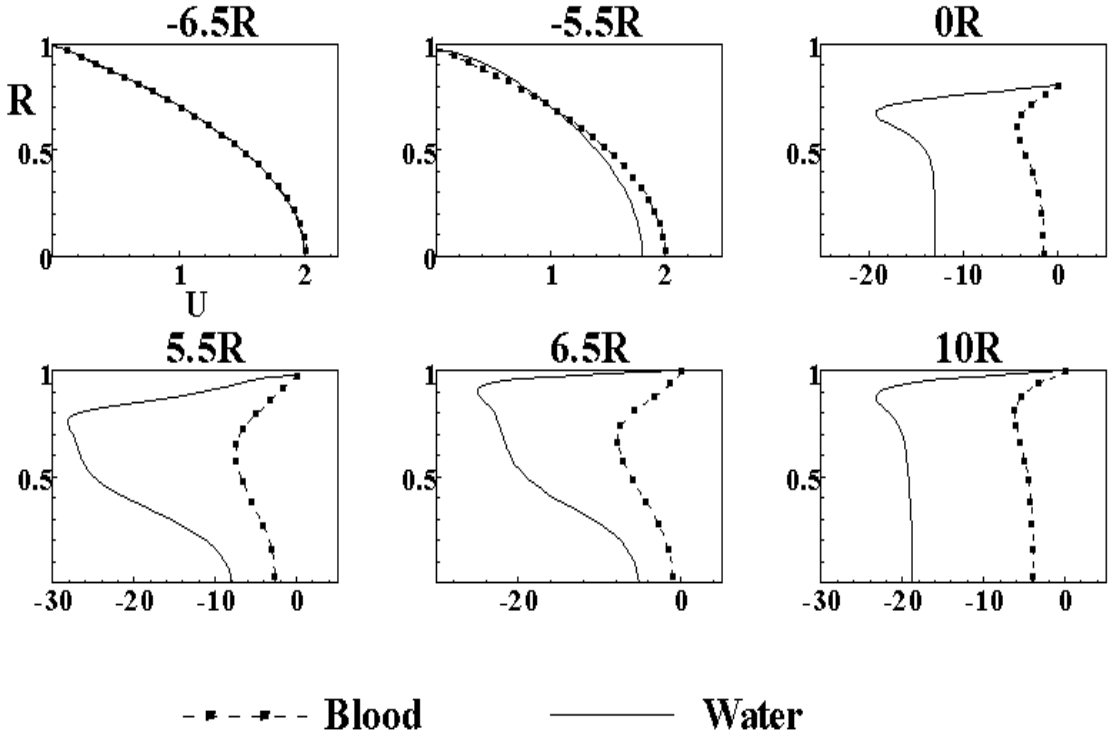

Figure 5.24 (c) Comparison of Axial Velocity profiles for steady blood flow ((Re=200, α=13.4) and steady water flow (Re=200, α=25) at τ=0.75.

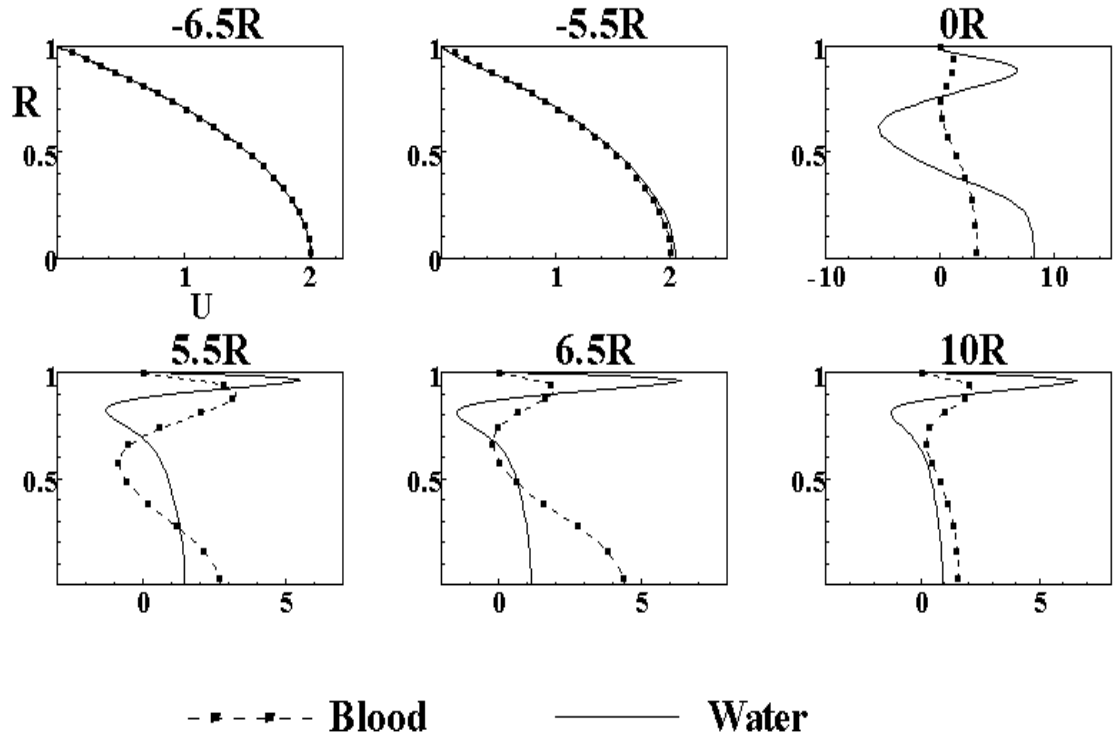

Figure 5.24 (d) Comparison of Axial Velocity profiles for steady blood flow ((Re=200, α=13.4) and steady water flow (Re=200, α=25) at τ=1

5.2.6. Case IV Pulsatile Newtonian Blood Flow at Inlet (Re=200, α=13.4.)

In this case pulsatile blood flow is simulated, which is more close to the physiological blood flow in arteries. The input waveform is shown in Figure 5.25. The input pulse selected is sinusoidal i.e.

$$U = 2(U_0 + U_m Cos(\omega t))\left(1 - \left(\frac{r}{r_0}\right)^2\right) \qquad 5.1$$

Here U_0=0.035 m/sec and U_m=0.02275 m/sec. The input pulse selected gives an average volume flow rate of $Q_0=6.6x10^{-4}$ m^3/min (660 ml/min) and a peak volume flow rate of $1.089x10^{-3}$ m^3/min (1089 ml/min).

Figure 5.26 (a) (a-p) and Figure 5.26 (b) (a-p) show the velocity streamlines at τ= 0.1 to 1 for zone I and zone II respectively. In the first quarter of the period the indentation accelerates into the tube. At τ = 0.2, a distinct recirculation zone prevails upstream of the indentation and exists until τ = 0.6 because of the decelerating flow (Figure 5.26 (a)(b-j)). When the acceleration phase begins thereafter, the recirculation zone disappears upstream of the indentation (Figure 5.26 (a)(k-p)).

At some time between, τ = 0.2 and 0.25 (Figure 5.26 (b) b & c) separation occurs in the lee of the indentation and an eddy A appears. The resulting eddy grows in its size and strength with no reattachment point. As a result a region of flow reversal exists distal to eddy A near the wall region, downstream of the indentation.

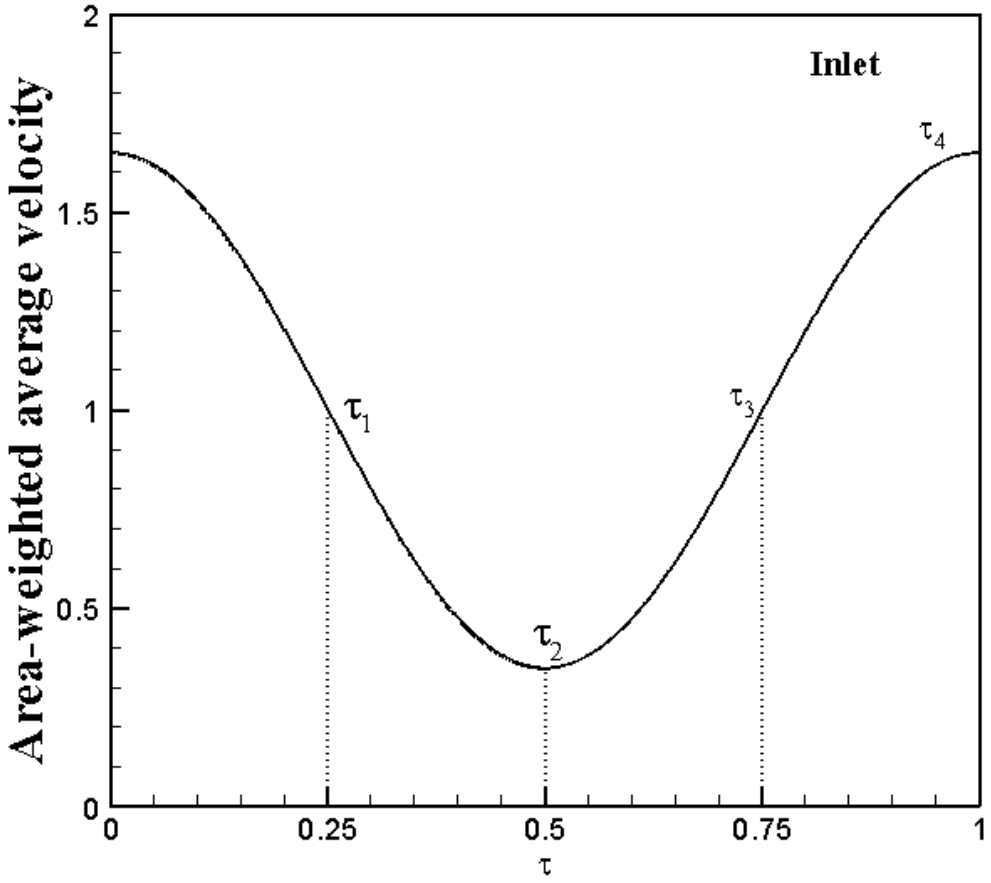

Figure 5.25 Flow input waveform at the Inlet for the pulsatile blood flow–Case IV (Re=200, α=13.4).

At $\tau = 0.4$ a second, eddy B of opposite sign forms near eddy A (Figure 5.26 (b) f) and the eddy A grows in its size and moves towards the core of the tube.

As the flow accelerates in third quarter of the cycle, the recirculation zone upstream of the indentation disappears. At $\tau = 0.5$, eddy A tries to split into a pair of co-rotating eddies, however it is weak and fails to double itself. Hence, the eddy doubling is not observed in this case (Figure 5.26 (b) h). As τ increases eddy A grows in its size and strength and moves towards the core of the tube. Also, the depth of the reversal flow region increases, with the time, downstream of the indentation, from the near wall region to the core of the tube.

At $\tau = 0.55$ (Figure 5.26 (b)i), the eddy A almost blocks the core flow in the tube. At $\tau = 0.65$ (Figure 5.26 (b)k), the reverse flow from the downstream of the indentation sweeps out eddy B. As the indentation recedes back to its original position ($\tau = 1$), the accelerating flow sweeps out the reversal flow downstream of the indentation (Figure 5.26 (b) r-II).

Figure 5.27 (a) and (b) show the variation of the wall shear stress on the upper (indented) wall at various time intervals during the cycle. They indicate the strength of the eddy; the position of separation and the position of reattachment (change of sign in wall shear stress) and thus the movement of eddies along the wall. Eddy doubling can be observed from these figures. The wall shear stress upstream of the indentation is dominated mostly by the forward flow but downstream of the indentation it is strongly

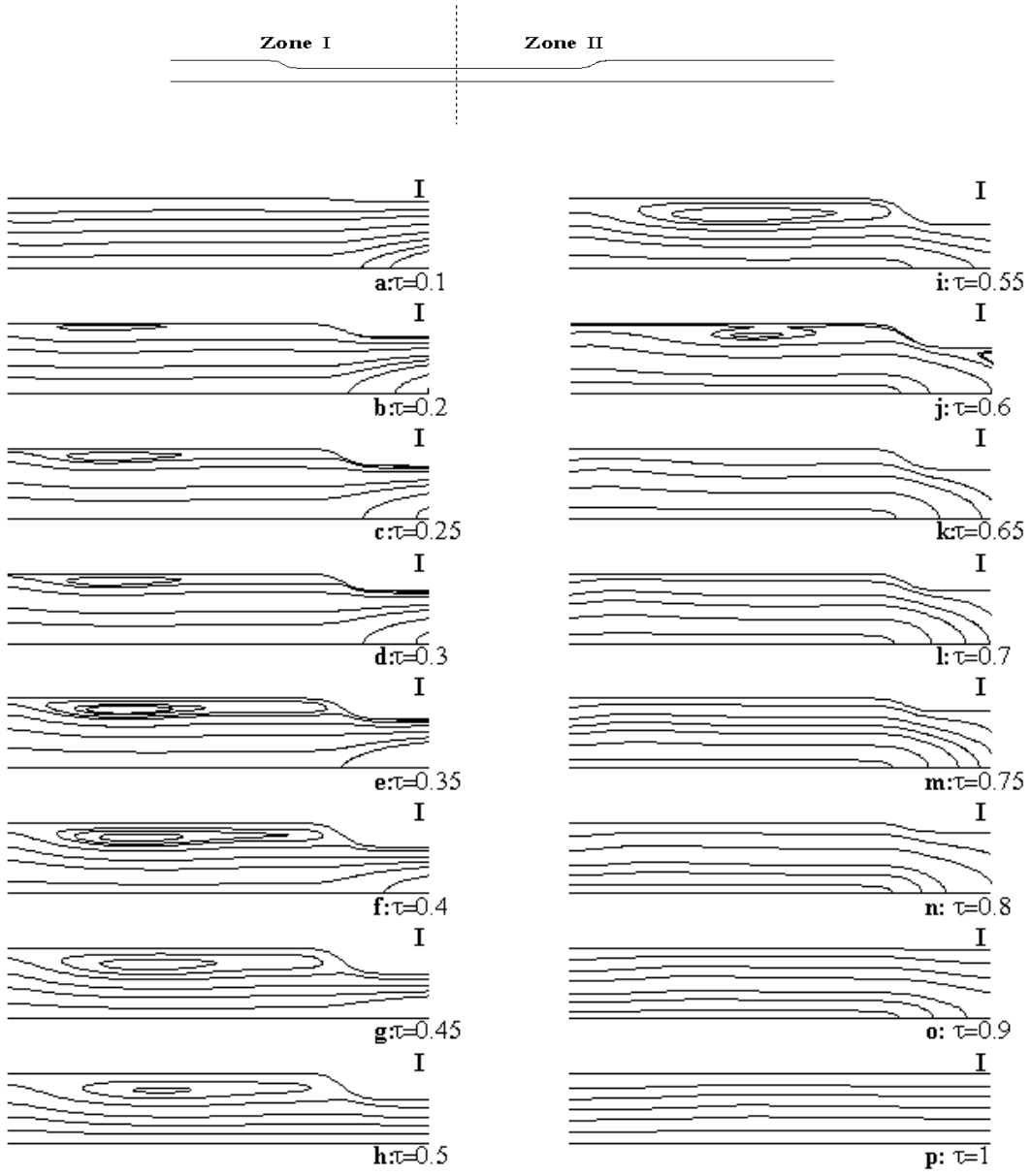

Figure 5.26 (a) Velocity Stream lines for Zone I at various times τ for Unsteady (Pulsatile) blood flow at the inlet-Case IV (Re=200, α=13.4).

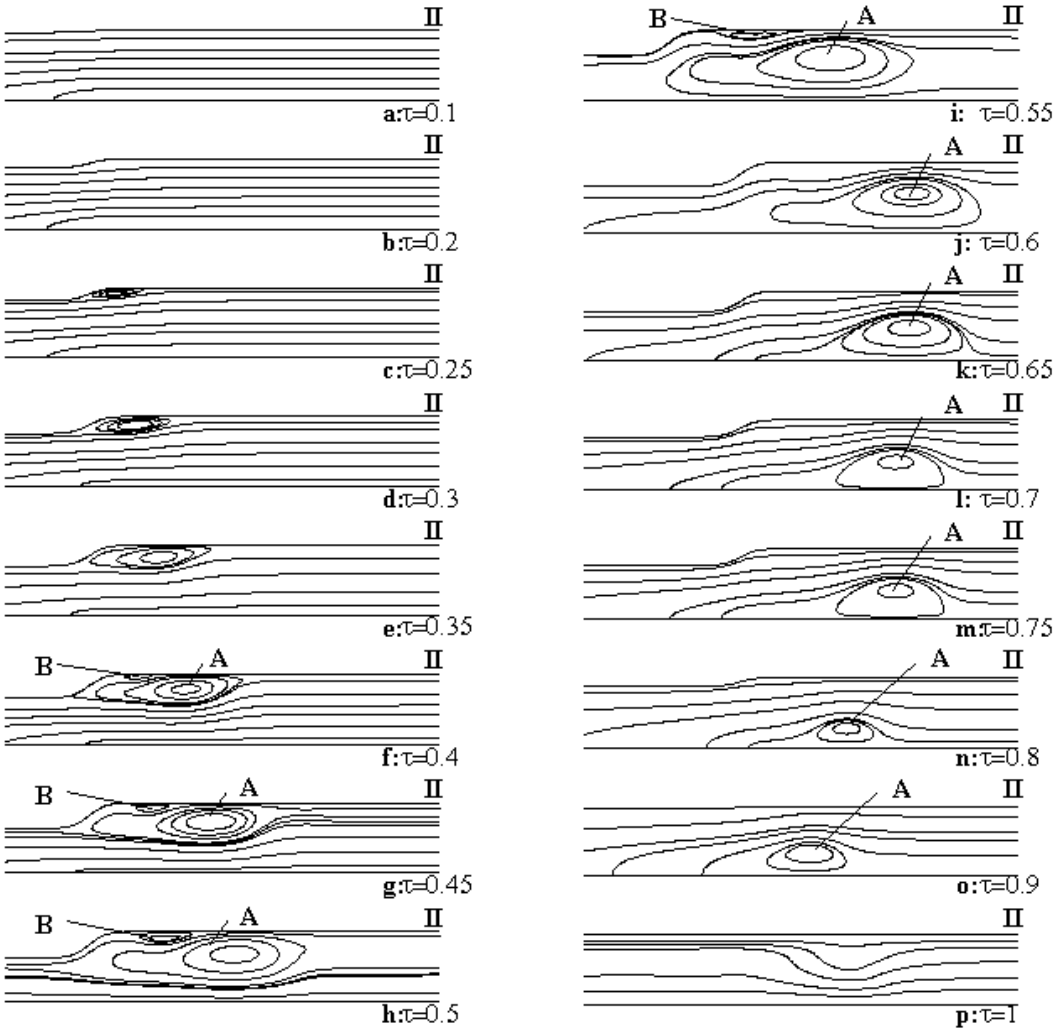

Figure 5.26 (b) Velocity Stream lines for Zone II at various times τ for Unsteady (Pulsatile) blood flow at the inlet-Case IV (Re=200, α=13.4).

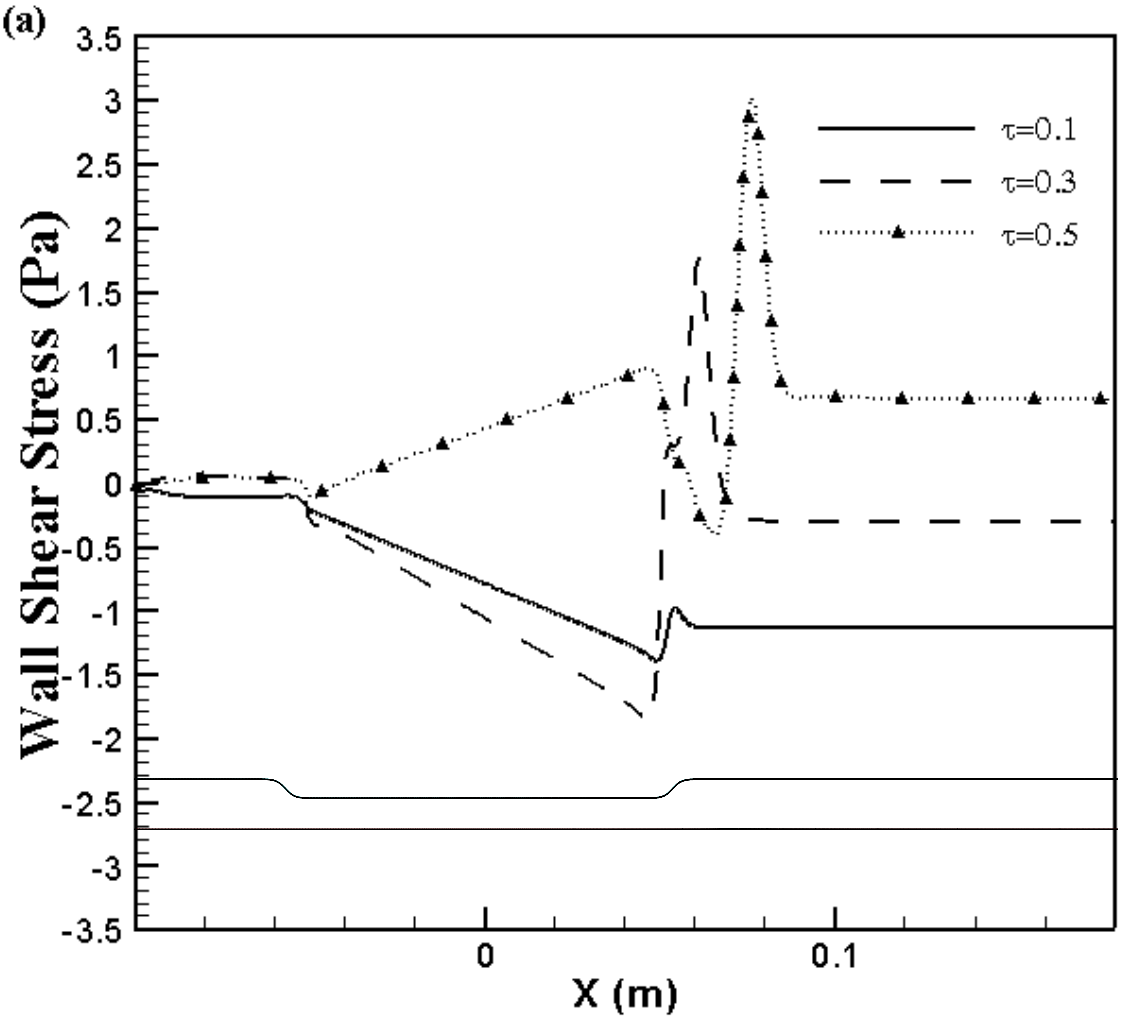

Figure 5.27 (a) Wall shear stress variations during one cycle along the indented wall, $\tau = 0.1 to 0.5$ for the pulsatile blood flow at the inlet-Case IV (Re=200,α=13.4).

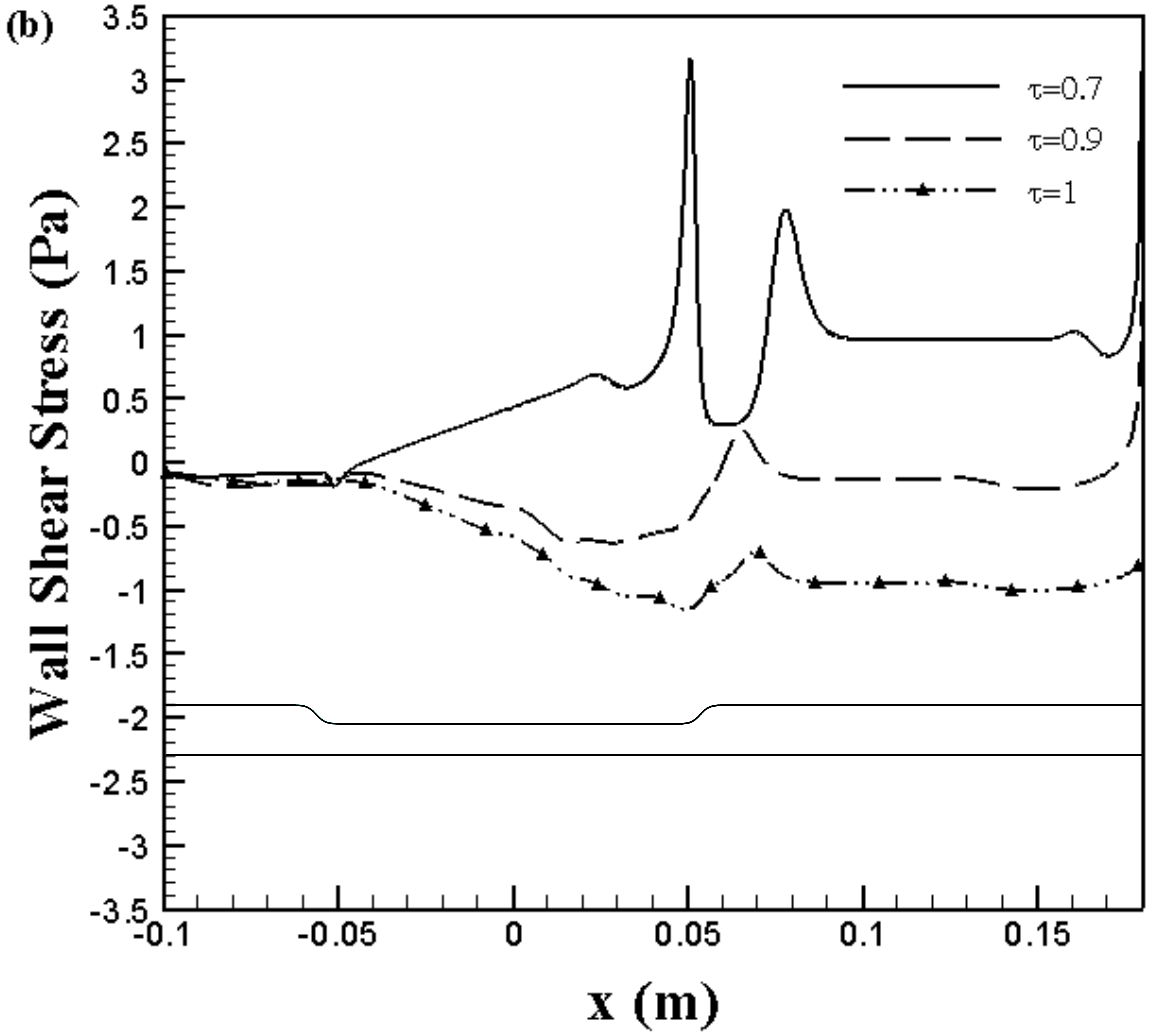

Figure 5.27 (b) Wall shear stress variations during one cycle along the indented wall, $\tau = 0.7 to 1$ for the pulsatile blood flow at the inlet-Case IV (Re=200,α=13.4).

affected by the eddies. The shear stress variation along the indentation also indicates an acceleration of the flow in this region when the indentation is moving inwards ($\tau<0.5$); and a deceleration when it is retracting ($\tau>0.5$).

Figure 5.28 shows the variation of pressure drop (P1-P2 and P1-P3) along the indentation, at the sections shown in Figure 5.13. For the first quarter of the cycle, the pressure drop increases with the time, while for the second quarter; the pressure drop decreases with time. As the indentation starts receding late in the cycle, the pressure drop increases with time showing a sinusoidal pattern. The pressure drop between the upstream of the indentation and downstream of the indentation (P1-P3) is greater than the pressure drop between the upstream of the indentation and center of the indentation (P1-P2). The pressure drop is high across the indentation, when we have maximum narrowing ($\tau=0.5$).

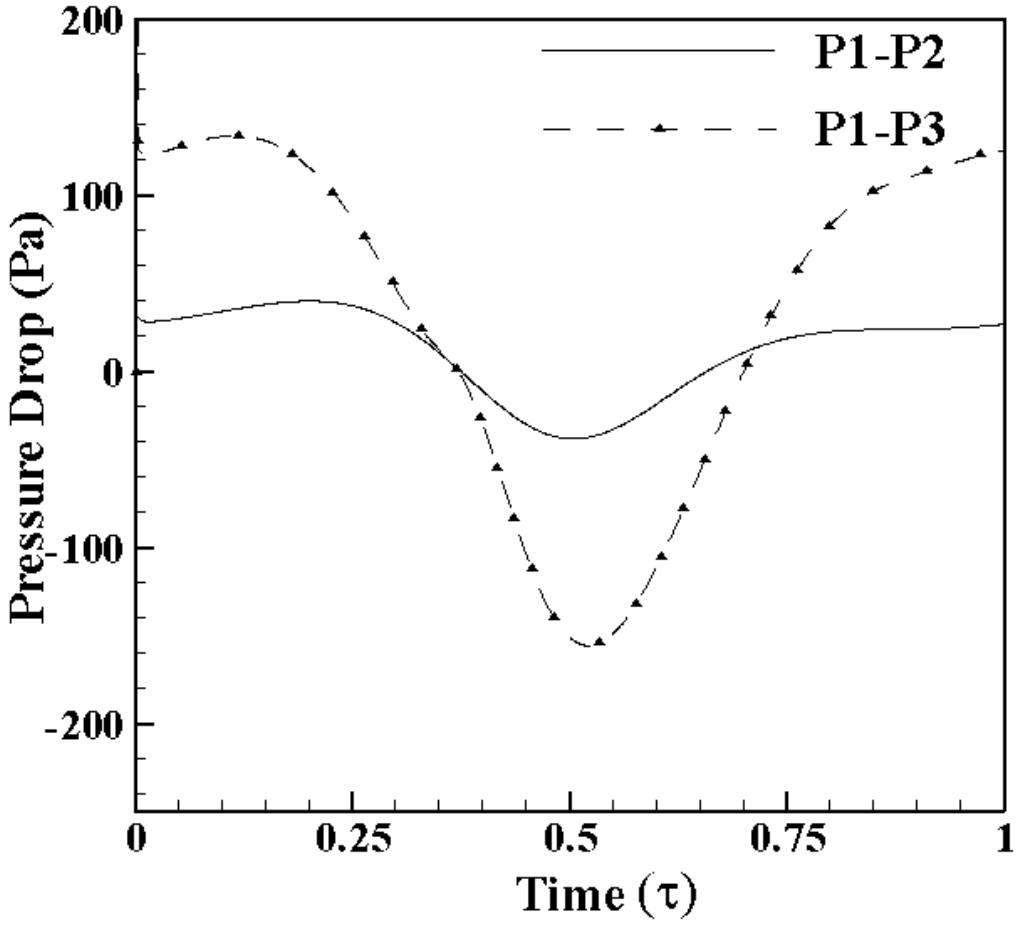

Figure 5.28 Pressure Drop along the indentation for pulsatile blood flow at the inlet-Case IV (Re=200, α=13.4).

5.2.6.1. Comparison of Pulsatile Blood and Steady Blood Flow

Figure 5.29 (a-d) shows the comparison of axial velocity profiles of pulsatile flow and steady flow at different cross sections and time intervals. For the pulsatile flow case a recirculation zone is observed upstream of the indentation between the time levels $\tau = 0.2$ and $\tau=0.65$ because of the decelerating flow in these time levels. The velocities are maximum for the both the cases after the indentation (6.5R). The velocity profiles also show the separation and recirculation zones. From the figure it can also be viewed that the reverse flow dominates at the downstream of the indentation as the τ increases.

The magnitude of the velocity profile for the pulsatile blood flow is less than steady blood flow at $\tau = 0.25$, due to deceleration phase of the pulsatile flow, while the pulsatile blood flow has high velocity magnitude at $\tau = 1$, due to acceleration phase of the pulsatile flow.

The main difference that exists between the pulsatile flow and steady flow is the reverse flow upstream of the indentation. Reverse flow was observed not observed in the case of steady flow while it was observed in the case of pulsatile flow.

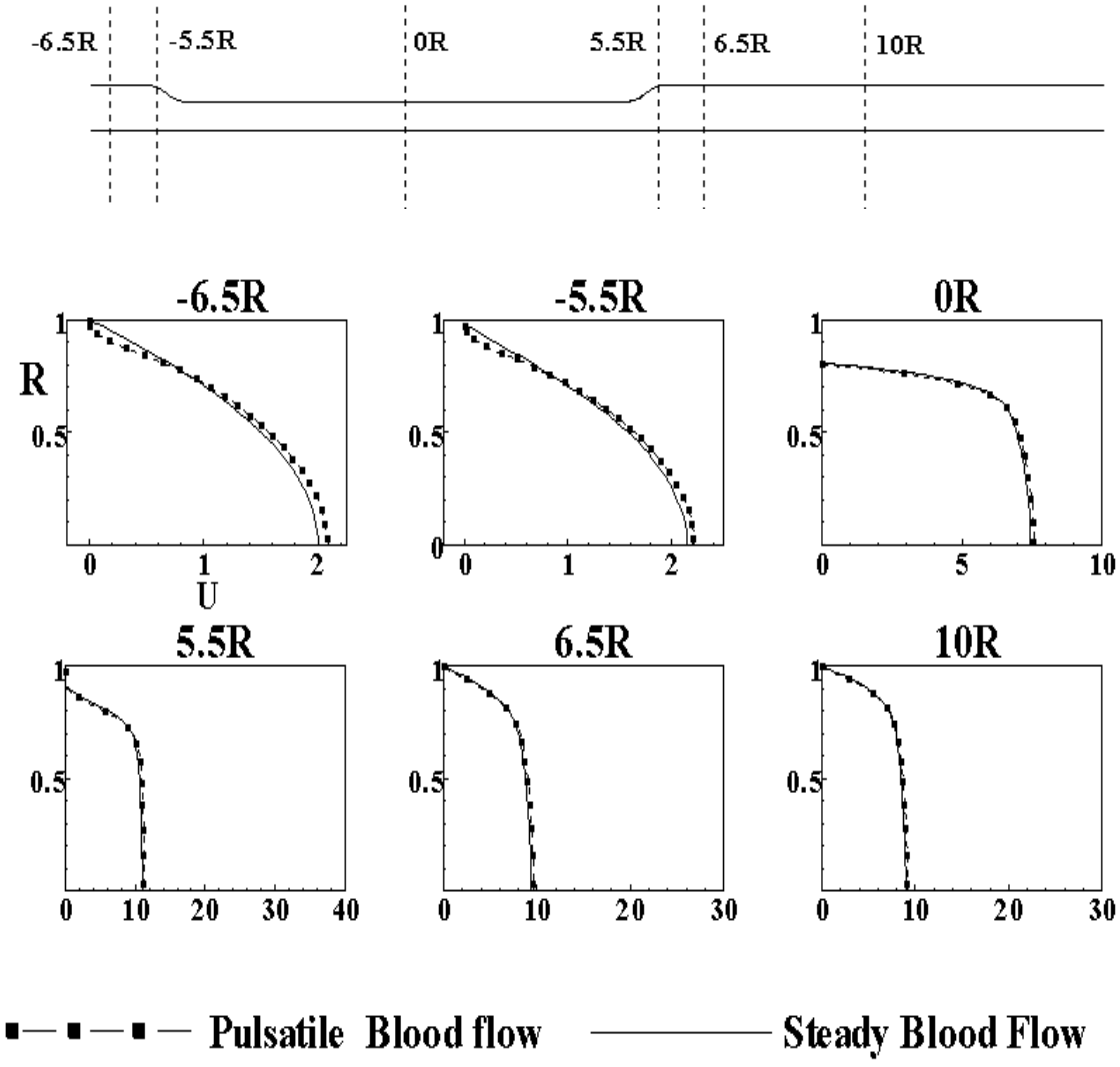

Figure 5.29 (a) Comparison of Axial Velocity profiles of steady and pulsatile blood flow for τ=0.25.

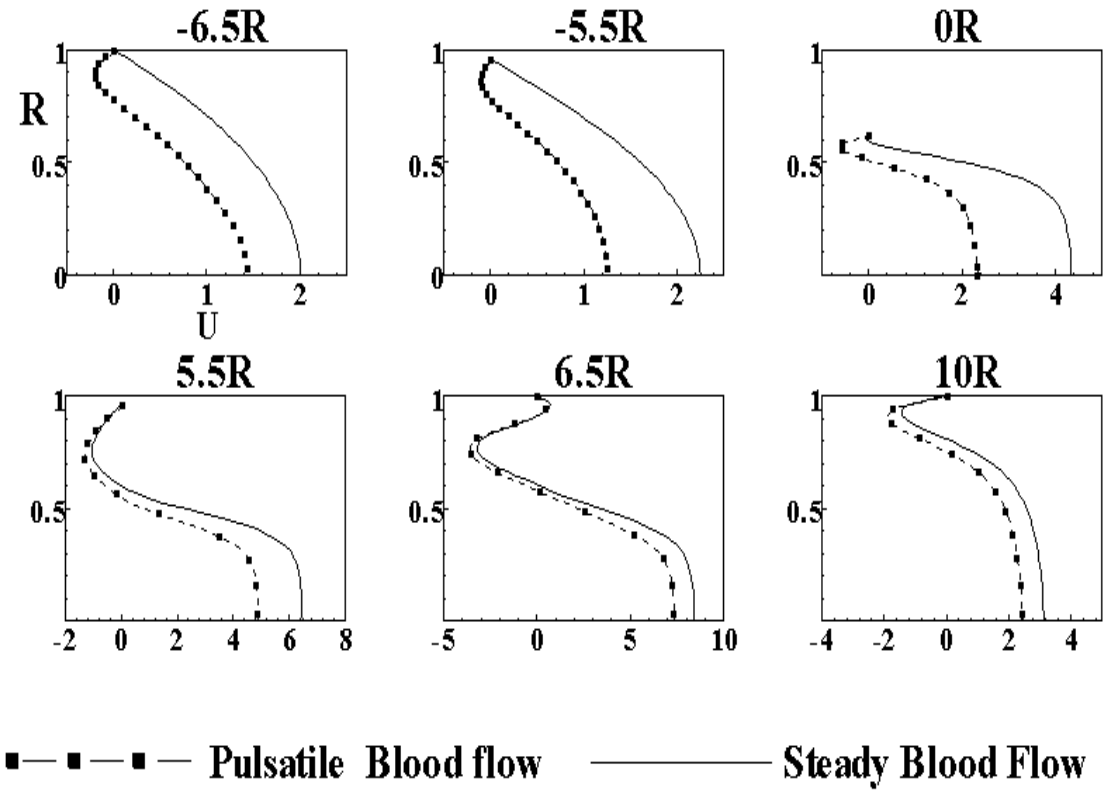

Figure 5.29 (b) Comparison of Axial Velocity profiles of steady and pulsatile blood flow for τ=0.5.

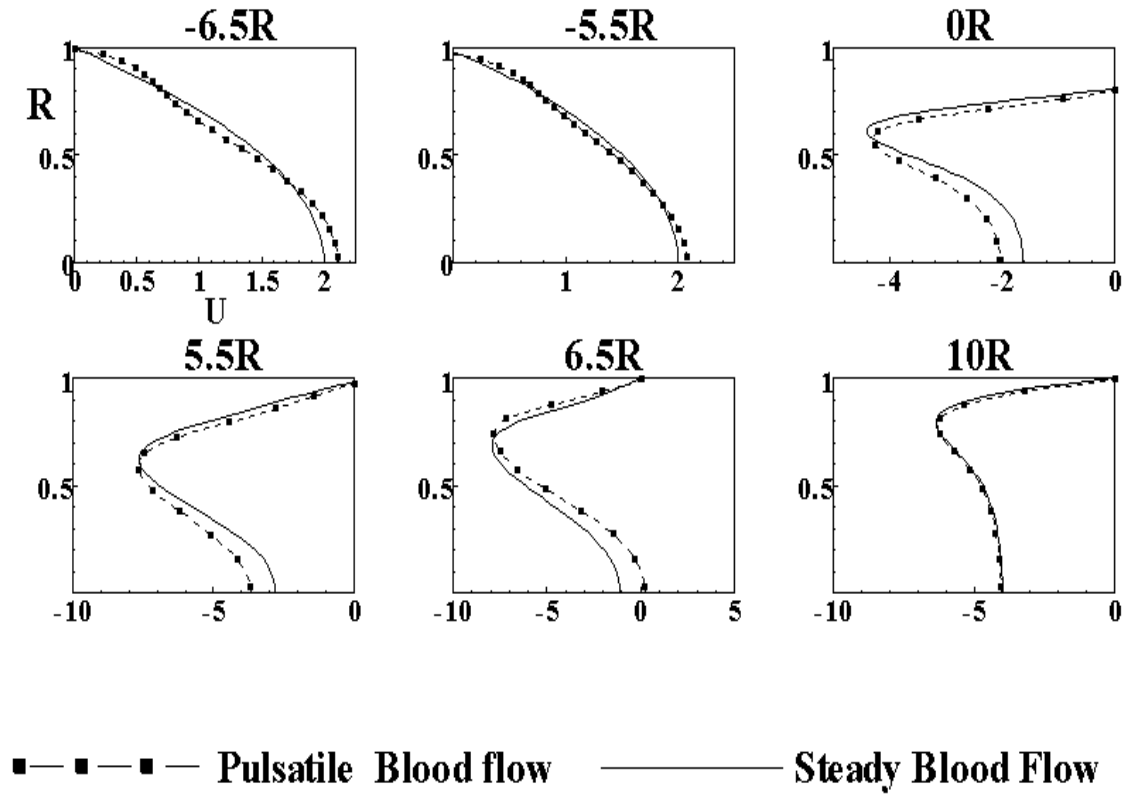

Figure 5.29 (c) Comparison of Axial Velocity profiles of steady and pulsatile blood flow for τ=0.75.

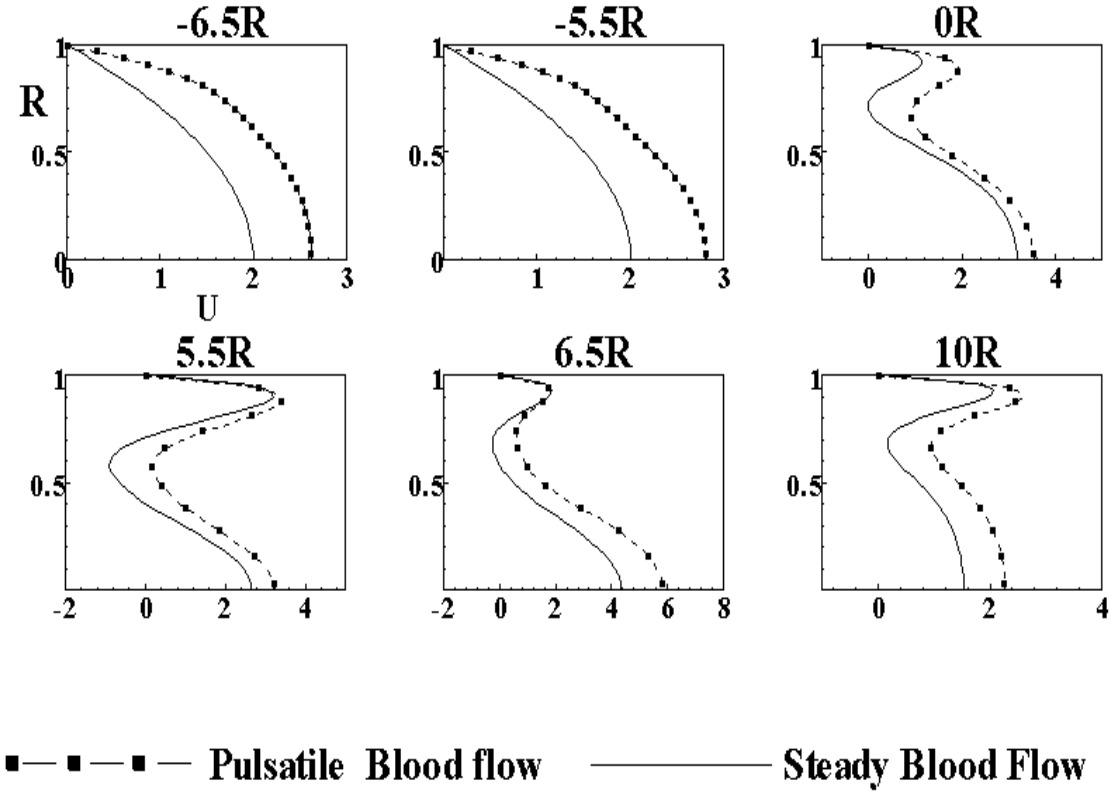

Figure 5.29 (d) Comparison of Axial Velocity profiles of steady and pulsatile blood flow for τ=1.

CHAPTER 6

AXISYMMETRIC FLOW OF A NON-NEWTONIAN FLUID IN A TUBE WITH A MOVING INDENTATION

In the present study, the non-Newtonian rheology of the flowing blood is characterized by non-Newtonian power law, Carreau Model and Carreau-Yasuda model, which were discussed in the chapter 3.

6.1. Case I-Non-Newtonian Power Law

In this case, the density of blood is taken as ρ=1060kg/m^3 and the non-Newtonian model is characterized by non-Newtonian power law. The frequency of the moving indentation was set at a value of 1Hz, representing the biological flows. The average velocity was chosen to give a Reynolds number Re=200. For this Re, the volumetric flow rate upstream of the moving indentation, Q_0 is 6.6X10^{-4}m^3/min (660 ml/min). The Womersley parameter for this case is, α=13.4.

Figure 6.1 (a-p) show the velocity streamlines at τ= 0.1 to 1. In the first quarter of the period, the indentation accelerates into the tube. At some time between, τ = 0.2 and

0.25 (Figure 6.1c-II) separation occurs in the lee of the indentation and an eddy A appears. The resulting eddy grows in its size and strength with no reattachment point. As a result a region of flow reversal exists distal to eddy A near the wall region, downstream of the indentation.

At $\tau = 0.45$ a second, eddy B of opposite sign forms near eddy A (Figure 6.1g-II) and the eddy A grows in its size and moves towards the core of the tube. At $\tau = 0.5$ (Figure 6.1h-II), eddy A tries to split into a pair of co-rotating eddies, but could not split because of high viscosity of the blood. As the indentation accelerates towards the wall of the tube, a suction effect is created by the indentation. Due to this suction effect, reversal flow is observed in the indentation and downstream of the indentation. At $\tau = 0.55$ (Figure 6.1 i-II), eddy A and B almost blocks the core flow and the thickness of the reversal flow region increases with the time downstream of the indentation, from the wall to the core of the tube. At $\tau = 0.65$ (Figure 6.1k-II), the reverse flow region downstream moves back into the indentation due to suction effect of the indentation and sweeps out the eddy B and eddy C. As the indentation recedes back to its original position, the reverse flow region at the downstream moves back into the indentation due to suction effect of the indentation and collides with the upstream coming flow. Hence, at $\tau = 1$ (Figure 6.1 p-II), the flow is fully disturbed in the indentation. Flow does not recover for the next cycle. It may take three or four more cycles to recover the flow or may not recover at all as long as you have a moving indentation.

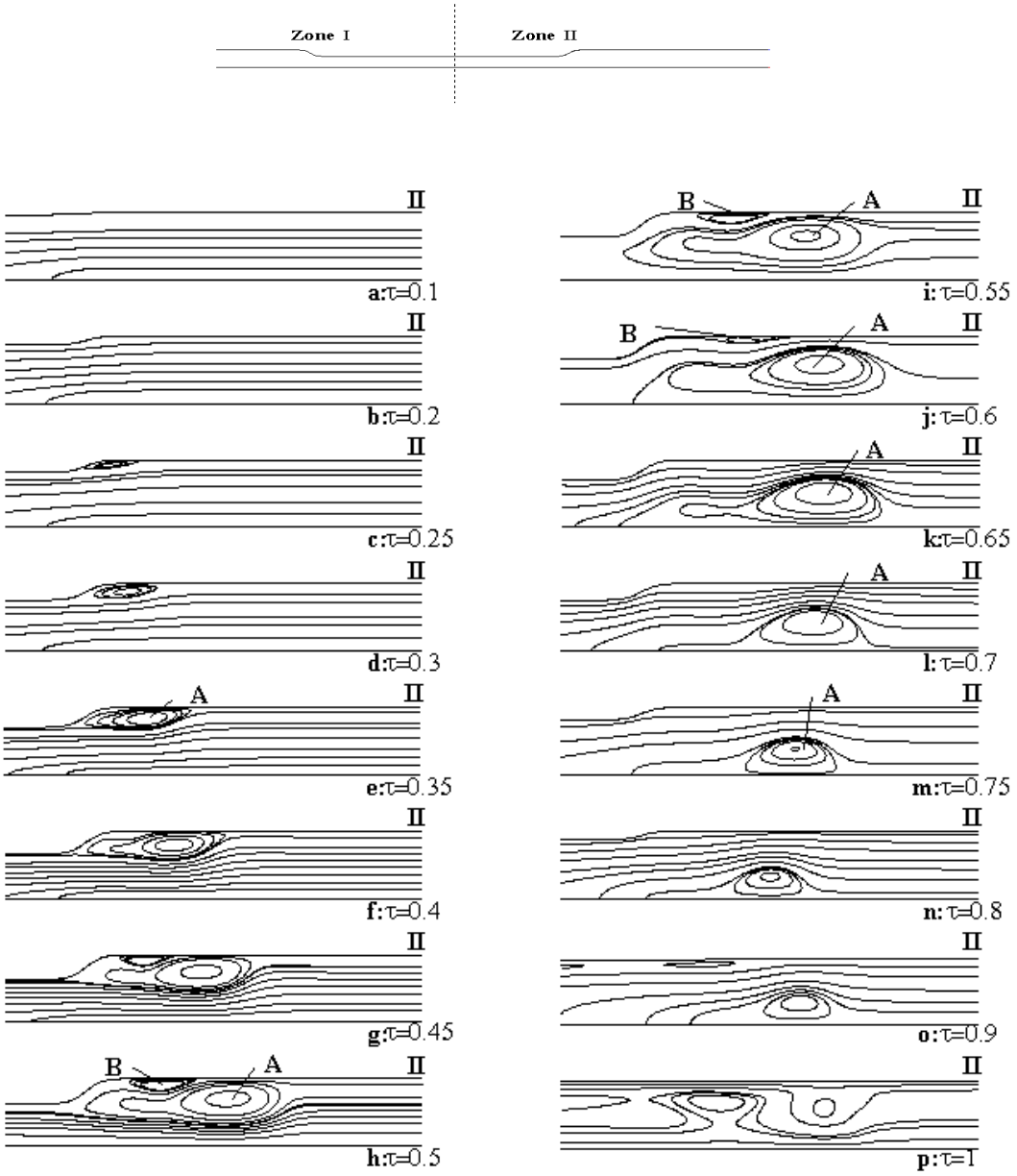

Figure 6.1 Velocity Stream lines at various times τ for steady non-Newtonian blood flow characterized by non-Newtonian power law (Re=200, α=13.4).

Figure 6.2 (a) and (b) show the variation of the wall shear stress on the upper (indented) wall at various time intervals during the cycle. They indicate the strength of the eddy; the position of separation and the position of reattachment (change of sign in wall shear stress) and thus the movement of eddy along the wall. The wall shear stress upstream of the indentation is dominated mostly by the forward flow but downstream of the indentation it is strongly affected by the eddies. The shear stress variation along the indentation also indicates an acceleration of the flow in this region when the indentation is moving inwards ($\tau<0.5$) and a deceleration when it is retracting ($\tau>0.5$). High wall shear stresses are observed just downstream of the indentation. The vortex forming downstream of the indentation gives high velocity gradients, which results in high wall shear stress.

Figure 6.3 shows the variation of pressure drop (P1-P2 and P1-P3) with the time along the indentation, at the sections shown in Figure 5.13. For the first quarter of the cycle, the pressure drop increases with the time, while for the second quarter; the pressure drop decreases with time. As the indentation starts receding late in the cycle, the pressure drop increases with time showing a Sinusoidal pattern. The pressure drop P1-P3 is greater than the pressure drop P1-P2. The maximum pressure drop across the stenosis occurs when we have the maximum narrowing ($\tau\approx0.5$).

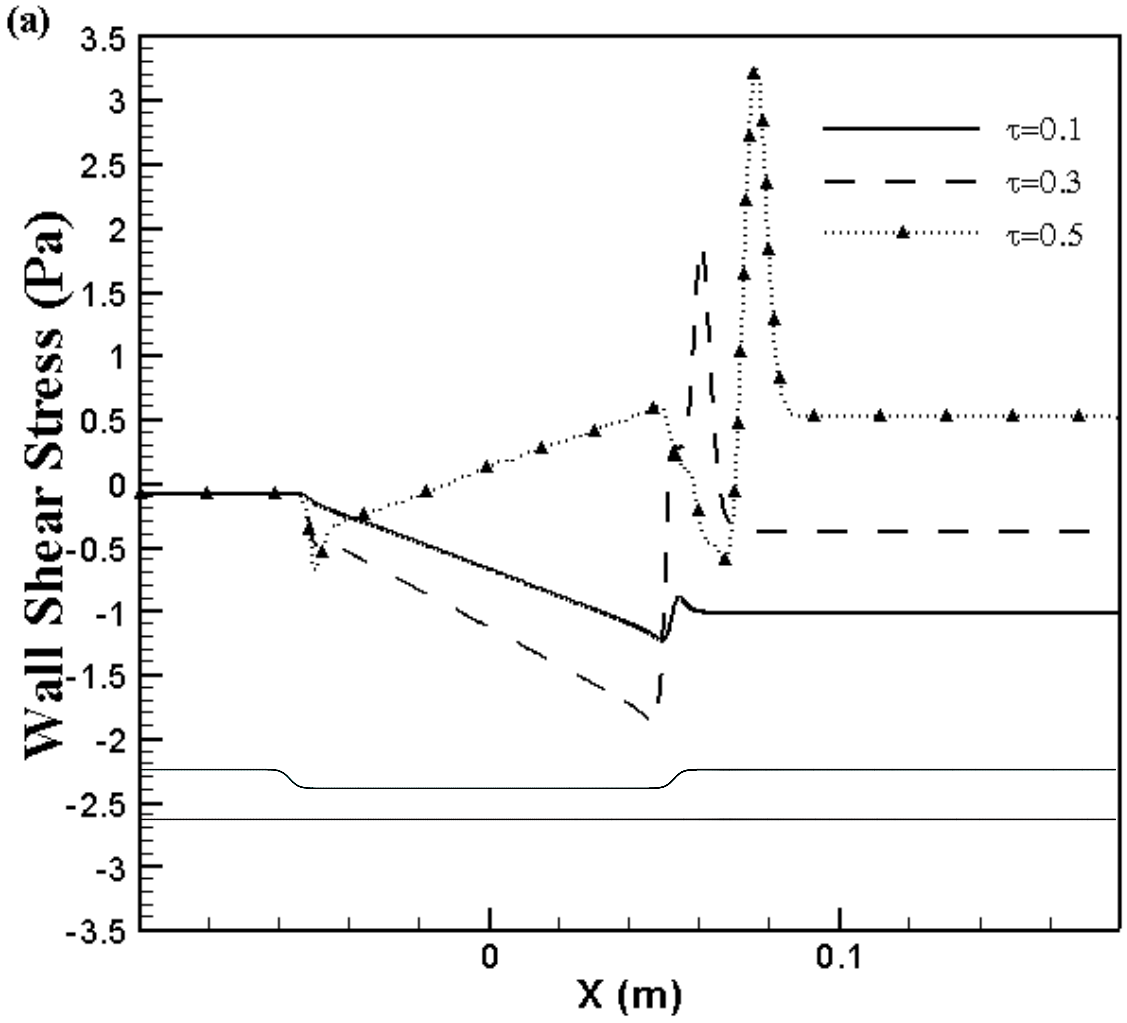

Figure 6.2 (a) Wall shear stress variations during one cycle along the indented wall, τ=0.1 to 0.5 for steady non-Newtonian blood flow characterized by non-Newtonian power law-Case I (Re=200, α=13.4).

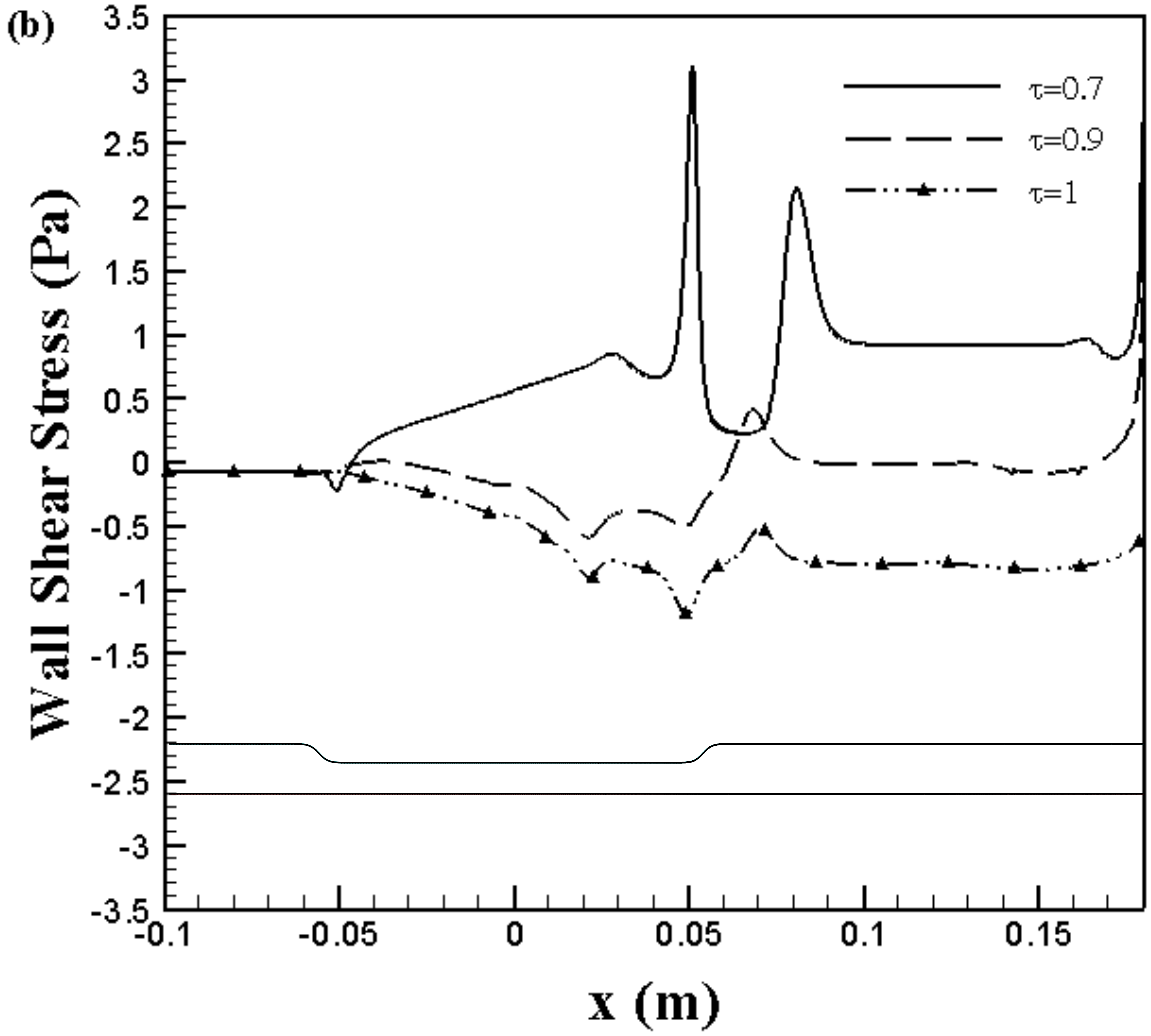

Figure 6.2 (b) Wall shear stress variations during one cycle along the indented wall, τ=0.7 to 1for steady non-Newtonian blood flow characterized by non-Newtonian power law -Case I (Re=200, α=13.4).

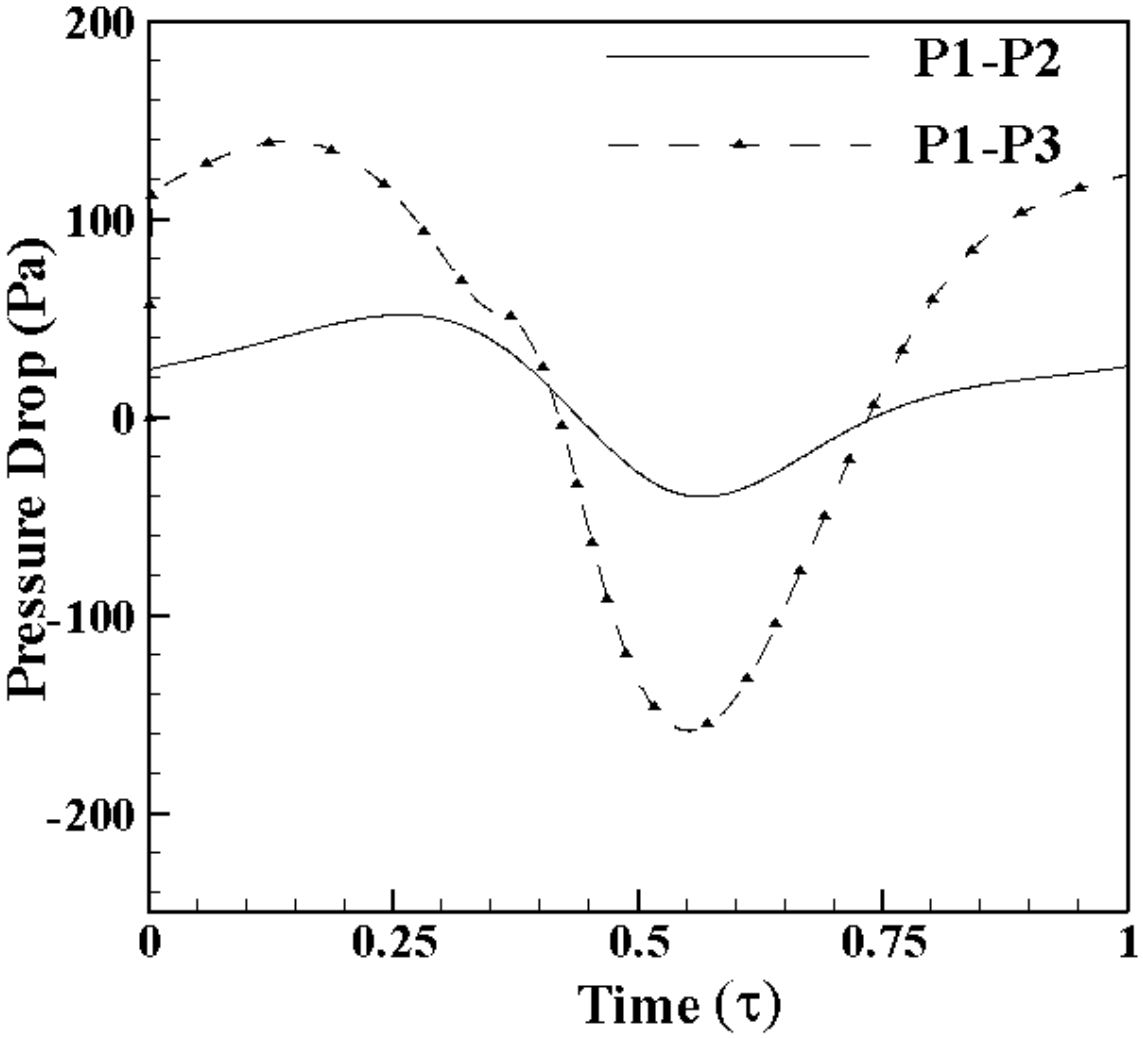

Figure 6.3 Pressure drop along the indentation for steady blood flow characterized by non-Newtonian power law at the inlet -Case I (Re=200, α=13.4).

Figure 6.4 shows the variation of axial velocity with the time along the indentation at points of interest (Figure 5-13). The straight line (at X=-6.5R) in the Figure 6.4, indicates that the flow is not affected upstream of the indentation. At the centre (X=0R) and downstream (X=6.5R) of the indentation, the axial velocity increases sinusoidally with time for the first quarter of the cycle as the indentation is accelerating into the tube. Between the second and the third quarter of the cycle the axial velocity decreases with time. And in the final quarter of the cycle, the axial velocity increases with time. The axial velocity is high downstream (X=6.5R) of the indentation in compare with that of centre of the indentation due to upcoming forward flow.

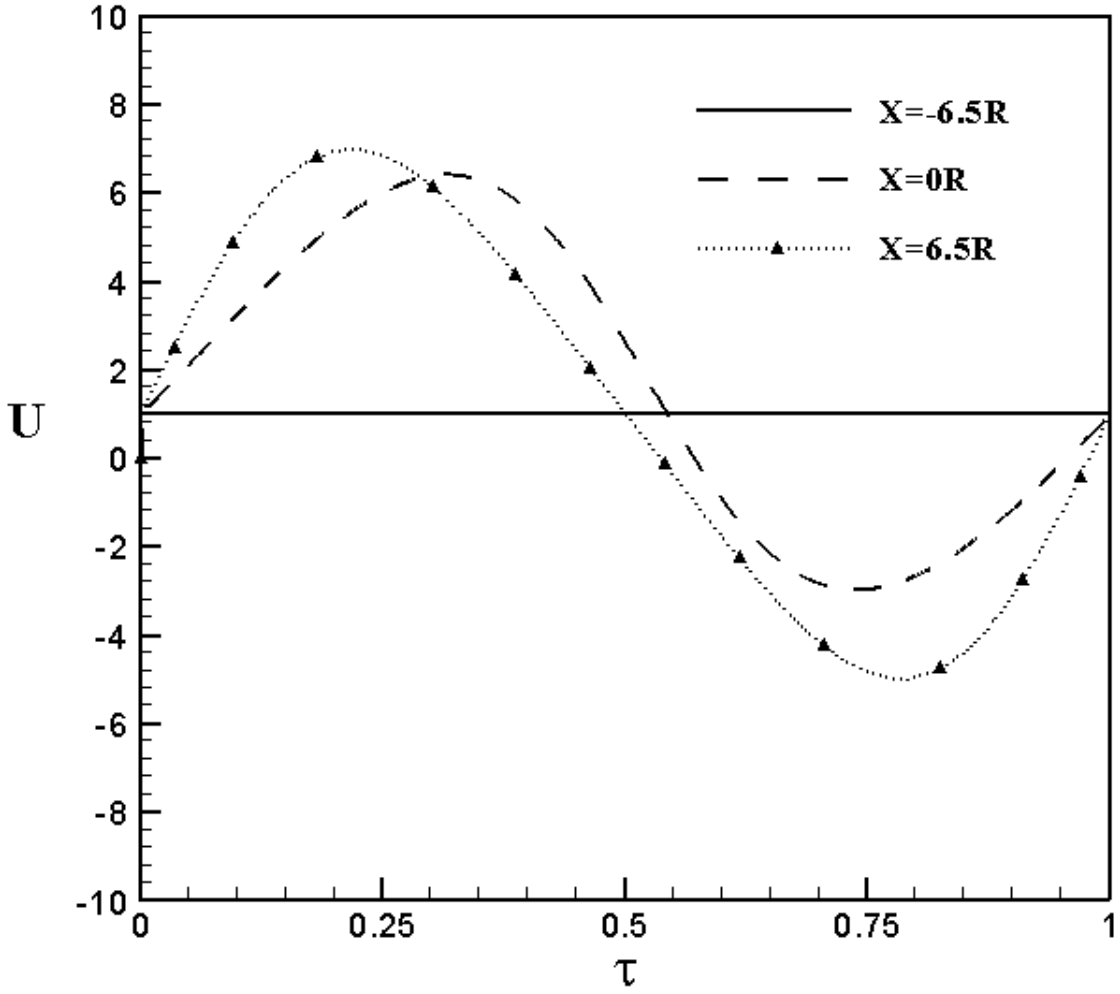

Figure 6.4 Variation of axial velocity with time at different sections of the tube -Case I (Re=200, α=13.4).

6.2. Case II-Carreau Model

Here, the non-Newtonian property of blood is characterized by the Carreau Model. Figure 6.5(a-p) show the velocity streamlines at τ= 0.1 to 1. In the first quarter of the period the indentation accelerates into the tube. At some time between, τ = 0.2 and 0.25 (Figure 6.5b-I & II) separation occurs in the lee of the indentation and an eddy A appears. The resulting eddy grows in its size and strength with no reattachment point. As a result a region of flow reversal exists distal to eddy A, near the wall region, downstream of the indentation.

At τ = 0.45 a second, eddy B of opposite sign forms near eddy A (Figure 6.5g-II) and the eddy A grows in its size and moves towards the axis of the tube. At τ = 0.5 (Figure 6.5h-II), eddy A tries to split into a pair of co-rotating eddies, but could not split because of high viscosity of the blood. As the indentation accelerates towards the wall of the tube, a suction effect is created by the indentation. Due to this suction effect, reversal flow is observed in the indentation and downstream of the indentation. At τ = 0.55 (Figure 6.5i-II), eddy A and B almost blocks the core flow and the thickness of the reversal flow region increases, downstream of the indentation. At τ = 0.65 (Figure 6.5k-II), the reverse flow region downstream moves back into the indentation due to suction effect of the indentation and sweeps out eddy B and eddy C. As the indentation recedes back to its original position, the reverse flow region at the downstream moves back into the indentation due to suction effect of the indentation and collides with the upstream coming flow. Hence, at τ = 1 (Figure 6.5p-II) the flow is fully disturbed in the indentation.Flow does not recover for the next cycle. It may take three or four more cycles to recover the flow or may not recover at all as long as you have a moving indentation.

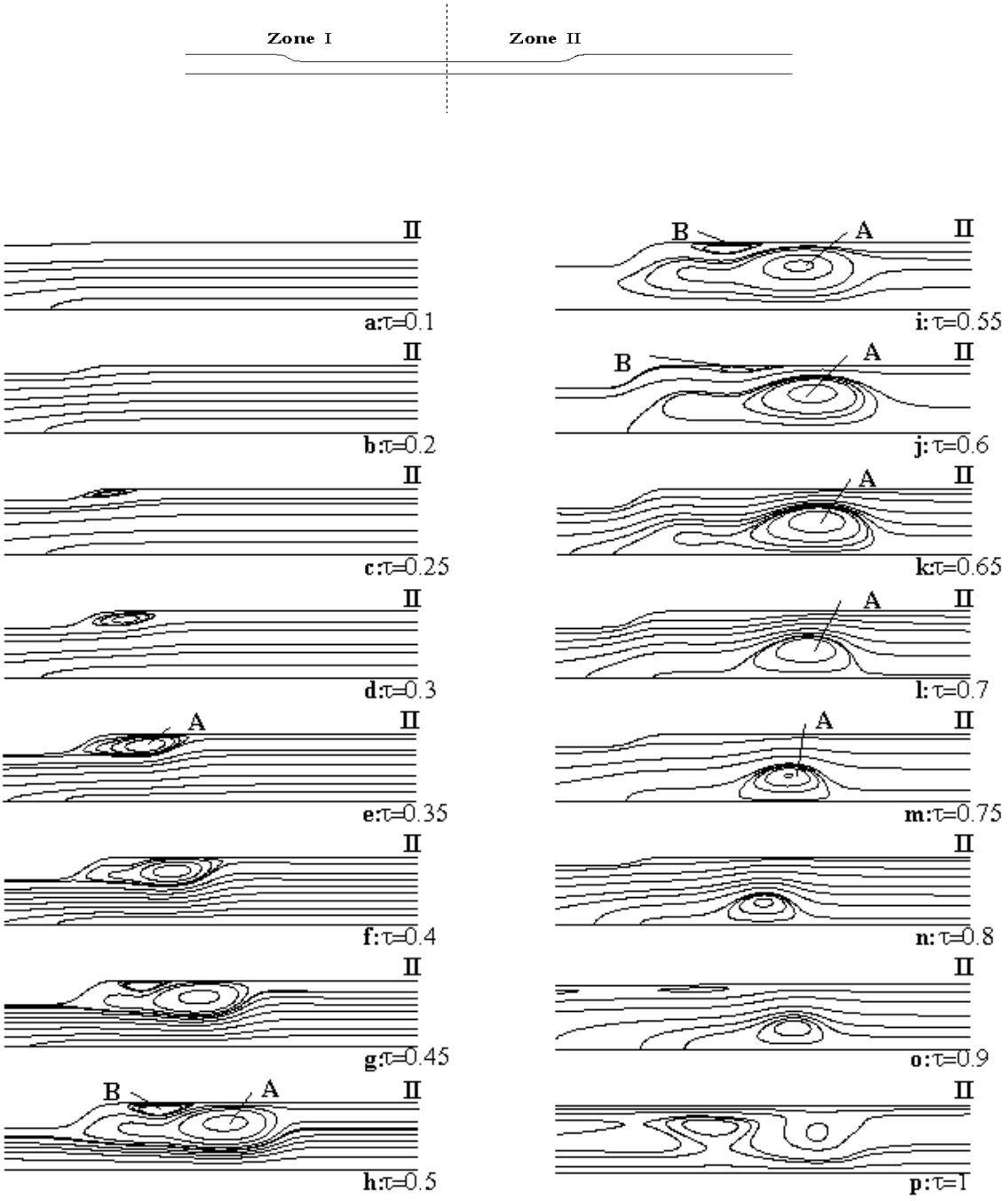

Figure 6.5 Velocity Streamlines at various times τ for steady blood flow characterized by Carreau model at the inlet-Case II (Re=200, α=13.4)

Figure 6.6 (a) and (b) show the variation of the wall shear stress on the upper (indented) wall at various time intervals during the cycle. They indicate the strength of the eddy; the position of separation and the position of reattachment (change of sign in wall shear stress) and thus the movement of eddy along the wall. The wall shear stress upstream of the indentation is dominated mostly by the forward flow but downstream of the indentation it is strongly affected by the eddies. The shear stress variation along the indentation also indicates an acceleration of the flow in this region when the indentation is moving inwards ($\tau<0.5$) and a deceleration when it is retracting ($\tau>0.5$). High wall shear stresses are observed just downstream of the indentation. The vortex forming downstream of the indentation gives high velocity gradients, which results in high wall shear stress.

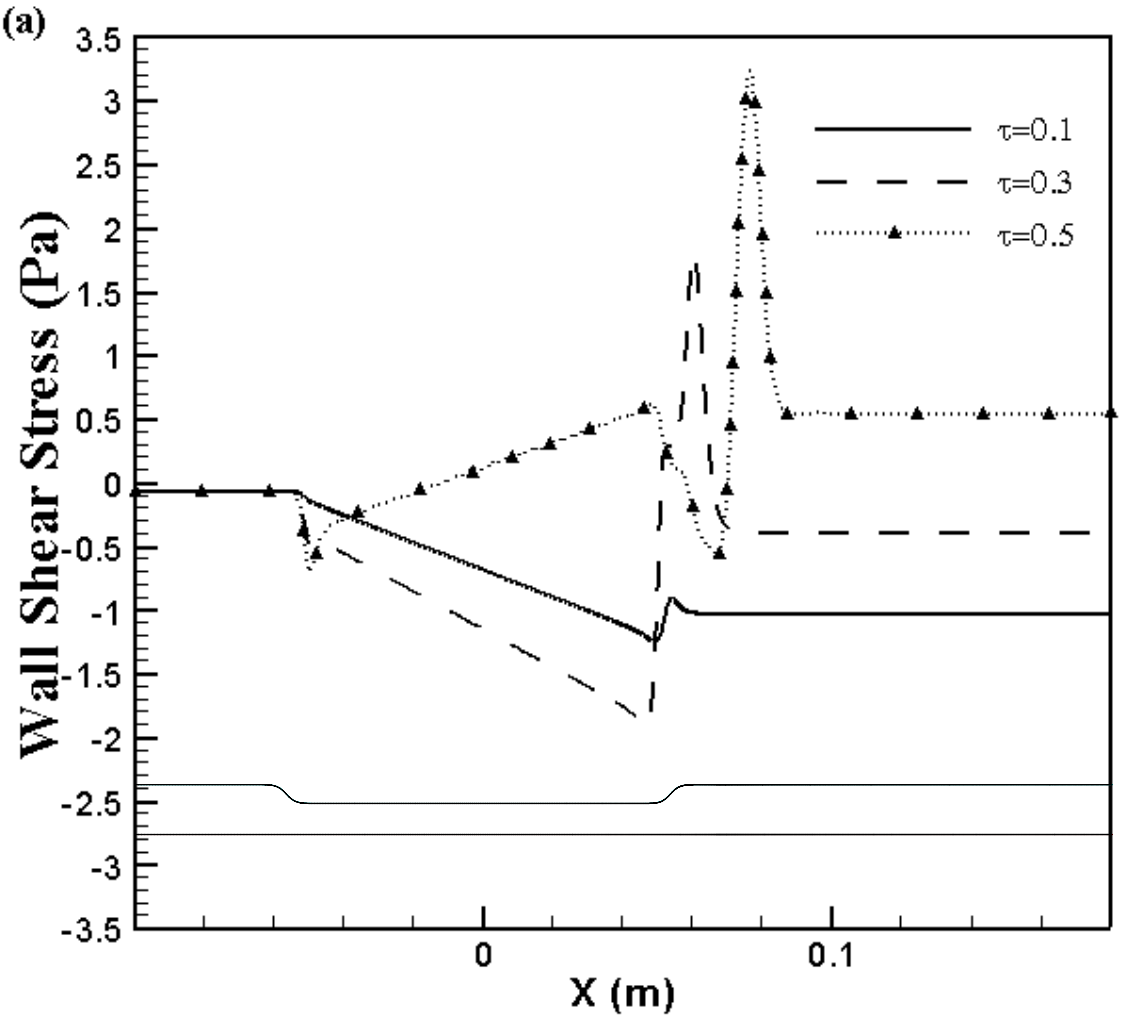

Figure 6.6 (a) Wall shear stress variations during one cycle along the indented wall $\tau = 0.1 to 0.5$ for the steady blood flow characterized by the carreau model-Case II (Re=200, α=13.4)

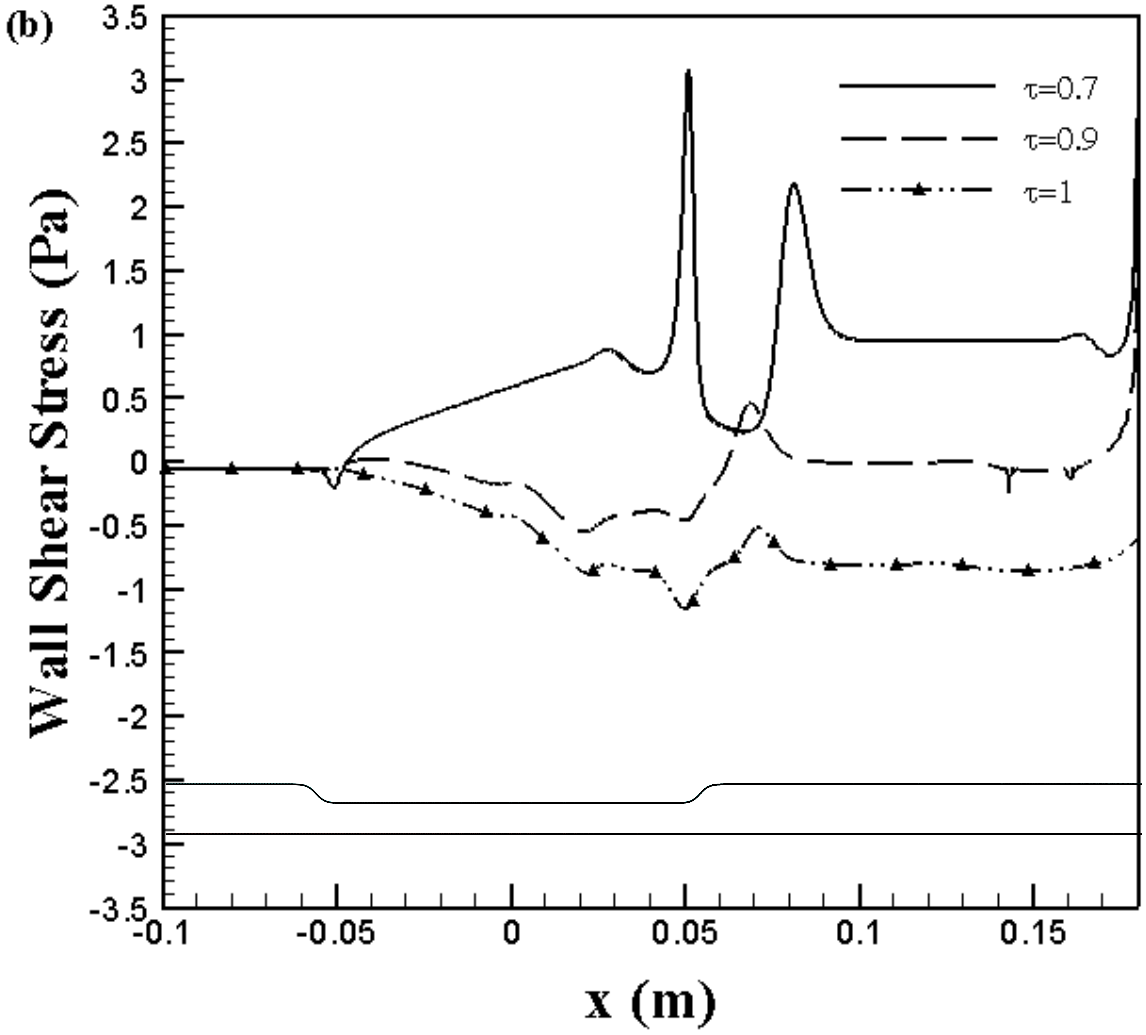

Figure 6.6 (b) Wall shear stress variations during one cycle along the indented wall τ=0.7 to 1 for the steady blood flow characterized by the carreau model-Case II (Re=200, α=13.4)

Figure 6.7 shows the variation of pressure drop (P1-P2 and P1-P3) with the time along the indentation at the sections shown in Figure 5.13. For the first quarter of the cycle, the pressure drop increases with the time, while for the second quarter; the pressure drop decreases with time. As the indentation starts receding late in the cycle, the pressure drop increases with time showing a Sinusoidal pattern. The pressure drop P1-P3 is greater than the pressure drop P1-P2. The maximum pressure drop across the stenosis occurs when we have the maximum narrowing ($\tau \approx 0.5$).

Figure 6.8 shows the variation of axial velocity with the time along the indentation at points of interest (Figure 5-13). The straight line (at X=-6.5R) in the Figure 6.8, indicates that the flow is not affected upstream of the indentation. At the centre (X=0R) and downstream (X=6.5R) of the indentation, the axial velocity increases sinusoidally with time for the first quarter of the cycle as the indentation is accelerating into the tube. Between the second and the third quarter of the cycle the axial velocity decreases with time. And in the final quarter of the cycle, the axial velocity increases with time. The axial velocity is high downstream (X=6.5R) of the indentation in compare with that of centre of the indentation due to upcoming forward flow.

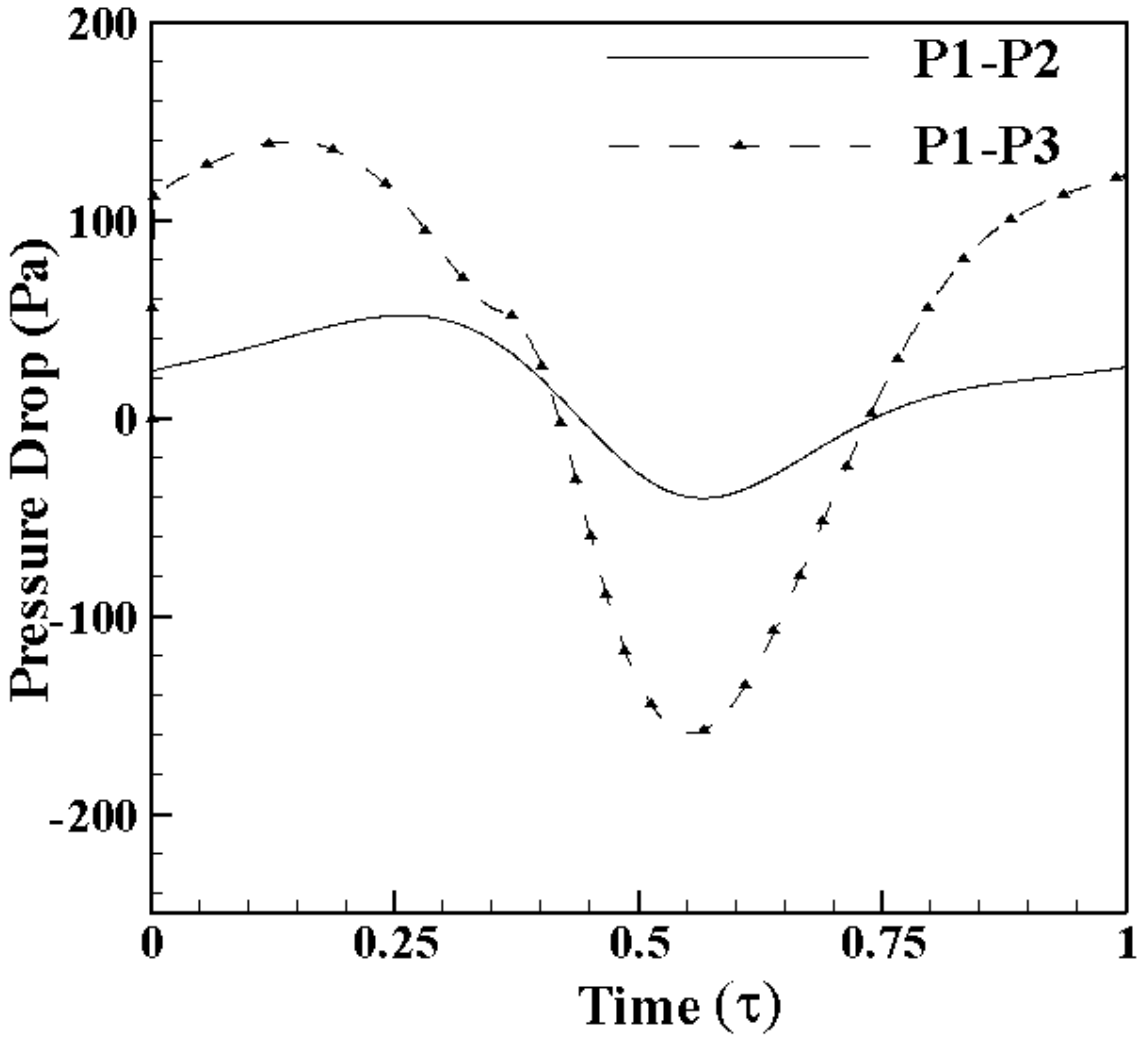

Figure 6.7 Pressure Drop along the indentation for steady blood flow characterized by the Carreau model at the inlet-Case II (Re=200, α=13.4)

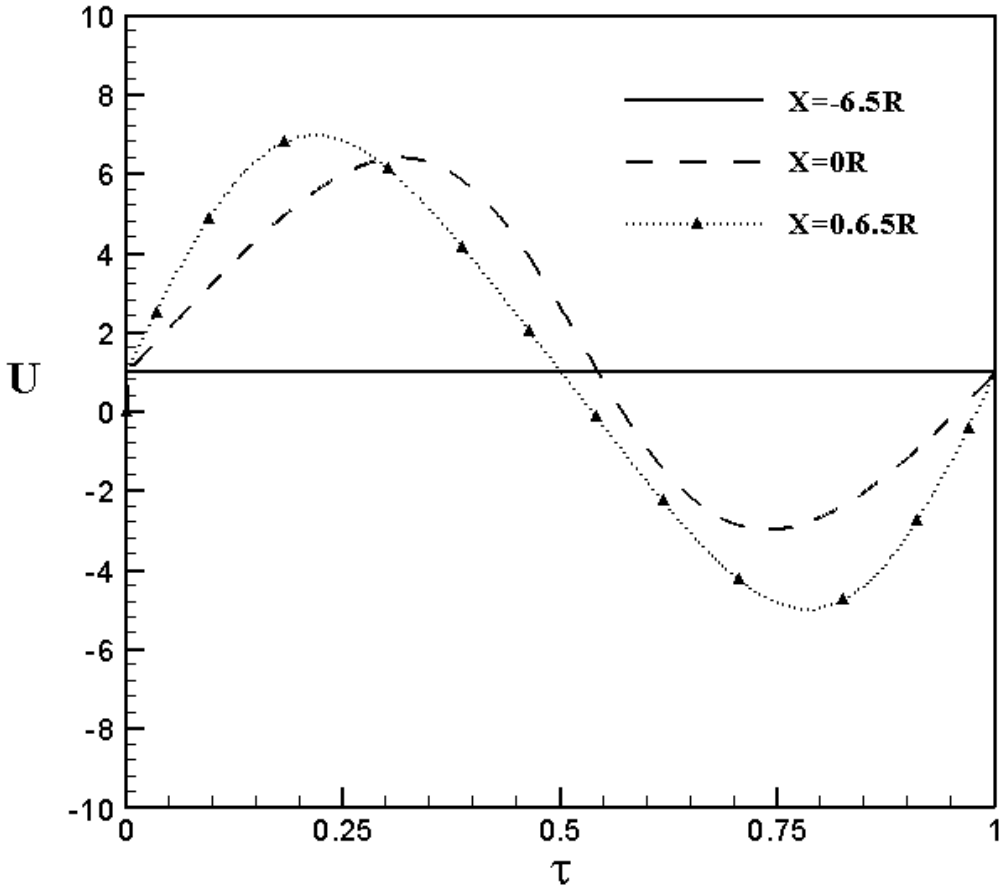

Figure 6.8 Variation of axial velocity with time at different sections of the indentation (Figure 5-13) for steady non-Newtonian blood flow characterized by Carreau Model at the inlet-Case II (Re=200, α=13.4)

6.3. Case III-Carreau-Yasuda Model

In this case, the non-Newtonian property of blood is characterized by the Carreau-Yasuda model. Figure 6.9(a-p) show the velocity streamlines at τ= 0.1 to 1. In the first quarter of the period, the indentation accelerates into the tube. At some time between, τ = 0.2 and 0.25 (Figure 6.9 b-II & c-II) separation occurs in the lee of the indentation and an eddy A appears. The resulting eddy grows in its size and strength with no reattachment point. As a result a region of flow reversal exists distal to eddy A, near the wall region, downstream of the indentation.

At τ = 0.45 a second, eddy B of opposite sign forms near eddy A (Figure 6.9g-II) and the eddy A grows in its size and moves towards the axis of the tube. At τ = 0.5 (Figure 6.9h-II), eddy A tries to split into a pair of co-rotating eddies, but could not split because of high viscosity of the blood. As the indentation accelerates towards the wall of the tube, a suction effect is created by the indentation. Due to this suction effect, reversal flow is observed in the indentation and downstream of the indentation. At τ = 0.55 (Figure 6.9i-II), eddy A and B almost blocks the core flow and the thickness of the reversal flow region increases, downstream of the indentation. At τ = 0.65 (Figure 6.9 k-II), the reverse flow region downstream moves back into the indentation due to suction effect of the indentation and sweeps out eddy B and eddy C. As the indentation recedes back to its original position, the reverse flow region downstream moves back into the indentation due to suction effect of the indentation and collides with the upstream coming flow. Hence, at τ = 1 (Figure 6.9p-II), the flow is fully disturbed in the indentation.

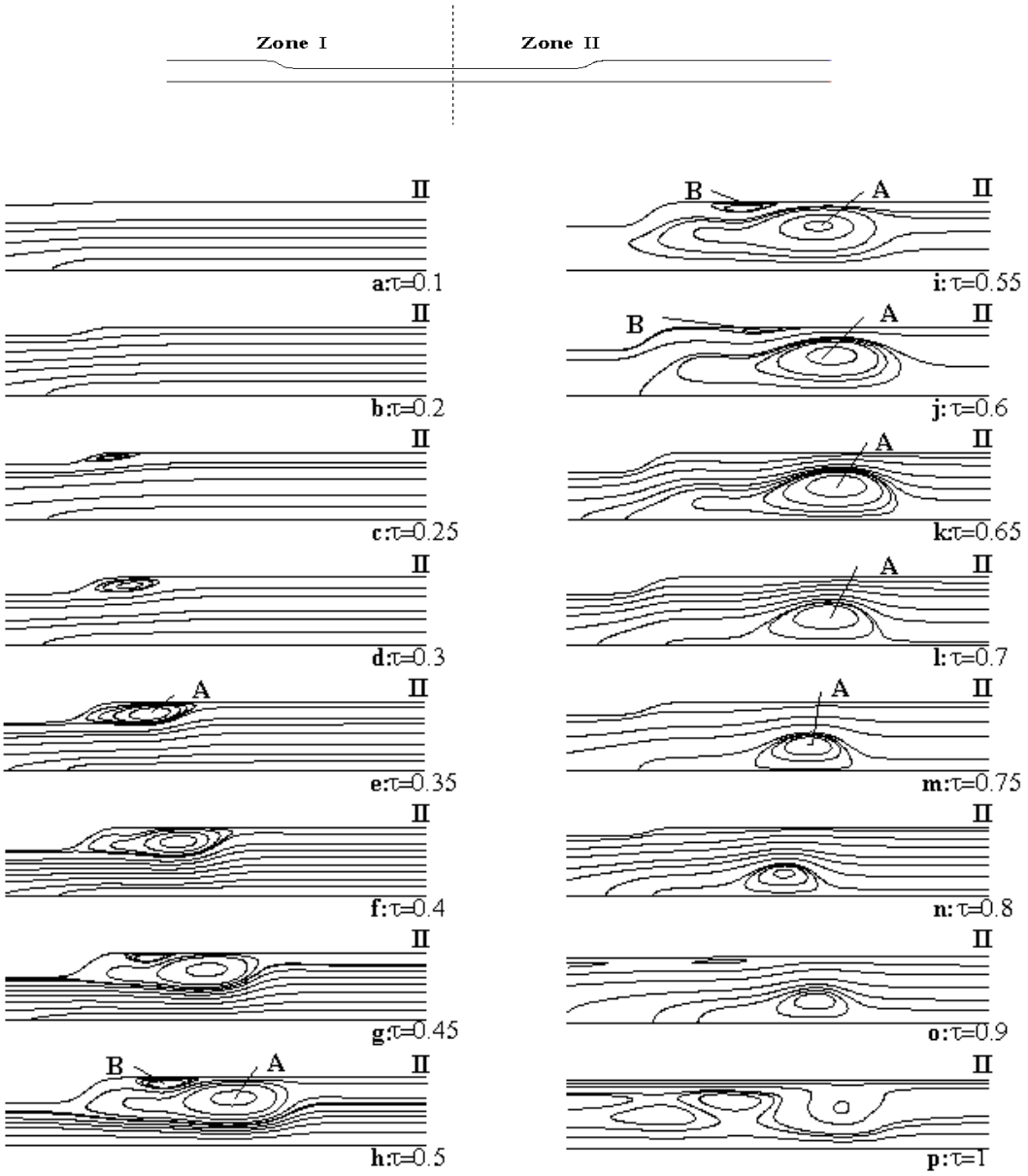

Figure 6.9 Velocity Stream lines at various times τ for steady non-Newtonian blood flow characterized by Carreau-Yasuda Model -Case III (Re=200, α=13.4)

Flow does not recover for the next cycle. It may take three or four more cycles to recover the flow or may not recover at all as long as you have a moving indentation.

Figure 6.10 (a) and (b) show the variation of the wall shear stress on the upper (indented) wall at various time intervals during the cycle. They indicate the strength of the eddy; the position of separation and the position of reattachment (change of sign in wall shear stress) and thus the movement of eddy along the wall. The wall shear stress upstream of the indentation is dominated mostly by the forward flow but downstream of the indentation it is strongly affected by the eddies. The shear stress variation along the indentation also indicates an acceleration of the flow in this region when the indentation is moving inwards ($\tau<0.5$) and a deceleration when it is retracting ($\tau>0.5$). High wall shear stresses are observed just downstream of the indentation. The vortex forming downstream of the indentation gives high velocity gradients, which results in high wall shear stress.

Figure 6.11 shows the variation of pressure drop (P1-P2 and P1-P3) with the time along the indentation, at the sections, shown in Figure 5.13. For the first quarter of the cycle, the pressure drop increases with the time, while for the second quarter; the pressure drop decreases with time. As the indentation starts receding late in the cycle, the pressure drop increases with time showing a sinusoidal pattern. The pressure drop P1-P3 is greater than the pressure drop P1-P2. The maximum pressure drop across the stenosis occurs when we have the maximum narrowing ($\tau\approx0.5$).

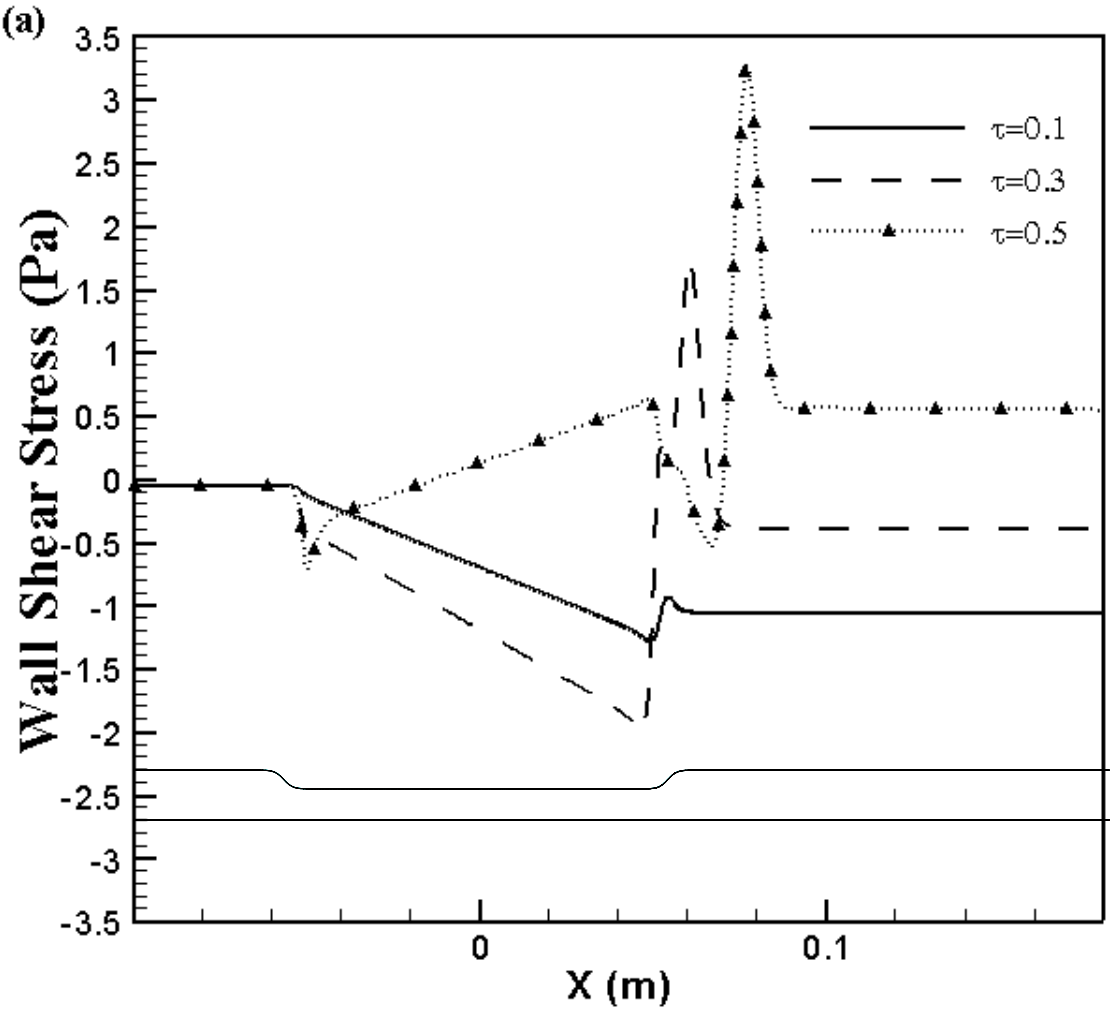

Figure 6.10 (a) Wall shear stress variations during one cycle along the indented wall τ=0.1 to 0.5 for the steady non-Newtonian blood flow characterized by the Carreau-Yasuda model at the inlet -Case III (Re=200, α=13.4).

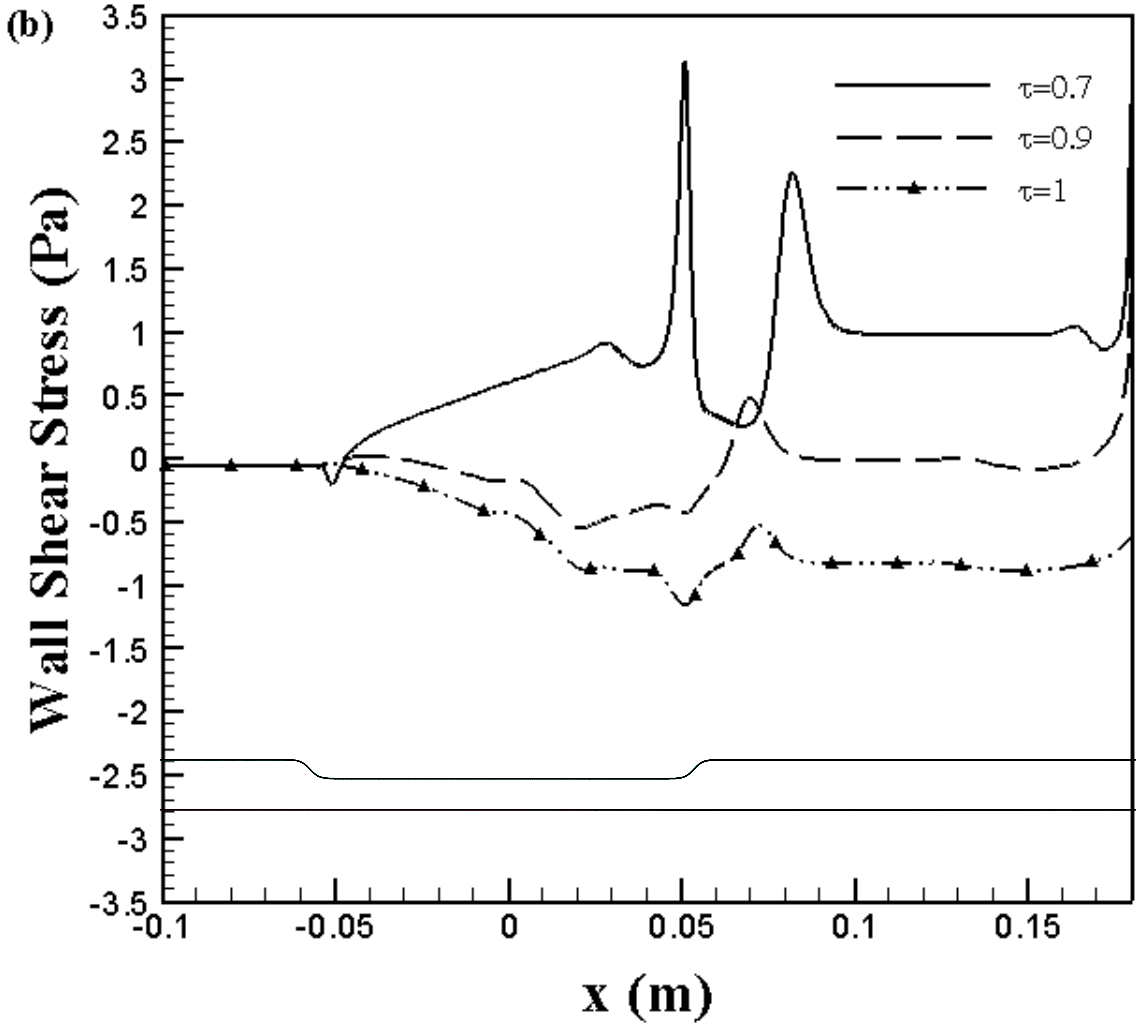

Figure 6.10 (b) Wall shear stress variations during one cycle along the indented wallτ=0.7 to 1 for the steady non-Newtonian blood flow characterized by the Carreau-Yasuda model at the inlet -Case III (Re=200, α=13.4).

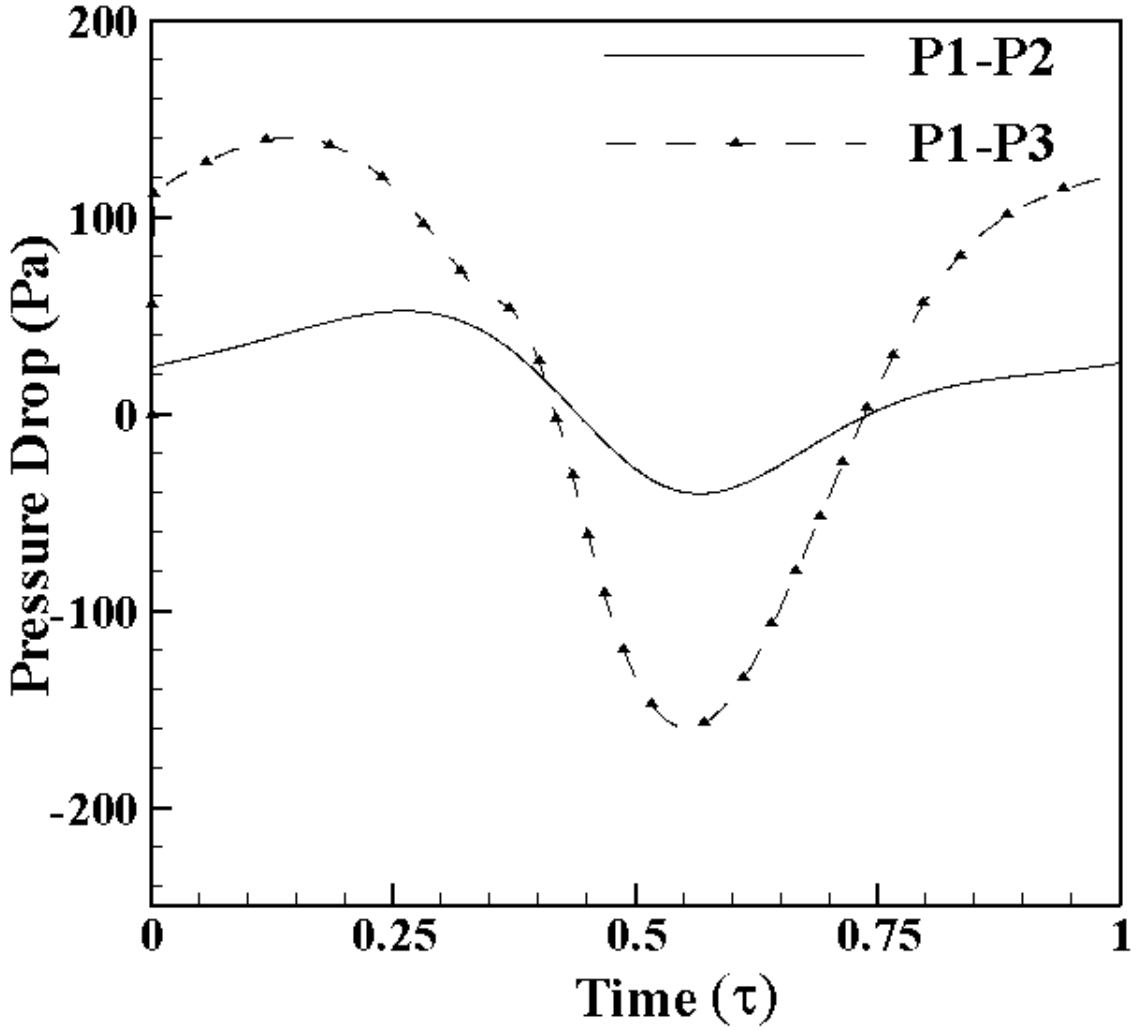

Figure 6.11 Pressure Drop along the indentation for steady non-Newtonian blood flow characterized by the Carreau model at the inlet-Case III (Re=200, α=13.4).

Figure 6.12 shows the variation of axial velocity with the time along the indentation at the sections shown in Figure 5.13. The straight line (at X=-6.5R) in the Figure 6.12, indicates that the flow is not affected upstream of the indentation. At the centre (X=0R) and downstream (X=6.5R) of the indentation, the axial velocity increases sinusoidally with time for the first quarter of the cycle as the indentation is accelerating into the tube. Between the second and the third quarter of the cycle the axial velocity decreases with time. And in the final quarter of the cycle, the axial velocity increases with time. The axial velocity is high downstream (X=6.5R) of the indentation in compare with that of centre of the indentation due to upcoming forward flow.

Figure 6.13 (a), (b), (c) and (d) show the comparison of axial velocity profiles of non-Newtonian power law, Carreau model and Carreau-Yasuda model at different cross sections and various time intervals. From the present figure it can be observed that the three models show similar behavior with a minor difference in the magnitude near the axis. This difference is due to difference in viscosities in the low shear region. Examining the behaviors of the results, one observes that the axial velocity profile assumes a flat shape in the presence of the indentation as well as the downstream of the indentation, instead of a parabolic profile. This observation can be interpreted physically, that if the indentation is moving, then inertial forces associated with the convective accelerations manifest themselves in an amount of the same order as viscous forces, while the former compel the axial velocity profile to attain a flat shape. . No recirculation zone is observed upstream of the moving indentation for all the three models. The axial velocities are observed to be maximum after the indentation (i.e. at 6.5R) for the three models at

different time steps. From the figure, it can also be observed that the reverse flow dominates downstream of the indentation, after $\tau \geq 0.5$. Thus analyzing the behavior of the present figures, one may conclude that the moving indentation affects the axial velocity of the streaming blood significantly and also that the three different models tend to show the similar behavior.

In this chapter, we presented three non-Newtonian models of two-dimensional flows as a step towards the analysis of fully three-dimensional conditions. The three non-Newtonian models showed the same behavior because of the same Reynolds number used. However, a minor difference in the velocity profiles was observed near the axis of the tube, because of the difference in the viscosities used for the three models in the low shear region. Maximum wall shear stress was observed just after the indentation.

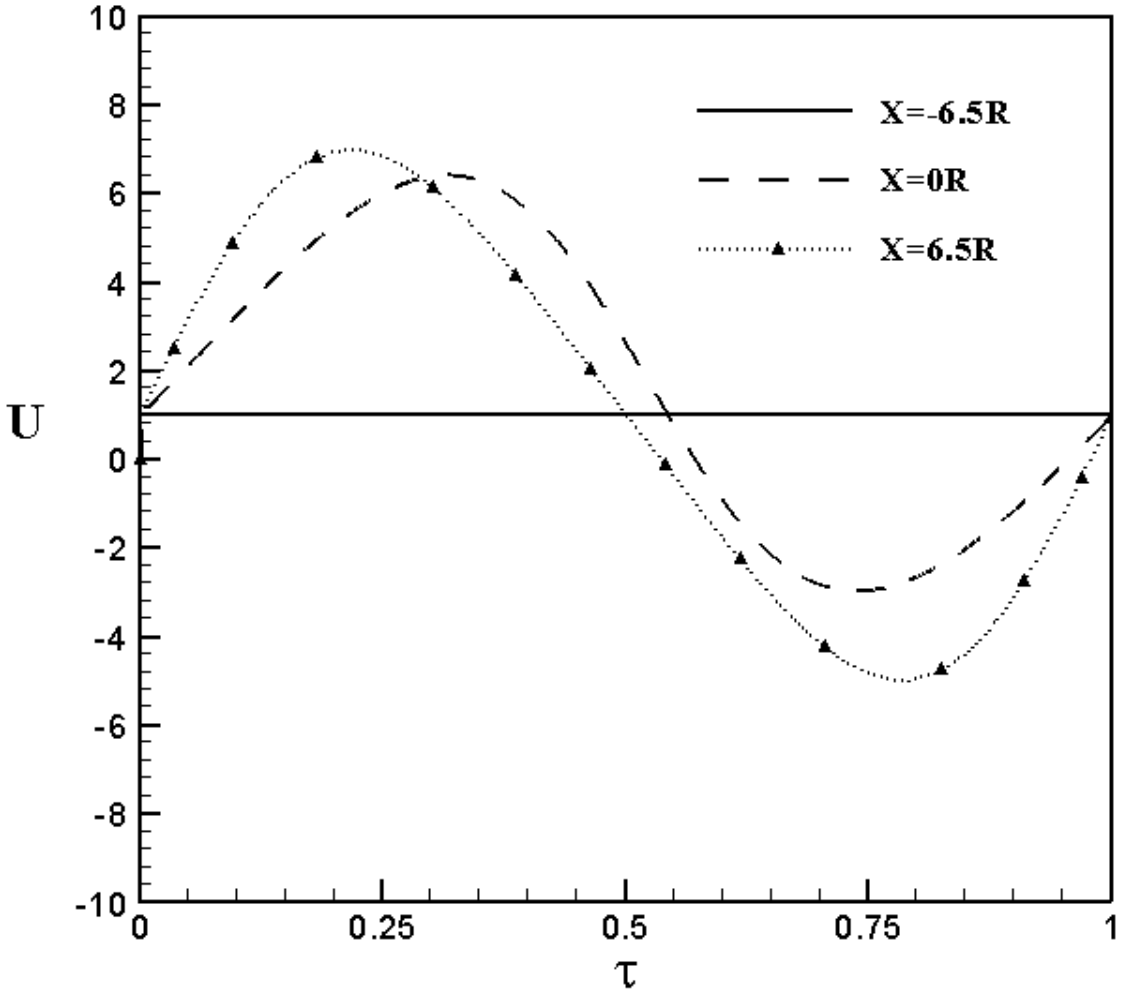

Figure 6.12 Variation of axial velocity with time at different sections of the indentation (Figure 5-13) for steady non-Newtonian blood flow characterized by Carreau-Yasuda Model-Case III (Re=200, α=13.4).

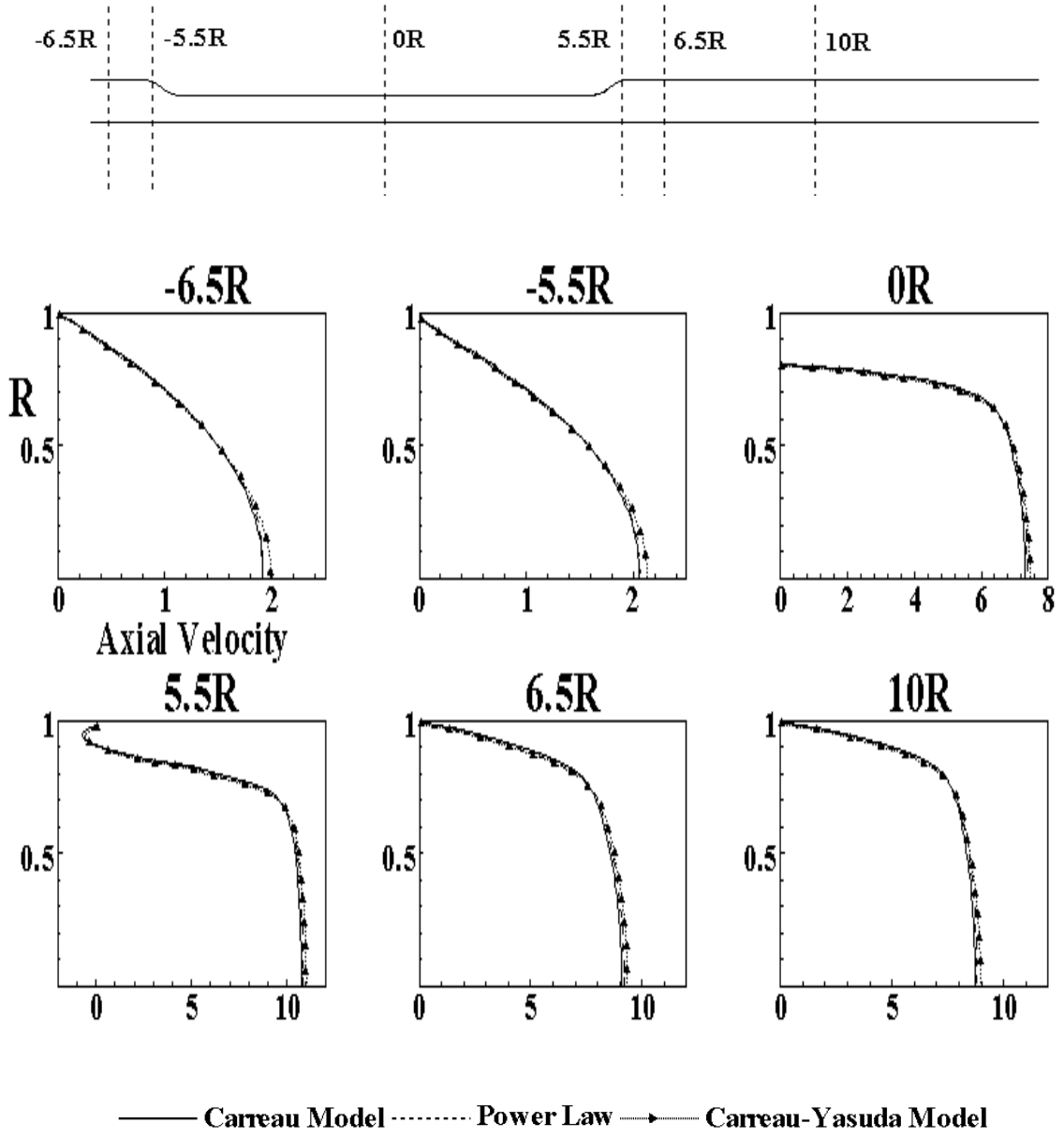

Figure 6.13 (a) Comparison of Axial Velocity profiles obtained by different non-Newtonian models at τ=0.25

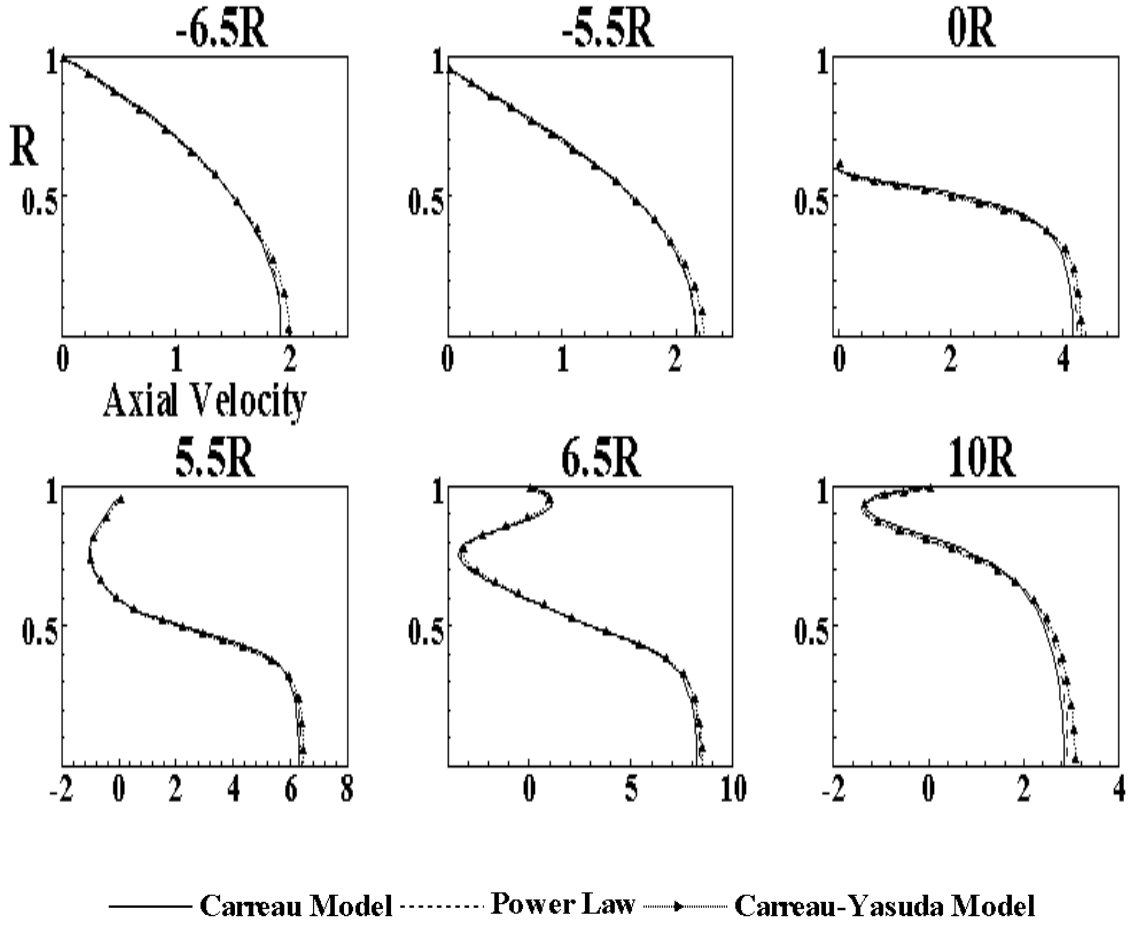

Figure 6.13 (b) Comparison of Axial Velocity profiles obtained by different non-Newtonian models at τ=0.5

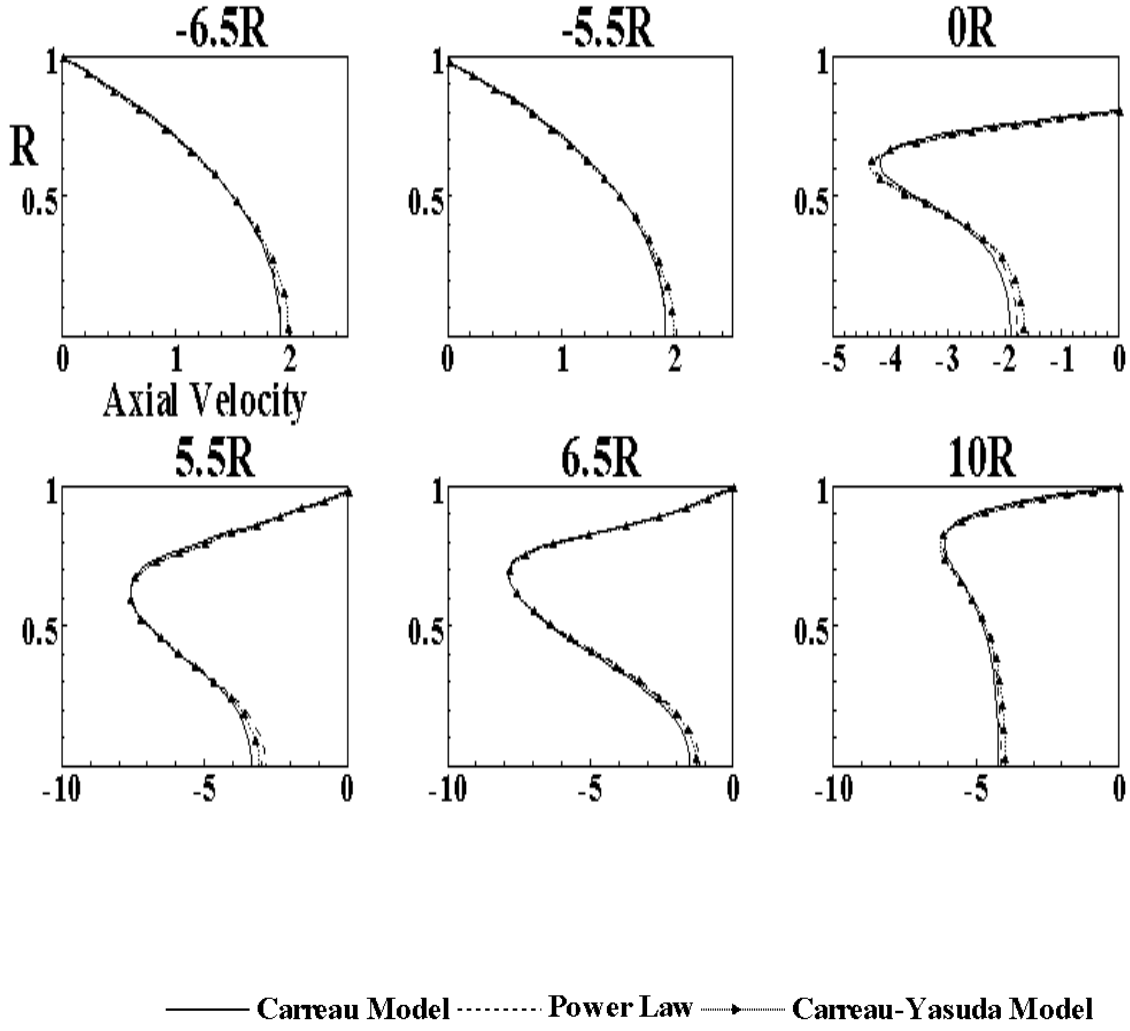

Figure 6.13 (c) Comparison of Axial Velocity profiles obtained by different non-Newtonian models at τ=0.75

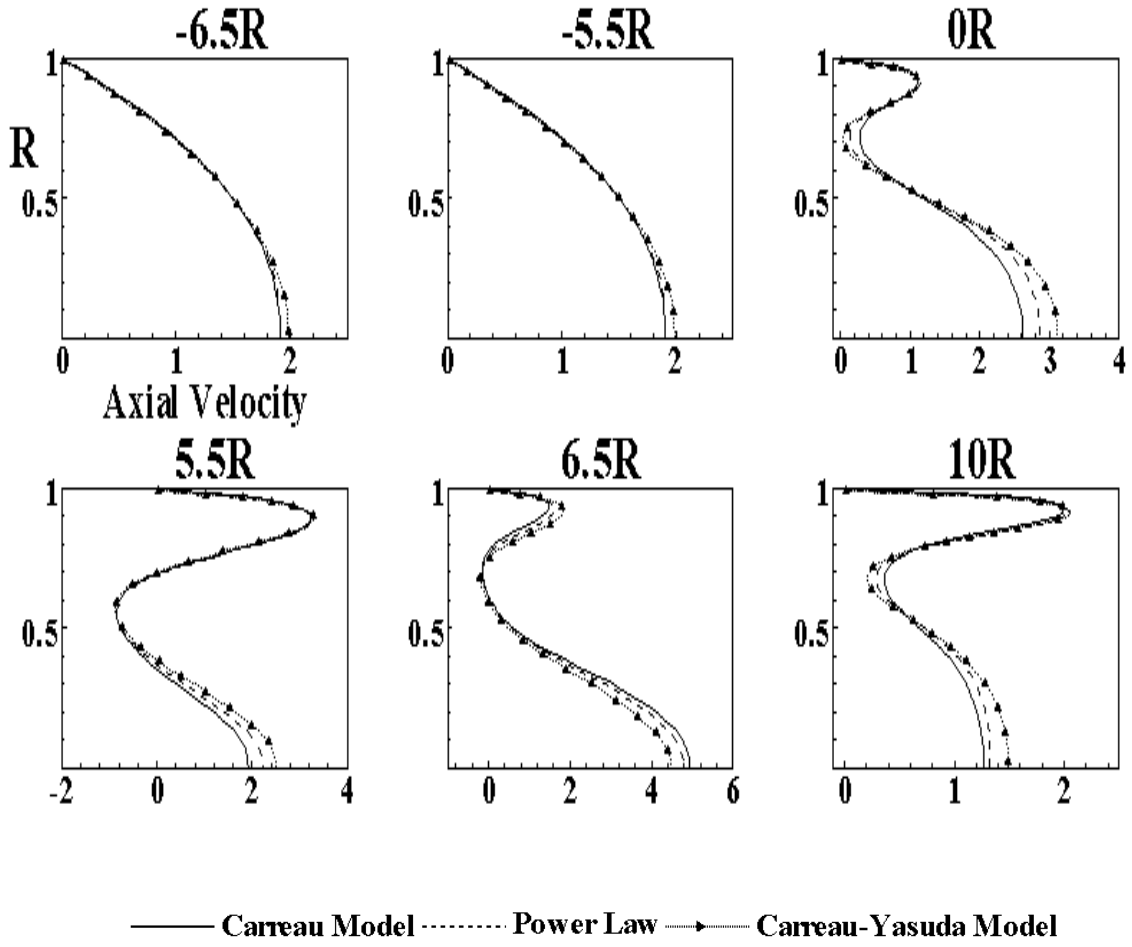

Figure 6.13 (d) Comparison of Axial Velocity profiles obtained by different non-Newtonian models at τ=1

CHAPTER 7

CONCLUSIONS AND RECOMMENDATIONS

7.1. Conclusions

The present research is aimed at modeling of the blood flow in an axisymmetric tube with moving indentation, which closely resembles the flow in arteries and veins. The commercial software FLUENT was used to perform the numerical computations. The model was validated for a two-dimensional channel with moving indentation. The results exhibited excellent agreement with both experimental and numerical work presented in the literature. First the simulations were carried out for the axisymmetric moving indentation taking water as a fluid (as it is widely used for the experimental investigation) for frequencies of 0.1 and 1. The frequency of the 1 Hz closely matches the heart cycle. In addition the simulations were carried again with blood as the working fluid instead of water, considering the blood to be Newtonian. Two cases were analyzed for this simulation one with steady inlet and another with the pulsatile inlet. Later the non-Newtonian properties of the blood were incorporated using three different models,

non-Newtonian Power law model, Carreau Model and Carreau-Yasuda model. The investigation results are presented in the form of streamlines, velocity profiles, and the wall shear stresses.

From the results obtained, the following conclusions can be drawn:

- The time dependent model showed excellent agreement, for the 2D planar channel against Ralph and Pedley's [43] experimental and numerical work.

- For the axisymmetric model with water flow and a wall frequency of $0.1\,Hz$ a single eddy was observed in the lee of the indentation. It grew in size and strength with time and was swept out at the end of the period.

- For the axisymmetric model with water flow and a wall frequency of $1\,Hz$ the flow was very complex. A region of flow reversal prevailed downstream of the indentation. In addition, eddy doubling was observed. It was also observed that the wall shear stress increases with the increase in the frequency of the moving indentation.

- For the steady blood flow inlet, no reverse flow was observed upstream of the indentation. Furthermore, eddy doubling occurred downstream of the indentation for water flow but it was not observed for the blood flow case under same Reynolds number. The wall shear stresses obtained for the blood case were higher than that for water flow.

- For pulsatile blood flow, inlet recirculation zone was observed upstream of the indentation and the reverse flow was found to be dominating downstream of the indentation. The wall shear stresses and the pressure drops obtained for the pulsatile case were same as of the steady case.

- The non-Newtonian properties of blood are characterized by non-Newtonian power law, Carreau and the Carreau-Yasuda models. No recirculation zone was observed upstream of the indentation for all the three models. And the three models showed similar behavior with very little difference in the velocity profiles.

- The Newtonian and the non-Newtonian models exhibit similar behavior in the regions of high shear (i.e. near the wall), but a difference exists in the velocity profiles at the core of the tube because of the low shear rates in these regions.

The main shortcomings of the present study lie in the assumption of axisymmetric, while actual flows in arteries are clearly three-dimensional. This deficiency can be overcome only by the use of a three-dimensional model

7.2. Recommendations

1. Detailed experimental flow data are needed to further validate the flow in a tube with a moving indentation.

2. The scope of this study is limited by the assumption of two-dimensional laminar flow. Further studies are required to extend the results of the present investigation to the three dimensional turbulent flow.

3. Further studies are required to extend the results of the present investigation considering the pulsatile non-newtonian properties at the inlet.

APPENDIX A

Derivation of Equation (3.11 b and c)

V-Velocity:

The analytic functions which approximately fit the shape of the indentation is given by

$$y_w(x,t)=\begin{cases} h(t) & for\ 0<x<x_1 \\ 0.5h(t)\{1-Tanh[a(x-x_2)]\} & for\ x_1<x<x_3 \\ 0 & for\ x>x_3 \end{cases} \tag{A.1}$$

$$h(t)=0.5h_{\max}[1-\cos(\omega t)] \tag{A.2}$$

where $a=4.14, x_1=4b, x_3=6.5b, x_2=0.5(x_1+x_3)$. Here ω is the radial frequency $2\pi/t_0$, t_0 is period of oscillation of the moving indentation, b is the unblocked channel height and is taken as 1cm. The maximum blockage of the channel cross section is $h_{\max}(=0.38b)$ occurs at the middle of the period.

$For\ x_1<x<x_3$ we have,

$$y_w(x,t)=0.5h(t)\{1-Tanh[a(x-x_2)]\}$$

$$\frac{dy_w(x,t)}{dt} = 0.5\{\{1 - Tanh[a(x - x_2)]\}\frac{dh(t)}{dt} \tag{A.3}$$

$$\frac{dy_w(x,t)}{dx} = -0.5h(t) \times aSec^2 h[a(x - x_2)] \tag{A.4}$$

Now, $h(t) = 0.5h_{\max}[1 - \cos(2\pi t / t_0)]$

$$\therefore \frac{dh}{dt} = 0.5h_{\max}(2\pi / t_0)[Sin(2\pi t / t_0)]$$

Here $h_{\max} = 0.38$

$$\therefore \frac{dh}{dt} = 0.5 \times 0.38 \times (2\pi / t_0)[Sin(2\pi t / t_0)]$$

$$i.e\ \frac{dh}{dt} = \frac{1.19381}{t_0} \times [Sin(2\pi t / t_0)] \tag{A.5}$$

Substituting (A.5) in equation (A.3), we get

$$v = \frac{dy_w(x,\ t)}{dt} = 0.5 \times [\{1 - Tanh[a(x - x_2)]\} \times \frac{1.19381}{t_0}[Sin(2\pi t / t_0)]$$

Hence,

$$\boxed{v = \frac{dy_w(x,t)}{dt} = \frac{0.596905}{t_0} \times \{1 - Tanh[a(x - x_2)]\}[Sin(2\pi t / t_0)]} \tag{A.6}$$

Using the non-dimensional variables,

$$U = \frac{u}{U_0},\ V = \frac{v}{U_0},\ P = \frac{p}{\rho U_0{}^2},\ X = \frac{x}{b},\ Y = \frac{y}{b},\ \tau = \frac{t}{t_0} \tag{A.7}$$

Eq. A.6 is written as

$$\boxed{V = \frac{0.596905}{U_0 t_0} \times \{1 - Tanh[ab(X - X_2)]\}[Sin(2\pi\tau)]} \tag{A.8}$$

U-Velocity:

$$u = \frac{\partial x}{\partial t} = \frac{\partial y_w}{\partial t} \times \frac{\partial x}{\partial y_w} = v \times \frac{\partial x}{\partial y_w} = \frac{v}{\left(\frac{\partial y_w}{\partial x}\right)}$$

$$\therefore u = \frac{v}{\left(\frac{\partial y_w}{\partial x}\right)}$$

$$u = \frac{v}{\left(\frac{\partial y_w}{\partial x}\right)} = \frac{v}{-0.5ah(t)Sec^2h[a(x - x_2)]}$$

Substituting Eq.(A.2) in the above equation, we get,

$$u = \frac{-v}{0.095aSec^2h[a(x - x_2)][1 - Cos(2\pi t)}$$

$$u = \frac{-v}{0.095aSec^2h[a(x-x_2)][1-Cos(2\pi t)]} \tag{A.9}$$

Using Eq. (A.7) Eq. (A.9) can be written as,

$$U = \frac{-V}{0.095aSec^2h[ab(X-X_2)][1-Cos(2\pi\tau)]} \tag{A.10}$$

REFERENCES

[1] Graaff, V.D, Kent, M., Fox, S.I., and LaFleur, K.M., 1997 "*Synopsis of Human Anatomy and Physiology,*" Wm. C. Brown Publishers.

[2] Sharp, M.K., Thurston, G.B., and Moore J.E., 1996, "The Effect Of Blood Viscoelasticity On Pulsatile Flow In Stationary And Axially Moving Tubes," Biorheology, Vol. 33, No. 3, pp. 185-208.

[3] Moore, J.E., Nicolas, G., Antonio, D., Doroit, P.A., Dorsaz, P.A., Rutishauser, W., and Meister, J.J., 1994 "Preliminary Analysis Of The Effects Of Blood Vessel Movement On Blood Flow Patterns In The Coronary Arteries," ASME Journal of Biomechanical Engineering, Vol. 116, pp 302-306..

[4] McDonald, D.A., 1974, Blood flow in Arteries, 2nd Ed., Arnold, London.

[5] David N. Ku and Don P. Giddens, 1983, "Pulsatile Flow In A Model Carotid Bifurcation", Arteriosclerosis, Vol. 3, 1, pp 31-39.

[6] David, N.K. and Giddens, D.P., 1983, "Pulsatile Flow In A Model Carotid Bifurcation," Arteriosclerosis, Vol. 3, 1, pp 31-39.

[7] Moore, J.E., and Ku, D.N., 1994, " Pulsatile Velocity Measurements In A Model Of The Human Abdominal Aorta Under Simulated Exercise And Postprandial Conditions," ASME Journal of Biomechanical Engineering, Vol. 116, pp 107-116.

[8] Liou, T.M., Chang, T.W., Chang, W.C., 1994, "Pulsatile Flow Through a Bifurcation With A Cerebrovascular Aneurysm", ASME Journal of Biomechanical Engineering, Vol. 116, pp 112-118.

[9] Maalej, N., Holden, J.E. and Folts J.D., 1998, "Effect Of Shear Stress On Acute Platelet Thrombus Formation In Canine Stenosed Carotid Arteries: An In Vivo Quantitative Study", J. of Thrombosis and Thrombolysis, Vol. 5, pp 231-238.

[10] Bertram. C.D., Tuesta., G. D., and Nugent. A.H., 2001, "Laser-Doppler Measurements Of Velocities Just Downstream Of A Collapsible Tube During Flow-Induced Oscillations", J. of Biomechanical eng., Vol. 123, pp 493-499.

[11] Xue, M.L., and Stanley, E.R., 2001, "Hemodynamic Ractors At The Distal End To Side Anastomosis Of A By Pass Graft With Different Pos:Dos Ratios", J. of Biomechanical eng. Vol. 123, pp 270-276.

[12] Chesler, N.C. and Enyinna, O.C., 2003, "Particel Deposition In Arteries Ex Vivo: Effects Of Pressure, Flow And Waveform", J. of Biomechanical eng., Vol. 125, pp 389-394.

[13] Stephanoff, K.D, Pedley, T.J., Lawrence, C.J., and Secomb T.W., 1983, "Fluid Flow Along A Channel With An Asymmetric Oscillating Constriction", Nature. Vol. 305, pp. 692-695.

[14] Pedley, T.J., and Stephanoff, K.D., 1985, "Flow Along A Channel With A Time-Dependent Indentation In One Wall: The Generation Of Vorticity Waves", J. of Fluid Mech. Vol. 160, pp 337-367.

[15] Womersley, J.R., 1957, "An Elastic Tube Theory Of Pulse Transmission And Oscillatory Flow In Mammalian Arteries" Technical report, Wright Air dev. Ctr. Tech. Rep. WADC-TR-56-614.

[16] Ling, S.C., and Atabek, H.B., 1972, "A Nonlinear Analysis Of Pulsating Flow In Arteries", J. Flud Mech. Vol 55, pp 493-511.

[17] Chang, L.J. and Tarbell, J.M., "Numerical Simulation Of Fully Developed Sinusoidal And Pulsatile (Physiological) Flow In Curved Tubes", J. Fluid Mech. 161, pp 175-198.

[18] Mirsa J, C., and Singh, S.I., 1987, "A Study On The Nonlinear Flow Of Blood Through Arteries", Bull. Math Biol., 49, pp 257-277.

[19] Cen, R.,J.,Liu, and Hwang, H.C., 1987, "Developing Oscillatory Flow In A Circular Pipe: A New Solution", J. of Biomechanical eng. Vol 109, pp 340-345.

[20] Perktold, K., Resch, M., and Florian, H., 1991, "Pulsatile Non-Newtonion Flow Characteristics In A Three Dimensional Human Carotid Bifurcation Model", J. of Biomechanical eng., Vol. 113, pp 464-475.

[21] Xu, S,Y.,. Collins, M.W., and Jones, C., J., H., 1992, "Flow studies in canine Artery Bifurcations Using Numerical Simulation Method., J. Of Biomechanical eng." Vol. 114, pp 504-511.

[22] Tutty, O.R., 1992, "Pulsatile Flow In A Constricted Channel", J. of Biomechanical eng., Vol. 114, pp 50-54.

[23] Ma, X, Lee, G.C., and Wu. S.G., 1992, "Numerical Simulation For The Propagation Of Nonlinear Pulsatile Waves In Arteries", J. of Biomechanical eng. Vol. 114, pp 490-496.

[24] Moore, J.,E., Nicolas, G., Antonio, D,, Doroit, P.,A.., Dorsaz..,P.,A.,Rutishauser, W., and Meister, J. J.,1994 " Preleiminary analysis of the effects of blood vessel movement on bloo flow patterns in the coronary arteries", J. of Biomechanical eng. Vol 116, pp 302-306.

[25] Kobayashi, M.H., and Pereira, J.C.F., 1994, "A computational method for solving Arbitrary two dimensional physiological flows", J. of Biomechanical eng. Vol 116, pp 315-317.

[26] He.,X., and David., N., K., 1994., "Unsteady Entrance Flow Development in a Straight Tube", J. of Biomechanical eng." Vol. 116, pp 355-360.

[27] Sharp, M.K., Thurston, G.B., and Moore J.E., 1996, "The Effect Of Blood Viscoelasticity On Pulsatile Flow In Stationary And Axially Moving Tubes." Biorheology, Vol. 33, No. 3, pp. 185-208.

[28] Ghalichi, F., Deng X., Champlain, A.D., Douville Y., King, M. and Guidoin, R., 1998, "Low Reynolds Number Turbulence Modeling Of Blood Flow In Arterial Stenosis", Biorheology, Vol. 35, pp 281-294.

[29] Moore, J.E, Steinman, D.A., Prakash, S., Johnston, K.W., Ethier., C.R., 1999, "A Numerical Study Of Blood Flow Patterns In Anatomically Realistic And Simplified End To Side Anastomoses", J. of Biomechanical eng. Vol. 121, pp 265-272.

[30] Haidekker, M.A., White, C.R., and Frangos J.A., 2001, "Analysis Of Temporal Shear Stress Gradients During The Onset Phase Of Flow Over A Backward Facing Step", J. of Biomechanical eng. Vol. 123, pp 455-463.

[31] Finol, E.A., and Amon, C.H., 2001, "Blood Flow In Abdominal Aortic Anerysms: Pulsatile Flow Hemodynamics", J. of Biomechanical eng. Vol. 123, pp 474-484.

[32] Lei., M., Giddens., D.P., Jones., S.A., Loth., F.and Bassiouny., H., 2001., "Pulsatile Flow In An End-To-Side Vascular Graft Model: Comparison Of Computations With Experimental Data", J. Of Biomechanical Eng." Vol. 123, pp 80-87.

[33] Ene-lordache, B., Mosconi, L., Remuzzi, G., and Remuzzi, A., 2001, "Computational Fluid Dynamics Of A Vascular Access Case For Hemodialysis", J. of Biomechanical eng. Vol. 123, pp 284-292

[34] Kute, S. M., and Vorp, D.A., 2001,"The Effect Of Proximal Artery Flow On The Hemodynamics At The Distal Anastomosis Of A Vascular Bypass Graft: Computational Study", J. of Biomechanical eng. Vol. 123, pp 277-283.

[35] Prakash, S. and Ross Ethier C, 2001, "Requirements For Mesh Resolution In 3d Computational Hemodynamics", J. of Biomechanical eng. Vol. 123, pp 134-144.

[36] Craciunescu, O.I., and Clegg. S.T., 2001, "Pulsatile Blood Flow Effects On Temperature Distribution And Heat Transfer In Rigid Vessels." J. of Biomechanical eng. Vol. 23, pp 500-505.

[37] Liu, H. and Yamaguchi, T., 2001, "Waveform Dependence Of Pulsatile Flow In A Stenosed Channel", J. of Biomechanical eng. Vol. 123, pp 88-96.

[38] Stangeby, K.D., and Ethier, C. R., 2002, "Computational analysis of coupled blood-wall arterial LDL transport", J. of Biomechanical eng. Vol. 124, pp 1-8.

[39] Stroud., J.S., Berger. S.A., Saloner., D., 2002 "Numerical Analysis Of Flow Through A Severely Stenotic Carotid Artery Bifurcation", J. of Biomechanical eng. Vol. 124 pp 9-20.

[40] Varghese, S. S, and Frankel, S. H., 2003, "Numerical Modeling Of Pulsatile Turbulent Flow in Stenotic Vessels", J. of Biomechanical eng. Vol. 125, pp 445-460.

[41] Kalse, S.G.C., Bijl, H. and Oudheusden B.W.V., 2003, "A One-Dimensional Viscous Inviscid Strong Interaction Model For Flow In Indented Channels With Separation And Reattachment", J. of Biomechanical eng. Vol. 125, pp 335-362.

[42] Augst, A.D., Barratt, D.C., Hughes, A.D., Glor, F.P., Thom, S.A.M and Xu, X.Y., 2003, "Accuracy And Reproducibility Of CFD Predicted Wall Shear Stress Using 3d Ultrasound Images", J. of Biomechanical eng. Vol. 125, pp 218-222.

[43] Ralph, M.E., and Pedley. T.J., 1988, "Flow In A Channel With A Moving Indentation", J. Fluid Mech. Vol. 190. pp 87-112.

[44] Ralph, M.E., and Pedley. T.J., 1989, "Viscous And Inviscid Flows In A Channel With A Moving Indentation", J. Fluid Mech. Vol. 209, pp 543-566.

[45] Demirdzic, I, and Peric, M., 1990, "Finite Volume Method For Prediction Of Fluid Flow In Arbitrarily Shaped Domains With Moving Boundaries", International J. for Numerical Methods In Fluids, Vol.10, pp771-790.

[46] Wang, D.M., and Tarbell., J.M., 1992, "Nonlinear Analysis Of Flow In An Elastic Tube(Artery): Steady Streaming Effects" , J. Fluid. Mech. Vol. 239, pp 341-358.

[47] Johnson, G.A., Borovetz, H.S. and Anderson J.L., 1992, "A Model Of Pulsatile Flow In A Uniform Deformable Vessel", J. Biomechanics, Vol. 25, No. 1, pp 91-100.

[48] Tutty, O.R., and Pedley, T.J., 1994, "Unsteady flow in a non-uniform channel: A model for wave generation, "Physics and Fluids, Vol. 6(1), pp 199-208.

[49] Shim, E.B. and Kamm, R.D., 2002, "Numerical Simulation of Steady Flow in a Compliant Tube or Channel with Tapered wall Thickness", J. Fluid Structures, 16, vol. 8, pp 1009-1027.

[50] Zhao, Y., and Forhad, A., 2003, "A General Method For Simulation Of Fluid Flows With Moving And Compliant Boundaries On Unstructured Grids", Comput. Methods Appl. Mech.Engg, 192, pp. 4439-4466.

[51] Jin, S., Oshinski, J. and Giddens, D.P., 2003, "Effects Of Wall Motion And Compliance On Flow Patterns In The Ascending Aorta", J. of Biomechanical Eng., Vol. 125, pp 347-354.

[52] Thurston, G.B., 1973, "Frequency and shear rate dependence of viscoelasticity of human blood", Biorheology, 16, pp 149-162.

[53] Deutsch, S. and Phillips, W.M., 1979, "The Stability Of Blood Cell Suspensions To Small Disturbances In Circular Couette Flow: Experimental Results For The Taylor Problem", J. of Biomechanical eng., Vol. 101, pp 289-292.

[54] Liepsch, D. and Morvec, S 1984, "Pulsatile flow of non-Newtonian blood flow at the aortic bifurcation", J. of Biomechanics, 26, pp 37-49.

[55] Ku, D.N. and Liepsch D., 1986, "The effect of non-Newtonian viscoelasticity and wall elasticity on flow at a 90 degree bifurcation", Biorheology, 23, pp 359-370.

[56] Theodorou, G. Bellet, D., 1986 "Laminar flows of a non-Newtonian fluid in mild stenosis", Comp. Meth. Appl. Mech. Eng. 54, 111–123.

[57] Nakamura, M, Swada, T., 1988, "Numerical study on the flow of a non-Newtonian fluid through an axisymmetric stenosis", J. Biomech. Eng. Trans ASME, 110, 137–143.

[58] Pak, B., Young Y.I., and Choi, S.U.S., 1990, "Separation and re-attachment of non-Newtonian fluid flows in a sudden expansion pipe", J. Non-Newtonian Fluid. Mech. 37 175–199

[59] Das, B., Johnson, P.C., and Popel, A.S., 1998, "Effect of nonaxisymmetric hematocrit distribution on non-Newtonian blood flow in small tubes", Biorheology 35, pp 69–87.

[60] Gijsen, F.J.H., van de Vosse, and F.N., Janssen, J.D., 1999, "The influence of the non-newtonian properties of blood on the flow in large arteries: steady flow in a carotid bifurcation model", Journal of Biomechanics 32, pp 601–608.

[61] Gijsen, F.J.H., van de Vosse, F.N., and Janssen, J.D., 1999, "The influence of the non-Newtonian properties of blood on the flow in large arteries: unsteady flowin a 90° curved tube", Journal of Biomechanics 32, pp 705–713.

[62] Hussain M.A., Subir Kar and Puniyani, R.R., 1999, "Relationship Between Power Law Coefficients And Major Blood Constituents Affecting The Whole Blood Viscosity", J. of Biosciences, Vol. 24, No.3, pp 329-337.

[63] Buchanan Jr. J.R., Kleinstreuer C., and Comer J.K., 2000, "Rheological effects on pulsatile hemodynamics in a stenosed tube", Computers & Fluids, Vol. 29, pp 695-724.

[64] Shalman, E., Rosenfeld, M., Dgany, E., and Einav. S., 2001, "Numerical modeling of the flow in stenosed coronary artery. The relationship between main hemodynamic parameters", Computers in Biology and Medicine, 32, pp 329-344.

[65] Neofytau, P. and Drikakis, D., 2003, "Non-Newtonian flow instability in a channel with a sudden expansion", J. of Non-Newtonian Fluid Mechanics, 111, pp 127-150.

[66] Chen, J., Lu, X.Y., 2004, "Numerical investigation of the non-Newtonian blood flow in a bifurcation model with a non-planar branch", Journal of Biomechanics, 37, pp 1899-1911.

[67] Mandal P.K., 2005, "An unsteady analysis of non-Newtonian blood flow through tapered arteries with a stenosis", Int. J. of Non-Linear Mechanics, 40, pp 151-164.

[68] Lapidus, L. and Pinder G. F., "Numerical Solution of Partial Differential Equations in Science and Engineering" *John wiley and Sons*, 1982.

[69] Patankar, S.V., 1980. *Numerical Heat Transfer and Fluid Flow,* Series in Computational Methods in Mechanics and Thermal Sciences, McGraw-Hill Book Company.

[70] Versteeg, H.K., and Malalasekera, W. *An Introduction to Computational Fluid Dynamics, The Finite Volume Method,* Longman Scientific and Technical, 1995.

[71] Barth, T. J. and Jespersen, D., "The design and application of upwind schemes on unstructured meshes".Technical Report AIAA-89-0366, AIAA 27th Aerospace Sciences Meeting, Reno, Nevada, 1989.

[72] Patankar, S. V. and Spalding, D. B., "A Calculation Procedure for Heat, Mass and Momentum Transfer in Three-dimensional Parabolic Flows", *International Journal of Heat and Mass Transfer*, Vol. 15, pp. 1777-1787, 1972.

[73] Fluent 6.1 Manual, February 2003.

VITA

NAME: Shaik Abdul Qaiyum

ADDRESS: 40-D, G.P.R.A. Campus, Gachibowli,
Hyderabad-500 032
Andhra Pradesh, INDIA.

E-MAIL: abdulq77@rediffmail.com

EDUCATIONAL QUALIFICATIONS

Master of Science in Mechanical Engineering (Thermal Fluid Sciences)

Sept. 2002 – April. 2005

King Fahd University of Petroleum and Minerals, Dhahran, Saudi Arabia

GPA – 3.72/4.0

Bachelor of Engineering (Mechanical)

Aug. 1997 – Feb. 2001

Osmania University, Hyderabad, India

First Class with Distinction